Dissociative chemisorption of methane on Ni(111)
Krishna Mohan, G.P.

Dissociative Chemisorption of Methane on Ni(111)

Krishna Mohan G. Prasanna

Dissociative Chemisorption of Methane on Ni(111)

PROEFSCHRIFT

ter verkrijging van

de graad van Doctor aan de Universiteit Leiden,

op gezag van de Rector Magnificus Prof. Mr. P. F. van der Heijden,

volgens besluit van het College voor Promoties

te verdedigen op woensdag 13 oktober 2010

klokke 15.00 uur

door

Krishna Mohan Gangadharan Prasanna

geboren te Trivandrum, India in 1980

Promotiecommissie

Promotores: Prof. dr. G. J. Kroes

                           Prof. dr. R. A. Olsen

Overige leden: Prof. dr. J. Brouwer

                           Prof. dr. M. C. van Hemert

                           Prof. dr. M. T. M. Koper

                           Dr. A. P. J. Jansen

                           Dr. L. B. F. Juurlink

                           Dr. A. Valdes

In memoriam

Prem,
My tutor at school (93-94).

the core energy to complete this work is just rooted to his motivations,

which I received from him on my school/college days...

Contents

Chapter 1

Introduction

1.1   Introduction

In most chemical reactions aimed at making specific chemicals, one needs to activate the stable reactants (like methane) to convert them into desired products using catalysts. Among the various types of catalysis, the heterogeneous version is attracting wide attention because of its immense industrial importance for the production of many commodity chemicals, e.g. hydrogen, ammonia, sulfuric acid [1]. In heterogeneous catalysis the catalyzed reaction occurs at the boundary between two phases. In this class of catalysis reacting molecules are adsorbed from a gas or liquid phase onto the surface of a solid catalyst (usually a metal). Thus, gas-surface interactions and reactions on metals play a crucial role in the science of heterogeneous catalysis reactions. A wide range of interesting gas-surface reaction systems can be observed, from the inside of a chemical reactor to the outside surface of a space ship. Many industrial processes benefit hugely from catalysis; these processes include the Haber-Bosch process for the production of ammonia, the hydrogenation of edible oils, and various processes within the petrochemical industry such as cracking of crude oil, to name a but a few. Indeed, the catalytic converters in automobiles are nothing but a small gas-surface reaction system which converts harmful exhausts into the less poisonous byproducts, thereby minimizing the environmental hazards.

Catalysis research has a long history. The alchemical era was dominated by the search for the 'philosophers stone' - a mystical catalyst - that could convert cheap metals into precious noble metals. The first successful use of a synthetic catalyst was reported by Valerius Cordus, who used sulfuric acid to catalyze the conversion of alcohol to ether [2]. Apparently, the first report of a gas-surface catalyst was authored by Prof. J. W. Doebereiner, who wrote *". . . that finely divided platinum powder causes hydrogen gas to reaction with oxygen gas by mere contact to water whereby the platinum itself is not altered"* [3].

As for many other scientific fields, this area has been gradually strengthened by the development of various experimental techniques. Today, both scanning tunneling microscopy and modern spectroscopic measurements are regularly employed to observe details at the microscopic level of the system [4]. For example, the atomic positions of both the adsorbate and substrate are determined by scanning tunneling microscopes. Many spectroscopic methods, such as sum frequency gen-

eration and stimulated Raman pumping are used in conjunction with molecular beam experiments to study the details of 'state-specific' chemistry [5].

The investigation of details of reaction mechanisms in gas-surface systems is therefore now possible. Nevertheless, a full understanding of the reaction dynamics requires accurate theoretical calculations and modeling, and the comparison of theoretical results with experimental data. For instance, for a thorough understanding of a surface reaction, a dynamical simulation has to be performed to understand the femto-/pico-second atomistic level details of the reaction mechanism. With the use of state-of-the-art modeling codes and computers, it is now possible to accurately simulate several spectroscopic and molecular beam experiments of gas-surface systems [4]. Density functional theory (DFT) [6, 7] deserves a special mention here since without it many of the gas-surface theoretical calculations could not be performed, due to the large number of electronic and/or spatial degrees of freedom of the system that needed to be treated, and the demands this puts on the computational resources.

In this thesis we attempt to understand several aspects of the gas-surface physics/chemistry of (a) the dissociative chemisorption of CH_4 on the Ni(111) surface and (b) N_2 dissociation over the Ru(0001) surface. Apart from their industrial importance, these systems are regarded as prototypes for molecular beam and state-specific spectroscopic experiments. We performed both static DFT and dynamical calculations to understand better: (i) the role of the vibrational normal mode specificity and the collision energy dependence of the CH_4 reactivity, (ii) the possible reaction paths and dissociation dynamics of CH_4 and N_2, (iii) the role of different vibrational and rotational quantum states, (iv) the applicability of the Born-Oppenheimer approximation for N_2 dissociation and (v) the applicability of different DFT functionals for these systems.

1.2   Ruthenium and Nickel as industrial catalysts

From various experimental and theoretical studies, the role of Ruthenium catalysts in ammonia production is now reasonably well understood. By using a Ru catalyst, the reaction barrier of N_2 dissociation can be reduced to 1.4 eV from its gas phase dissociation value of 9.8 eV [8]. Since around 2% of the world's annual energy supply is used for making ammonia [9] it is natural to investigate this system in detail, in which the reaction

$$N_2(gas) \rightarrow 2N(adsorbed)$$
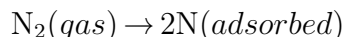
is the rate limiting step. Further studies of this reaction over the ruthenium surface are still necessary to understand how to avoid catalytic poisoning by steam [1] and to reduce the energy cost [10].

The need for sustainable energy has never been greater [11]. The quest for a green fuel – e.g. hydrogen - has been and remaining a serious global challenge. Although hydrogen could in principle be a 100% green fuel, more than 50% of its production still uses catalytic steam reforming, where methane is the major feedstock and nickel is the catalyst [12]. Unfortunately, this process leads to CO2 emission. In this endothermic process the rate limiting step is

$$CH_4(gas) \rightarrow CH_3(adsorbed) + H(adsorbed).$$

To enhance the rate of this reaction, vibrational excitation of CH_4 is found to be effective by many spectroscopic studies [13, 14, 15, 16, 17, 18] and chemical engineering works [19]. We also note that it has been observed that carbon deposition causes severe problems in the steam reforming process. Interestingly, Ni catalysts used in steam reforming are more resistant to deactivation by carbon deposition if the nickel surface contains a small amount of sulfur or gold [20].

1.3 Energetics and Dynamics at surfaces

1.3.1 Interactions at surfaces

The adsorption of a molecule on a surface - both chemisorption and physisorption - is a central concept in the field of surface science and heterogeneous catalysis. In chemisorption, the molecules stick to a surface by a strong chemical interaction, whereas in physisorption it is by weak interactions such as van der Waals forces (see Fig. 1.1(a)). In other words, physisorption does not involve electron transfer between the molecule and the substrate and hence it is highly non-directional, unlike chemisorption [4]. A typical energy range of chemisorption energies is 0.5 eV or more, while for physisorption it is less than 0.3 eV [21].
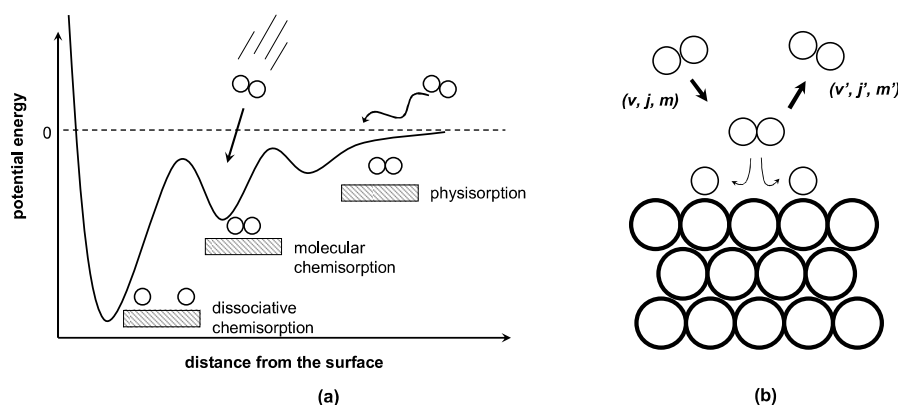
Figure 1.1: (a) Graphical representation of some gas-surface adsorption interactions, and (b) dissociative chemisorption and scattering events of a diatomic molecule.

The ability of a metal to act as a catalyst strongly depends upon the electronic structure of its surface atoms, with which the incoming gas molecule interacts. Since chemisorption creates new chemical bonds, the electronic structure of the adsorbate and substrate (generally metals) is strongly perturbed by their mutual interaction - the interaction leads to a significant hybridization of the electronic

orbitals [22]. To explain how a catalyst works and what the trends are when going from one catalyst-surface/structure to another, one can use molecular orbital (MO) and band structure theory. MO theory provides a fair amount of detailed intuition about the energetics of chemical reactions based on the symmetry properties of MOs and atomic orbitals (AOs). On several transition metals the weakening of the molecular bond occurs through charge transfer from the metal to the empty or antibonding orbitals of the adsorbate molecule. For example, (transition) metals are able to catalyze many thermally assisted reactions (eg. production of cyclo-alkanes). In this case it is necessary to populate the antibonding π (or π^*) orbitals of alkenes to convert them into cyclo-alkanes. This can be done by using a transition metal as a catalyst. In the presence of a transition metal, the electrons from π-orbital of alkenes will pass to the AOs of the metal of the corresponding symmetry (the t_{2g} d-orbitals). This make the reaction thermally permitted.
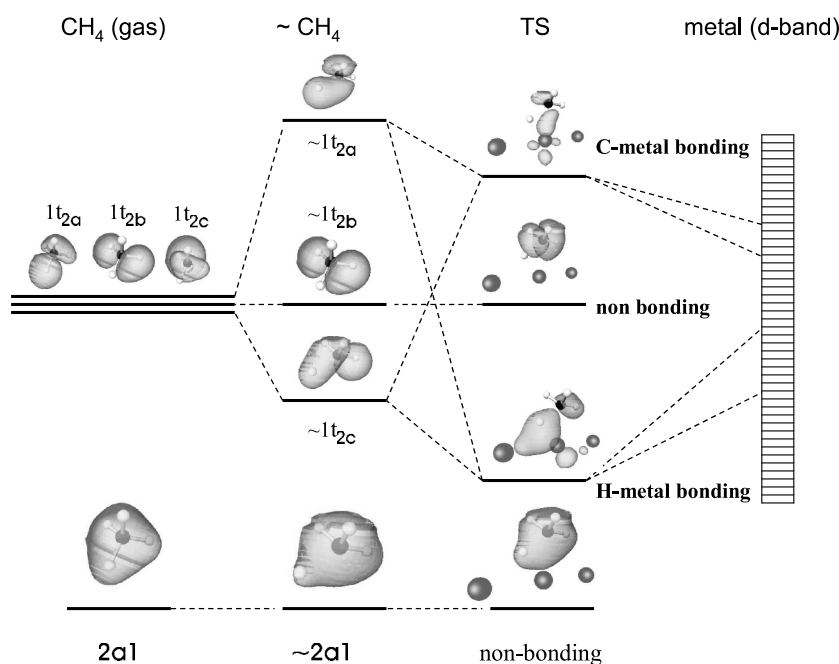
Figure 1.2: One electron Kohn-Sham real eigenstates of methane interacting with a *d*-band metal. Tildes indicate the distorted molecular orbitals and geometries. Reprinted with permission from A. T. Anghel et al., Phys. Rev. B, 71, 113410. © 2005 the American Physical Society.

In the context of extended MO systems, the local density of states at the Fermi level has been successfully correlated with the reactivity of metal surfaces [23]. To analyze and describe the nature of the chemical bonds, the local density of states or projected density of states are often used. Many models (e.g. Newns-Anderson)

have been proposed to provide semi-quantitative results for chemisorption properties [24]. Nowadays many of these approximate methods are predominantly used for explanatory purposes, due to the ease of performing numerical self-consistent calculations based on the density functional theory (DFT) (See Chapter 2). Figure 1.2 depicts a DFT based MO description of the chemical interaction between methane and a transition-metal, in which the Kohn-Sham orbitals of CH_4 interact with delocalized metal orbitals, resulting in C-metal and H-metal bonds.

The adsorbate-surface interaction can be described my many models (using minimal DFT data), such as the *d*-band model developed by Hammer and Nørskov [25]. The model suggests that the degree of orbital overlap with the adsorbate (or the hybridization energy between the bonding and anti-bonding adsorbate states) and the degree of filling of the antibonding states on adsorption determine the reactivity of the transition metals [25].

1.3.2 Dynamic events at surfaces

To understand the detailed reaction mechanisms behind the various dynamics events, one needs to perform dynamics simulations. In this work we only consider 'adiabatic' dynamics, in which bond making as well as bond breaking events are described by motion of nuclei on a ground state potential energy surface (PES). Using adiabatic PESs, several surface chemical reactions can be described which occur on a pico-second timescale (e.g. dissociative chemisorption, associative desorption, etc.).

In experimental surface chemistry, much chemical dynamics is studied using molecular beam experiments. Some of the important gas-surface scattering events in the molecular beam experiments are elastic, inelastic and reactive scattering. In elastic scattering there will be no transfer of energy among different degrees of freedom in the reactant molecule and the surface. In the inelastic scattering process, the transfer of energy among degrees of freedom in the system is allowed, but no chemical reaction occurs. A special process that may occur in molecular-surface scattering is diffraction, which is due to the periodic nature of the surface.

Many molecular scattering events are accompanied by rotational or vibrational (de-) excitations (see Fig. 1.1(b)). For instance, in a scattering event the vibrational state of a molecule may change and the molecule may be vibrationally excited or de-excited. A vibrational excitation can only occur if there is sufficient energy available in the collision, since the total energy must always be conserved. The energy released from the vibrational de-excitation can flow to other degrees of freedoms, like rotation and translation. A rotational (de-) excitation can occur only when the molecule-surface potential is anisotropic. Energy that is released from a rotational de-excitation can also flow to other degrees of freedom, like translation and vibration.

Other important dynamics events that may occur on a surface are diffusion and desorption. Energy transfer from the surface lattice to the translational coordinates of the adsorbents may cause diffusion and desorption. These processes
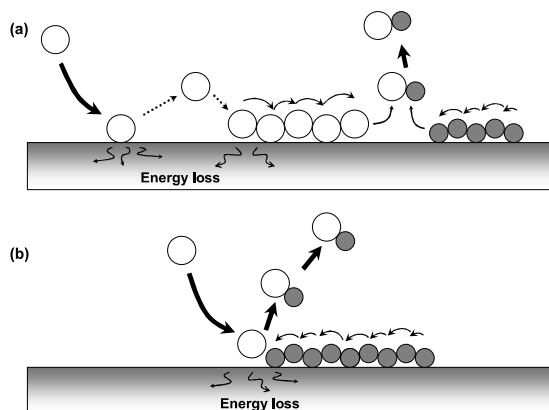
Figure 1.3: Schematic illustrations of (a) the Langmuir–Hinshelwood and (b) Eley–Rideal mechanisms in gas–surface dynamics.

involve bond breaking with the surface and have larger energy barriers than physisorption. Generally, diffusion energy barriers are found to be smaller ($\approx$0.3 eV) on terraces, whereas barriers for diffusion across steps are much higher ($\approx$1 eV) [26]. Desorption and adsorption are related to each other by time-reversal symmetry. The principle of detailed balance [27, 28] relates adsorption to desorption (at a particular coverage and temperature). It has been reported that thermally or photochemically produced electron-hole pairs can induce associative desorption [29] . DFT studies indicate a possible role of subsurface atoms in the desorption process, along with the importance of lattice relaxation [30].

To explain important reaction events at surfaces macroscopic reaction models are widely used. For example, a reaction would be considered to be of the 'Langmuir–Hinshelwood' type if both reactants first adsorbed onto the surface, and then reacted to form the products after equilibration with the surface. If one reactant first adsorbs, and the other then reacts with it directly from the gas phase, the reaction is of the 'Eley–Rideal' type. See Fig. 1.3 for a schematic illustration of these mechanisms. In the case of steam reforming reaction, the experimental data have a good fit with the 'Langmuir–Hinshelwood' model [31]. In general, the Eley–Rideal mechanism is more exothermic than the Langmuir–Hinshelwood mechanism [32]. In these two reaction-mechanisms at least one of the reactants, whether it is a molecule or a single atom, is already adsorbed on the metal. The process of adsorption of molecules or atoms on metals, which must precede these reactions, is one of the major steps in any gas-metal reactions.

To provide a detailed understanding of the origin of mode-specific disposal of energy and to understand the relative importance of kinetic energy versus internal energy (rotational or vibrational), a detailed understanding of the location of the transition state and motion of the nuclei over the PES is required. For instance, H_2 dissociation on nickel surfaces shows no vibrational enhancement [33]. On copper surfaces, however, vibrational enhancement of dissociation of H_2 has
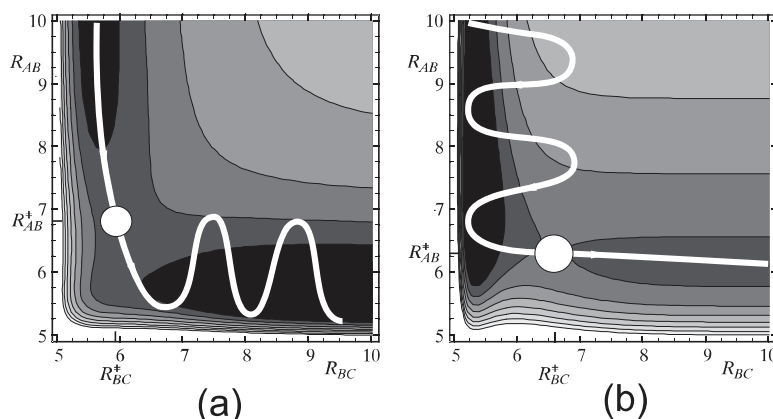
Figure 1.4: An illustration of the Polanyi's rule for an early barrier (a) and a late barrier system (b), for a collinear reaction, A + BC → AB + C, as a function of reaction coordinates, R_{AB} and R_{BC}. The transition state is indicated by the white dots with the trajectories (the white curves). Figure reprinted with written permission from L. Piela, Ideas of Quantum Chemistry, Elsevier, Amsterdam (2007). © L. Piela.

been demonstrated using molecular beam experiments [34]. This mode of energy utilization can be qualitatively predicted by Polanyi's rule. The rule suggests that reactions which possess '*early*' barriers will be promoted preferentially by initial translational excitation, while reactions with '*late*' barriers will be promoted preferentially by reactant vibrational excitation [35]. A schematic illustration of Polanyi's rule is shown in Fig. 1.4.

1.4 Major experimental results

In this section a summary of the major experimental results principal to the main work of this thesis is presented. The 'state-resolved' reactivity measurements of methane demand special attention because they provide many insights on vibrational mode-specific and bond-selective chemistry. In these experiments selective excitation of particular vibrational and rotational quantum states as well as local modes of CH_4 are possible. Although most of these experiments on CH_4 involve nickel surfaces, a variety of similar experimental results have been obtained for many other metal surfaces. For example, the molecular beam experiments of CH_4 dissociation on W(110) [36], Pt(111) [37] and Ru(0001) [38] surfaces all provide similar results to those on nickel surfaces, and show both translational and vibrational activation of the reaction.

The first state-resolved experiment on CH_4 + Ni was reported by Juurlink et al., using an infrared (IR) laser. They observed that on Ni(100) laser-excited CH_4 (excited to $v = 1$ of the ν_3 C-H stretching vibration) dissociates with up to 1600 times the probability of molecules that do not absorb IR light, i.e., CH_4 in its ground vibrational state [15]. A preference for vibrational over translational energy activation in this reaction was observed by Smith et al. [39] for the Ni(100) surface. They reported that CH_4 in its vibrational ground state requires 0.466 eV of translational energy to attain the same reactivity enhancement provided by

0.373 eV of ν_3 vibrational energy. Another study by Juurlink et al. [14] reported the efficiency of the ν_3 C-H stretch at promoting dissociative chemisorption on Ni(111) and Ni(100) surfaces with respect to the $3\nu_4$ bend vibrational state (see Fig. 1.5(a)). Even though $3\nu_4$ contains 30% more energy than the $1\nu_3$ state the results showed the $3\nu_4$ state to be at least 4 times less reactive than $1\nu_3$.

A recent work of Killelea et al. [16], which used CHD_3 molecules in a molecular beam with one quantum of C-H stretching vibration (ν_1), reconfirmed that the excitation of the C-H stretch in CHD_3 favors the dissociation. This work also suggests that the symmetric and antisymmetric stretches in methane or its isotopologues lead to very different reactivities. Indeed, molecules with the symmetric stretching vibration excited with one quant can be as much as 10 times more reactive than ones with the antisymmetric stretch excited with one quant at similar collision energies. [17]

Laser experiments based on stimulated Raman pumping of CD_2H_2 excited to the |20> and |11> vibrational states, and incident on a Ni(100) surface, showed a higher reactivity (around 5 times) of the |20> state [18] (see Fig. 1.5(b) for a comparison). A stimulated Raman pumping experiment by Maroni et al. [17] showed that the reactivity of symmetric-stretch ($1\nu_1$) excited methane is about an order of magnitude higher than that of methane excited to ν_3 state. They also reported that the $1\nu_1$ and the $2\nu_3$ states have a similar reactivity.

All the discussed vibrational state-specific experiments indicate a failure of the statistical model [40, 41] used to calculate the reaction rate for the dissociative chemisorption. The statistical model treats the vibrational and translational energy on an equal footing, arguing that the reactivity is solely determined by the total energy of the molecule. This model therefore excludes the possibility of 'mode-specificity' in the reaction. Instead, the experiments demand full dimensional dynamical calculations to capture the necessary physics of the reactive CH_4[5].

For the N_2+Ru(0001) system, the molecular beam experiments [42, 43, 44] showed a slow increase of the sticking coefficient (S_0) with incident kinetic energy (E_i), where $S_0 < 0.01$ at E_i up to 4.0 eV (see Fig. 1.6). From these experiments it can be noted that (1) S_0 is almost independent of the surface temperature, which suggest that phonons play a minor role in this system, (2) an increase of the nozzle temperature from 700 K to 1800 K increases S_0 by an order of magnitude, which gives evidence for vibrational as well as translational activation, and (3) a higher vibrational efficacy (≈ 1.6) indicates that the vibrational excitation may promote reaction more efficiently than increasing E_i,- a consequence of the late barrier.

1.5   Theoretical approximations

In this section, we consider the two major approximations employed in the work. Since all the calculations were done using a static metal surface (Ni or Ru), the
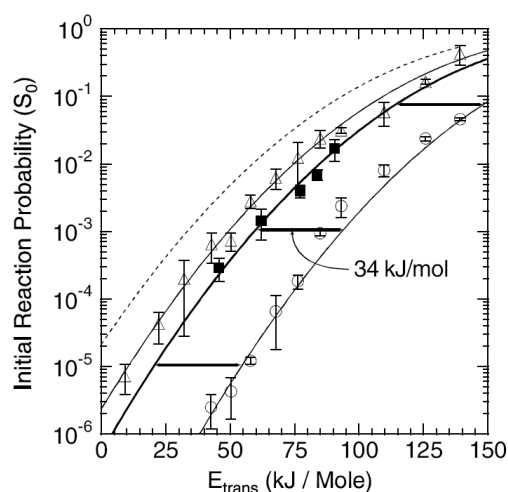
(a) State-resolved initial reaction probability for CH_4 molecules incident on Ni(111) surface in ground state (circles), ν_3 (triangles), and $3\nu_4$ (squares). Etrans denotes incident kinetic energy normal to the surface. Reprinted with permission from L. B. F. Juurlink et al., Phys. Rev. Lett., 94, 208303. © 2005, the American Physical Society.
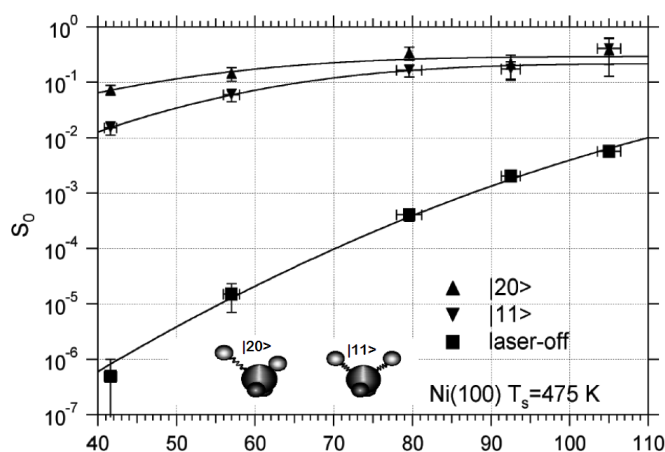
(b) The state resolved sticking coefficients for CH_2D_2 in the |20> |11> and ground vibrational states on Ni(100) surface as a function of incident kinetic energy normal to the surface. S_0 denotes initial reaction probability. Reprinted with permission from R. D. Beck and T. R. Rizzo, Chimia, 58, 306. © 2004, Swiss Chemical Society.

Figure 1.5: Results of two important state-resolved reaction probability measurements of CH_4 dissociation on nickel surface.
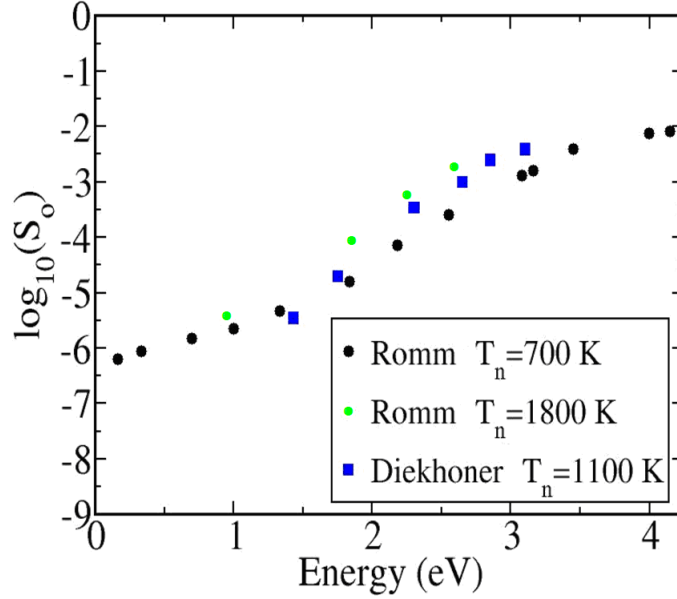
Figure 1.6: The experimental dissociation probability for N_2 on Ru(0001) plotted logarithmically vs. the incident normal energy for three different nozzle temperatures.

possibility of interaction between the molecule and the surface lattice vibrations is excluded. In other words, phonon interactions were neglected. In addition to this, we also neglected the possibility of electron-hole pair excitations in all our calculations.

The coupling of phonons to the motion of adsorbing species can often be neglected in the case of adsorbates with lower mass. For example, theoretical work by Dohle and Saalfrank [45] showed that the effects of including phonons in the calculation of reaction probabilities at 0 K is negligible in some diatomic molecule-surface systems such as dissociation of hydrogen isotopomers on copper. In their surface oscillator model calculations including phonon motions, they found a shift of the reaction probability curve of H_2 with 0.02 eV - which is within the error bars of the current supercell approaches of the DFT [46]. A recent experiment by Killelea et al. [47] on CH_4/Ni(111) revealed the surface temperature dependence of methane activation on Ni(111). In their vibrational state resolved measurements they observed an increase of the reactivity of CH_4 by up to 8 times, when the surface temperature was increased from 90 to 475 K. These results support the DFT calculations [48, 49] that predict an important role for lattice deformation in transition state access for CH_4/metal systems. The neglect of phonon interactions in this system is therefore not justified if quantitative accuracy is desired.

In the context of the N_2/Ru(0001) system, the exclusion of phonons can be considered as a reasonable approximation. Although N_2 is a heavy molecule and some energy exchange with phonons could be expected, experiments on Ru(0001) show the dissociation probability of nitrogen to be almost independent of surface temperature [42, 50].

Another major approximation in this work is the neglect of electron-hole (e-h) pair excitation. E-h pair excitation plays a crucial role in many systems such as

photocatalysed dissociation of water [4]. Experiments show direct evidence for nonadiabatic effects in molecule-surface scattering in which e-h pair excitations accompany chemisorption of molecules [51]. The electron emission from low work function metal surfaces (e.g. Cs/Au(111)) accompanying scattering of highly vibrationally excited molecules (e.g. NO) with high electron affinity also points to considerable nonadiabatic coupling of nuclear motion to electronic excitations at metal surfaces [52]. In all of our dynamical simulations we assumed that the electrons stay in their electronic ground state. This intrinsically avoids the treatment of the electronic excitations in our study. In general, neglecting electron-hole pair excitations is a reasonable approximation in the case of adsorption on semiconductors and insulators [21], but its significance in gas-metal reactions is under ongoing debate [53]. This approximation is considered to be reasonable in the CH_4/Ni system [54, 55, 56], because of (1) the low electron affinity of the CH_4 precursor and (2) the absence of the chemisorption wells in front of the barrier to reaction[57].

In the N_2/Ru systems, the influence of nonadiabatic effects on molecule-surface reactions has become a hot topic. The experimental results for this system suggest the possibility of e-h pair excitations in the Ru surface [43, 44]. For example, (1) the system exhibits a very low reaction probability (10^{-2}) [42, 43] even when the incident energy of N_2 reaches a value of 4 eV - which is almost twice as high as the reaction barrier, (2) only a small degree of vibrational excitation is seen in molecular beam experiments on N_2 scattering from Ru(0001) [58]. The latter result is unexpected for a late barrier system, and to interpret these results it is assumed that incident energy dissipation to e-h pair excitations occurs. Furthermore, laser assisted associative desorption (LAAD) experiments [43] suggested that 2/3 of the energy used by N_2 to overcome the barrier was lost to the surface, which was also attributed to e-h pair excitation.

1.6 Outline and major results of this thesis

This thesis deals with two different dissociative chemisorption reaction systems viz., (1) CH_4/Ni(111) and (2) N_2/Ru(0001). In this section, we summarize the main results obtained and discussed in this thesis. The theoretical methods used to perform the calculations, such as DFT, potential energy surface (PES) fitting, and classical and quantum dynamics, are discussed in **Chapter 2**.

In **Chapter 3**, we investigated the vibrational mode specificity for dissociative chemisorption of CH_4 on Ni(111). It should be noted that in our calculations in some cases we made a comparison between theoretical data for the Ni(111) surface and experimental data for the Ni(100) surface regarding the effect of vibrational pre-excitation. Although the Ni(100) surface is more reactive than the Ni(111) surface, for qualitative purpose this comparison can be justified. For example, the $3\nu_4$ state is less reactive than $1\nu_3$ on both Ni(100) and Ni(111) [14].

This work is the first full-dimensional (with respect to the degrees of freedom of the molecule) study for analyzing the various normal modes along a minimum energy path for a dissociative chemisorption reaction of a polyatomic molecule. In the plane-wave DFT calculations we used the PW91 functional [59], and we made sure that the point-group symmetry of the dissociating molecule-surface system is

preserved throughout the reaction path. We used nudged elastic band and steepest descent algorithms to obtain a dense reaction path.

Previous DFT calculations for the reaction barrier and transition state geometry [54, 20] are in good agreement with our results. The minimum energy path (MEP) displays a late barrier of 1.09 eV, which is reduced to 0.95 eV after zero-point energy corrections, and a considerable CH bond elongation was found at the transition state [54, 20] . A substantial "motion" along the different vibrational coordinates was observed on the way to the transition state. A vibrational analysis was performed along the MEP and it revealed a number of avoided crossing regions. We studied the nature (adiabatic/diabatic) of these different crossing regions in detail by calculating the Massey parameter and velocity. We found that pre-exciting the symmetric stretch vibration should be approximately 3 times as efficient at promoting reaction as pre-exciting the asymmetric stretch vibration. We also found indications as to why the vibrational bend modes are less efficient at promoting reaction than the stretch vibrations. Some of our results are similar to those from a previous study [60] in which the authors used a semi-empirical PES and a vibrationally adiabatic model. An important finding is the 'quarantining' of the vibrational energy in the methyl group in the case of the asymmetric excitation of the ν_3 mode. In the supplementary section of the chapter, we discussed the equivalence of vibrational eigenfunction and Cartesian normal mode eigenvectors, and a procedure to fit the Hessian matrix elements.

Chapter 4 describes a quantum dynamics study of methane on Ni(111) using a multiconfiguration time-dependent Hartree (MCTDH) method [61, 62] employing a full-dimensional (with respect to the CH_4 degrees of freedom) PES. The PES was created using DFT with the RPBE (revised Perdew-Burke-Ernzerhof) functional [63]. The RPBE functional gave a barrier of 1.38 eV. The modified Shepard interpolation scheme [64] was used to fit the 15D PES. In contrast to many other works in which the CH_4 was generally treated as a pseudo-diatomic [65, 66, 67], we modeled CH_4 as a polyatomic molecule. A 15D kinetic energy operator was derived that does not contain singularities in the operator and includes rotational and Coriolis couplings.

In our reduced dimensionality dynamics calculations we modeled the dissociative chemisorption of CH_4/Ni(111) at the atop site. Using some rigid constraints we derived two dimensional (2D), 3D and 4D Hamiltonians to perform the MCTDH calculations. We found that only four degrees of freedom evolve strongly along the 15D minimum energy path, viz. (1) the distance of the center of mass of the molecule to the surface, (2) the dissociative C-H bond distance, (3) the polar angle of orientation of the molecule and, (4) the bending angle between the dissociative C-H bond and the CH_3 umbrella. The comparison of our results with those of Xiang et al. [68, 69] is generally good. The helicopter motion of the CH_3 symmetry axis is found to be less efficient than its cartwheel motion at promoting the reaction. By comparing the vibrational efficacies from the 2D, 3D and 4D models, it can be seen that the efficacies of the 2D model are too small compared to the experimental results, even though the results are improved by the inclusion of a bending mode. In the 3D model, the dissociation probability appears to be an increasing function of the initial vibrational energy whatever the vibrational mode excited. The effect of the bending vibrations was correctly described in the 4D

model at intermediate collision energies (1.1-1.4 eV), where the polar orientation of the molecule is explicitly described. In addition to this, for small energies, the reactivity is almost independent of the total angular momentum J in the 4D model. Finally, our results indicate the necessity of including additional rotational and translational degrees of freedom in our model to obtain better agreement with experiments.

Chapter 5 presents six-dimensional quasi-classical dynamics calculations of nitrogen dissociative adsorption on Ru(0001). The main goal of this work was to check the applicability of the Born-Oppenheimer approximation in a prototype activated dissociation reaction. All the DFT calculations were carried out by applying the RPBE functional. The PES was fitted by applying a modified Shepard interpolation method [64]. We performed quasi-classical trajectory calculations [70], to describe the vibrational motion of the N_2 molecule.

We found that the reaction barrier is located far in the exit channel. The value of the intramolecular distance at the minimum barrier geometry (rb) is greater than the equilibrium bond distance by 1.3a0 for N_2/Ru(0001) (rb≈3.4a0). The DFT barrier is found to be very high (≈ 2 eV). According to our calculations the low reactivity of the N_2/Ru(0001) system is a result of the large corrugation and anisotropy of the PES near the minimum barrier. The theoretical and experimental angular scattering distributions show a similar behavior. In addition to this, our results show a small excitation of the translation parallel to the surface increasing with incidence energy of the molecule. However, rotational and vibrational excitation are overestimated by our theoretical calculations. Our calculations suggest that at the highest incidence energies considered, e-h pair excitations diminish the reactivity by no more than a factor of 3, in contrast to the two orders of magnitude suggested by the previous low-dimensional calculations of Diekhoner et al [43, 58]. Comparison to these low-dimensional calculations shows the importance of taking into account the multidimensional effects of N_2 rotation and translation parallel to the surface.

1.7 Outlook

In Chapter 3, we discussed the role of the fundamental vibrations of methane to promote the dissociative chemisorption of CH_4 on the Ni(111) surface employing the PW91 functional. Comparing these results to those of plane wave DFT calculations [71] using the RPBE functional, we found that the PW91 and RPBE functionals give similar frequencies and crossing regions. However, the PW91 functional seems slightly more suitable since it does not overestimate the reaction barrier, which is related to the theoretical molecular velocity along the reaction coordinate. The major challenge we faced in this project was the presence of numerical noise in the Hessian matrix elements, due to inaccuracies in the DFT gradients arising from the grid-representation to calculate exchange-correlation energies [72]. Although the noise in the forces can be reduced by using fitting methods, the DFT codes that calculate Hessians analytically by the linear response formalism give more accurate Hessians [71]. From this work we learned the importance of using the point-group symmetry of the reacting molecule-surface system to analyze the characters of the different vibrational modes, which are very sensitive to the

molecule-surface geometry. Since our vibrational analysis was based on the harmonic approximation, the role of the vibrationally overtone states [60] could not be addressed properly. One approach to solve this issue would be to find a method to obtain the vibrational wavefunction of CH_4 for the overtones or combination vibrations without the knowledge of a full-dimensional PES.

A similar approach to study the effect of vibrational modes and its coupling to the reaction coordinates for gas-phase systems is reported elsewhere [73]. This method is based on Coriolis and curvature coupling constants, which were obtained from similar numerical data as used in our work (i.e., MEP geometries, energies, forces and Hessian matrices). These quantities can also be used to construct a 'reaction path Hamiltonian' (RPH) [74], which eventually can be used to calculate the rate of the reaction as a function of temperature. Since statistical models are based on the wrong assumptions, the RPH approach would be an alternative to calculate the rate constant. Interestingly the RPH approach is now well established for handling multidimensional systems [75]. Trying one or several of these approaches for molecules interacting with surfaces would be an important step forward for understanding the role of vibrational excitations on the reactivity [76].

It would also be interesting to study the changes in the molecular orbitals during reaction. For example, the reaction path calculations showed that the hydrogen atom moved to the hcp site earlier than the CH_3 fragment to the fcc site. A charge density difference plot could possibly add to the understanding of this finding based on the concept of charge redistribution [4] of the molecular fragments. Furthermore, it would be interesting to seek an explanation of why the Ni atom moves out of the surface (in the CH_4–Ni transition state geometry) in terms of the charge densities.

In Chapter 4 we presented some quantum dynamics results for the CH_4/Ni(111) system. Although we used a full-dimensional PES (with respect to the CH_4 degrees of freedom), we treated only up to four degrees of freedom in the dynamics. A major approximation we made was that we used a frozen nickel surface. Several studies from the Jackson group indicate the involvement of the Ni atoms during the dissociation process [77, 49]. Likewise, recent quantum dynamical calculations using the surface oscillator model to include phonons clearly showed that phonons affect the barrier height [49]. Thus, a natural step to extend our efforts would be to go beyond the static surface model in the description of the dissociation dynamics. Another natural step would, of course, be to increase the number of degrees of freedom of CH_4 treated in the dynamics. The necessity of high-dimensional studies has already been pointed out by the early works of Luntz and Harris [65] and Carré and Jackson [67].

Another step would be to improve our PES by e.g. adding more points, especially near the transition state and in the exit channel. An 'n-mode' representation [78] of the PES could be necessary for future MCTDH calculations, because a non-separable PES with more than 6 degrees of freedom cannot be used in MCTDH in its most efficient form. In this work we treated methane as a polyatomic molecule. By including even more degrees of freedom one opens up the possibility for studying many different properties. For example it could be possible to study the effect of combined excitation of stretch and bend states of CH_4 on reactivity.

In Chapter 5 we described the result of quasi-classical trajectory calculations on

the dissociative chemisorption of N_2 on Ru(0001) based on a DFT PES and treating all six molecular degrees of freedom. The multidimensional effects of N_2 rotations and translations parallel to the surface dramatically lowered the reactivity of N_2 on Ru(0001) compared to earlier low-dimensional calculations. This lead to good agreement between electronically adiabatic theory and experiment, suggesting a much smaller role for nonadiabatic effects than previously assumed. This also suggests that the RPBE functional performs well in this system. Our result is in agreement with the recent findings by J. I. Juaristi et al. [79] on the 6D reactive dynamics of H_2 on Cu(110) and N_2 on W(110). Their calculations suggested that the contribution of electronic excitations is marginal and, therefore electronic adiabatic calculations are still meaningful.

It is reasonable to say that the theoretical description of nonadiabatic phenomena has not yet reached the same level of maturity as the treatment of electronic ground-state properties in the field of gas-surface chemistry. One could also aim to verify our quasi-classical dynamics results by applying quantum dynamics using the MCTDH method. Finally, in this work we used a PES based on the orthogonalized plane wave DFT [63]. However, a PES based on the projector augmented-wave DFT might be faster to calculate and prove more accurate [80].

Bibliography

[1] I. Chorkendorff and J. Niemantsverdriet, *Concepts of Modern Catalysis and Kinetics* (Wiley-VCH, Weinheim, 2003).

[2] B. H. Davis, *Handbook of Heterogeneous Catalysis*, volume 1 (Wiley-VCH, Weinheim, 1997).

[3] Nobel lecture, G. Ertl (2007).

[4] A. Gross, *Theoretical Surface Science: A Microscopic Perspective* (Springer-Verlag, Berlin, 2009).

[5] L. B. F. Juurlink, D. R. Killelea, and A. L. Utz, Prog. Surf. Sci. **84**, 69 (2009).

[6] P. Hohenberg and W. Kohn, Phys. Rev. **136**, B864 (1964).

[7] W. Kohn and L. J. Sham, Phys. Rev. **140**, A1133 (1965).

[8] D. C. Frost and C. A. McDowell, Proc. Roy. Soc. London, Ser. A **236**, 278 (1956).

[9] B. E. Smith, Science **297**, 1654 (2002).

[10] K. Honkala, A. Hellman, I. N. Remediakis, A. Logadottir, A. Carlsson, S. Dahl, C. H. Christensen, and J. K. Norskov, Science **307**, 555 (2005).

[11] J. Rifkin, *Hydrogen Economy* (Jeremy P Tarcher, New York, 2004).

[12] P. J. Chenier, *Survey of Industrial Chemistry* (Kluwer Academic, New York, 2002).

[13] L. B. F. Juurlink, R. R. Smith, and A. L. Utz, Faraday Discuss. **117**, 147 (2000).

[14] L. B. F. Juurlink, R. R. Smith, D. R. Killelea, and A. L. Utz, Phys. Rev. Lett. **94**, 208303 (2005).

[15] L. B. F. Juurlink, P. R. McCabe, R. R. Smith, C. L. DiCologero, and A. L. Utz, Phys. Rev. Lett. **83**, 868 (1999).

[16] D. R. Killelea, V. L. Campbell, N. S. Shuman, and A. L. Utz, Science **319**, 790 (2008).

[17] P. Maroni, D. C. Papageorgopoulos, M. Sacchi, T. T. Dang, R. D. Beck, and T. R. Rizzo, Phys. Rev. Lett. **94**, 246104 (2005).

[18] R. D. Beck, P. Maroni, D. C. Papageorgopoulos, T. T. Dang, M. P. Schmid, and T. R. Rizzo, Science **302**, 98 (2003).

[19] T. Nozaki, N. Muto, S. Kado, and K. Okazaki, Catalysis Today **89**, 57 (2004).

[20] P. Kratzer, B. Hammer, and J. K. Norskov, J. Chem. Phys. **105**, 5595 (1996).

[21] K. W. Kolasinski, *Surface Science: Foundations of Catalysis and Nanoscience* (John Wiley & Sons, 2008).

[22] M. Scheffler and A. Bradshaw, *The Chemical Physics of Solid Surfaces*, volume 2 (Elsevier, Amsterdam, 1983).

[23] P. J. Feibelman and D. R. Haman, Surf. Sci. **149**, 48 (1985).

[24] A. Nilsson, L. G. M. Pettersson, and J. K. Norskov, *Chemical Bonding at Surfaces and Interfaces* (Elsevier, Amsterdam, 2008).

[25] J. K. Norskov and B. Hammer, Nature **376**, 238 (1995).

[26] B. Hammer, Surf. Sci. **459**, 323 (2000).

[27] W. Brenig, Physica Scripta **35**, 329 (1987).

[28] W. Brenig, *Nonequilibrium Thermodynamics* (Springer, Berlin, 1990).

[29] A. C. Luntz, M. Persson, S. Wagner, C. Frischkorn, and M. Wolf, J. Chem. Phys. **124**, 244702 (2006).

[30] G. Henkelman, A. Arnaldsson, and H. Jonsson, J. Chem. Phys. **124**, 44706 (2006).

[31] J. Zhang, *Research and development of nickel based catalysts for carbon dioxide reforming of methane*, Ph.D. thesis, University of Saskatchewan (2008).

[32] J. Dai and J. C. Light, J. Chem. Phys. **110**, 6511 (1999).

[33] H. J. Robota, W. Vielhabera, M. C. Lin, J. Segner, and G. Ertl, Surf. Sci. **155**, 101 (1985).

[34] H. A. Michelsen, C. T. Rettner, and D. J. Auerbach, *Surface Reactions* (Springer, Beriln, 1993).

[35] J. C. Polanyi, Acc. Chem. Res. **5**, 161 (1972).

[36] C. T. Rettner, H. E. Pfnuer, and D. J. Auerbach, Phys. Rev. Lett. **54**, 2716 (1985).

[37] R. Bisson, M. Sacchi, T. T. Dang, B. Yoder, P. Maroni, and R. D. Beck, J. Phys. Chem. A **111**, 12679 (2007).

[38] H. Mortensen, L. Diekhoner, A. Baurichter, and A. C. Luntz, J. Chem. Phys. **116**, 5781 (2002).

[39] R. R. Smith, D. R. Killelea, D. F. DelSesto, and A. L. Utz, Science **304**, 992 (2004).

[40] H. L. Abbott, A. Bukoski, D. F. Kavulak, and I. Harrison, J. Chem. Phys. **119**, 6407 (2003).

[41] A. Bukoski and I. Harrison, J. Chem. Phys. **118**, 9762 (2003).

[42] L. Romm, G. Katz, R. Kosloff, and M. Asscher, J. Phys. Chem. B **101**, 2213 (1997).

[43] L. Diekhoner, L. Hornekaer, H. Mortensen, E. Jensen, A. Baurichter, V. V. Petrunin, and A. C. Luntz, J. Chem. Phys. **117**, 5018 (2002).

[44] L. Diekhoner, H. Mortensen, A. Baurichter, E. Jensen, V. V. Petrunin, and A. C. Luntz, J. Chem. Phys. **115**, 9028 (2001).

[45] M. Dohle and P. Saalfrank, Surf. Sci. **373**, 95 (1997).

[46] M. F. Somers, Ph.D. thesis, University of Leiden (2004).

[47] D. R. Killelea, V. L. Campbell, N. S. Shuman, and A. L. Utz, J. Phys. Chem. C **112**, 9822 (2008).

[48] G. Henkelman and H. Jonsson, Phys. Rev. Lett. **86**, 664 (2001).

[49] S. Nave and B. Jackson, Phys. Rev. Lett. **98**, 173003 (2007).

[50] H. Dietrich, P. Geng, K. Jacobi, and G. Ertl, J. Chem. Phys. **104**, 74704 (1996).

[51] B. Gergen, H. Nienhaus, W. H. Weinberg, and E. W. McFarland, Science **294**, 2521 (2001).

[52] J. D. White, J. Chen, D. Matsiev, D. J. Auerbach, and A. M. Wodtke, Nature **433**, 503 (2005).

[53] G. J. Kroes, Science **321**, 794 (2008).

[54] S. Nave and B. Jackson, J. Chem. Phys. **127**, 224702 (2007).

[55] A. Gross, Surf. Sci. Rep. **32**, 291 (1998).

[56] G. J. Kroes, Prog. Surf. Sci. **60**, 1 (1999).

[57] P. Nieto, E. Pijper, D. Barredo, G. Laurent, R. A. Olsen, E.-J. Baerends, G. J. Kroes, and D. Farias, Science **312**, 5770 (2006).

[58] A. C. Luntz and M. Persson, J .Chem. Phys. **123**, 074704 (2005).

[59] J. P. Perdew, J. A. Chevary, S. H. Vosko, K. A. Jackson, M. R. Pederson, D. J. Singh, and C. Fiolhais, Phys. Rev. B **46**, 6671 (1992).

[60] L. Halonen, S. L. Bernasek, and D. J. Nesbitt, J. Chem. Phys. **115**, 5611 (2001).

[61] M. H. Beck, A. Jackle, G. A. Worth, and H.-D. Meyer, Phys. Rep. **324**, 1 (2000).

[62] H.-D. Meyer, F. Gatti, and G. A. Worth, *Multidimensional Quantum Dynamics: MCTDH theory and applications* (Wiley-VCH, 2009).

[63] B. Hammer, L. B. Hansen, and J. K. Norskov, Phys. Rev. B **59**, 7413 (1999).

[64] C. Crespos, M. A. Collins, E. Pijper, and G. J. Kroes, J. Chem. Phys. **120**, 2392 (2004).

[65] A. C. Luntz and J. Harris, Surf. Sci. **258**, 397 (1991).

[66] A. P. J. Jansen and H. Burghgraef, Surf. Sci. **344**, 149 (1995).

[67] M. N. Carre and B. Jackson, J. Chem. Phys. **108**, 3722 (1998).

[68] Y. Xiang, J. Z. H. Zhang, and D. Y. Wang, J. Chem. Phys. **117**, 7698 (2002).

[69] Y. Xiang and J. Z. H. Zhang, J. Chem. Phys. **118**, 8954 (2003).

[70] M. Karplus, R. Porter, and R. Sharma, J. Chem. Phys. **43**, 3259 (1965).

[71] G. P. Krishnamohan, un published (2007).

[72] J. Hutter, personal discussion.

[73] J. T. Dunning and E. Kraka, *Advances in Molecular Electronic Structure Theory* (JAI press, Greenwich, 1989).

[74] W. H. Miller, N. C. Handy, and J. E. Adams, J. Chem. Phys. **72**, 99 (1980).

[75] J. Gonzalez, X. Gimenez, and J. M. Bofill, J. Phys. Chem. A **105**, 5022 (2001).

[76] S. Nave and B. Jackson, Phys. Rev. B **81**, 233408 (2010).

[77] A. K. Tiwari, S. Nave, and B. Jackson, Phys. Rev. Lett. **103**, 253201 (2009).

[78] J. M. Bowman, S. Carter, and X. Huang, Int. Rev. Phys. Chem. **22**, 533 (2003).

[79] J. I. Juaristi, M. Alducin, R. D. Muino, H. F. Busnengo, and A. Salin, Phys. Rev. Lett. **102**, 109602 (2009).

[80] G. Kresse and D. Joubert, Phys. Rev. B **59**, 1758 (1999).

Chapter 2

Review of the theoretical methods

In this chapter a brief overview of all the major theoretical methods used in this thesis is presented. Section 2.1 illustrates the Born-Oppenheimer approximation. In Section 2.2 the overview of plane-wave density functional theory is provided along with pseudopotential and projector augmented plane wave (PAW) approximations. The nudged elastic band method to obtain the reaction path and transition state along with different optimization methods are presented in Section 2.3. The theory of the vibrational normal modes is reviewed in Section 2.4. The interpolation scheme for the potential energy surface (PES) is described in Section 2.5. Finally, in Section 2.6 classical dynamics is reviewed and the last Section, 2.7, covers the aspects of quantum dynamics and MCTDH method.

2.1 The Born-Oppenheimer approximation

The Hamiltonian of an electronic system determines the energy of the system. Although a complete Hamiltonian for a molecule is easily determined, the resulting Schrödinger equation is very difficult to solve, due to the multidimensional nature of the problem. A standard approximation to solve this problem is to separate the nuclear and electronic degrees of freedom. Since the mass of the nuclei is considerably heavier than that of the electrons, it can be assumed that the electrons will respond 'instantaneously' to the nuclear coordinates. This approximation is called the Born–Oppenheimer (BO) or adiabatic approximation [1]. This idea allows one to treat the nuclear coordinates as parameters. For many condensed matter systems, this presumption is a reasonable approximation.

The non-relativistic molecular Hamiltonian operator for a system of nuclei and electrons can be written with usual notations as,

$$
\begin{aligned}
\hat{H} = &-\frac{\hbar^2}{2} \sum_{I=1}^{N} \frac{\nabla_I^2}{M_I} - \frac{\hbar^2}{2m} \sum_{i=1}^{n} \nabla_i^2 - \sum_{I=1}^{N} \sum_{i=1}^{n} \frac{Ze^2}{r_{i,I}} \quad + \\
&\sum_{I=1}^{N} \sum_{J=1}^{N'} \left[\frac{Z_I Z_J e^2}{r_{I,J}} \right] + \sum_{i=1}^{n} \sum_{j=1}^{n'} \left[\frac{e^2}{r_{i,j}} \right],
\end{aligned}
\tag{2.1}
$$

where m is the mass of the electron, M_I is the mass of the $I'th$ nucleus, N is the number of nuclei and n is the number of electrons. We can write Eq. 2.1 into a simple form, *viz.*,

$$\hat{H} = \hat{T}_N + \hat{T}_e + \hat{V}_{Ne} + \hat{V}_{NN} + \hat{V}_{ee}. \tag{2.2}$$

Here, $\hat{T}_N$ and $\hat{T}_e$ are the kinetic energies of the nuclei and of the electrons, respectively. $\hat{V}_{Ne}$ and $\hat{V}_{ee}$ denote the electron - nuclei attraction and electron - electron repulsion energies, and $\hat{V}_{NN}$ represents the nucleus - nucleus repulsion energy. The time-independent Schrödinger equation of the system is written as,

$$\hat{H}\Psi(r_i, R_I) = E\Psi(r_i, R_I). \tag{2.3}$$

Here, $\Psi(r_i, R_I)$ represents the complete eigenfunction of $\hat{H}$ and is a function of the electronic (r_i) and nuclear (R_I) positions.

As the mass of the proton is about 1840 times that of the electrons, a first approximation is to assume the nuclei to be stationary with respect to the electrons. This assumption readily suggests that in solving for the electronic motion one can neglect the kinetic energy of the nuclei ($\hat{T}_N$). Additionally, it allows us to write the full eigenfunction in a *seperable* form as,

$$\Psi(r_i, R_I) = \phi(r_i, \{R_I\})\chi(R_I). \tag{2.4}$$

In Eq.2.4, $\phi(r_i, \{R_I\})$ is an electronic wavefunction that parametrically depends on the nuclear positions while $\chi(R_I)$ is the nuclear wavefunction. Using the above expression, one can set up the Schrödinger equation for the nuclei and for the electrons, seperately. In other words, the Schrödinger equation for electrons is written as,

$$[\hat{T}_e + \hat{V}_{Ne} + \hat{V}_{ee} + \hat{V}_{NN}]\phi(r_i, \{R_I\}) = U_n(\{R_I\})\phi(r_i, \{R_I\}) \tag{2.5}$$

and that for the nuclei is,

$$[\hat{T}_N + U_n(\{R_I\})]\chi(R_I) = E_\chi \chi(R_I). \tag{2.6}$$

In the above equations, $U_n(\{R_I\})$ is the electronic energy at fixed nuclear coordinates. E_χ is the eigenvalue of the nuclear wavefunction. It should be noted that the $\chi(R_I)$ describes the nuclear motions like rotations, vibrations and translations. In BO approximation, the changes in the energies of the electrons in molecules that are brought about by nuclear motions are essentially adiabatic. This also shows that the interatomic potentials and forces are only functions of the nuclear positions.

2.2　The gas-surface interaction

In this study the gas-surface electronic interaction plays a major role. This interaction potential is needed to generate further derived quantities and/or observables to describe the system. This interaction potential is calculated by the density functional theory (DFT), within the Born-Oppenheimer approximation. DFT is currently one of the most successful electronic structure theories for the large systems. The main aspects of plane-wave DFT and its subsequent features are reviewed in the below subsection.

2.2.1   The outline of the density functional theory

DFT is formulated by P. Hohenberg and W. Kohn in 1964 [2], by proving that: (1) The external potential and hence the ground state energy of the system can be uniquely determined by the ground state electron density, or this energy is a functional of the electron density. One immediate consequence of this theorem is that the familiar relation of the ground state density can be reversed *i.e.* $\psi_0 = \psi_0[n_0]$, where ψ_0 and n_0 are the ground state electronic wavefunction and density, respectively. (2) The electron density variationally minimizes the total energy of the system, in other words, the determination of the exact ground state is possible. Thus an N-electron Schrödinger wave equation can be written within the Born-Oppenheimer approximation as,

$$\hat{H}\psi_0 = \left[\hat{T} + \hat{V} + \hat{U}\right]\psi_0 = \left[\sum_i^N -\frac{\hbar^2}{2m}\nabla_i^2 + \sum_i^N V(\mathbf{r}_i) + \sum_{i<j} U(\mathbf{r}_i, \mathbf{r}_j)\right]\psi_0 = E\psi_0.$$
(2.7)

Here, $\hat{H}$ is the electronic molecular Hamiltonian, N is the number of electrons and $\hat{U}$ is the electron-electron interaction. The operators $\hat{T}$ and $\hat{U}$ are 'universal operators' because they are independent of the system, while $\hat{V}$ is generally an external (Coulombic) potential which is system dependent. Following Hohenberg and Kohn, we can represent any ground state property, O as

$$\langle O \rangle[n_0] = \langle \psi_0[n_0] \mid \hat{O} \mid \psi_0[n_0] \rangle,$$
(2.8)

where n_0 is the ground state electron density. The ground state energy can be represented as,

$$E[n_0] = \left\langle \psi_0[n_0] \left| \hat{T} + \hat{V} + \hat{U} \right| \psi_0[n_0] \right\rangle.$$
(2.9)

Since V is the only functional which is system dependent, we can write a general expression of $E[n]$,

$$E[n] = T[n] + U[n] + \int V(\mathbf{r})n(\mathbf{r})\mathrm{d}^3\mathbf{r} = F_{HK}[n] + \int V(\mathbf{r})n(\mathbf{r})\mathrm{d}^3\mathbf{r}$$
(2.10)

where F_{HK} is an universal functional.

This expression can be minimized to get n_0 and hence all the ground state properties. More interestingly the above expression has an integral over three dimensions, so that the integration schemes became more simpler and cheaper compared to that of many-body wavefunction methods (where the equivalent integrals are tedious due to the $3N$ dimensionality).

2.2.2   Kohn-Sham formulation

W. Kohn and L. J. Sham proposed a self-consistent minimization scheme to minimize $E[n]$, thus making DFT calculations possible for real systems [3]. It start with non-interacting system of electrons with an external potential. Furthermore in this system $U = 0$, and $T = T_s[n]$, where $T_s[n]$ is the non-interacting kinetic energy. Then Eq. 2.10 can be rewritten as,

$$E_s[n] = \int V_s(\mathbf{r})n(\mathbf{r})d^3\mathbf{r} + T_s[n] \tag{2.11}$$

and corresponding exchange and correlation (xc) energy is defined by

$$E_{xc} = F_{HK}[n] + T_s - \int \frac{\rho(\mathbf{r_1})\rho(\mathbf{r_2})}{|\mathbf{r}_1 - \mathbf{r}_2|}d\mathbf{r}_1 d\mathbf{r}_2. \tag{2.12}$$

The *xc* potential can now be written as

$$V_{xc}(\mathbf{r}) = \frac{\delta E_{xc}[n]}{\delta n[\mathbf{r}]}. \tag{2.13}$$

From the above three equations one can set up an expression for the non-interacting external potential or 'effective' potential as,

$$V_s(\mathbf{r}_1) = V(\mathbf{r}_1) + \int \frac{\rho(\mathbf{r_2})}{|\mathbf{r}_1 - \mathbf{r}_2|}d\mathbf{r}_2 + V_{xc}(\mathbf{r}_1). \tag{2.14}$$

Eq. 2.14 forms N one particle Kohn-Sham (KS) set of coupled differential equations [4]:

$$\left(-\frac{\nabla^2}{2} + V_s(\mathbf{r})\right)\psi_i(\mathbf{r}) = \varepsilon_i\psi_i(\mathbf{r}). \tag{2.15}$$

These equations can be solved iteratively yielding eigenvalues or KS orbital energies $\{\varepsilon_i\}$ and eigenfunctions or one electron KS orbital functions $\{\psi_i\}$. The density is calculated by summing up all the occupied KS orbitals,

$$n_0 = \sum_{i=1}^{N} |\psi_i|^2 \tag{2.16}$$

An important aspect of the KS formulation is that it implicitly includes the treatment of the *xc* part. For many systems this makes a DFT calculation readily comparable with -say, an MP2 level of theory with a computational cost of HF method [4]. The choice of a suitable functional form is a very important step in any DFT calculation. In this work GGA (generalized gradient approximation) type functionals are used *viz.* PW91 [5, 6] and RPBE [7]. GGA approximates the *xc* energy via

$$E_{xc} = \int \epsilon_{xc}(n, \nabla n)n(\mathbf{r})\mathrm{d}^3\mathbf{r}, \tag{2.17}$$

where ϵ_{xc} is the exchange-correlation energy density.

2.2.3 Plane-wave DFT.

A planewave basis set is a natural choice for the basis set to solve the Kohn-Sham equations for spatially extended systems like metals, polymers etc. Using the translational symmetry of the atomic arrangements, the form of the effective potential for an extended system can be written as,

$$V_{eff}(\mathbf{r} + \mathbf{T}) = V_{eff}(\mathbf{r}), \tag{2.18}$$

where $\mathbf{r}$ and $\mathbf{T}$ are the arbitrary and (direct-) lattice vectors, respectively. By virtue of the Bloch's theorem, eigenfunction of such system can be written as a product of a plane wave and a periodic function *viz.*,

$$\psi(\mathbf{r} + \mathbf{T}) = e^{i\mathbf{kT}}\psi(\mathbf{r}). \tag{2.19}$$

In the above equation, $\mathbf{k}$ is a wave vector and it is restricted to be within the first Brillouin zone (BZ). Eq. 2.19 can be stated in an alternative form such that all eigenfunctions of single-particle Schrödinger equation with a periodic potential can be written in terms of a periodic function $u_{\mathbf{k}j}$ modulated by a plane wave with wave vector $\mathbf{k}$. Equivalently, this can be expressed for each and every band index, j such that

$$\psi_{\mathbf{k}j}(\mathbf{r}) = e^{i\mathbf{kr}}u_{\mathbf{k}j}(\mathbf{r}). \tag{2.20}$$

By assuming this eigenfunctions to be normalized with respect to the unit cell, the periodic function $u_{\mathbf{k}j}$ can be expanded in a Fourier series:

$$u_{\mathbf{k}j}(\mathbf{r}) = \sum_{\mathbf{G}} c_{\mathbf{G}}^{\mathbf{k}j} e^{i\mathbf{Gr}}. \tag{2.21}$$

Here, $\mathbf{G}$ is a lattice vector defined in the reciprocal space under the condition, $\mathbf{G}.\mathbf{T} = 2\pi n$, where n is any integer. Now the Kohn-Sham equation (Eq. 2.15) can be re-written as

$$\left(-\frac{\nabla^2}{2} + V_{eff}(\mathbf{r}) \right) \psi_{\mathbf{k}j}(\mathbf{r}) = \varepsilon_{\mathbf{k}j}\psi_{\mathbf{k}j}(\mathbf{r}), \tag{2.22}$$

where $\varepsilon_{\mathbf{k}j}$ is the Kohn-Sham eigenvalue of the band j.

$V_{eff}(\mathbf{r})$ can be easily decomposed into the following functionals of the density as,

$$V_{eff}(\mathbf{r}) = V_{ext}(\mathbf{r}) + V_H[n(\mathbf{r})] + V_{xc}[n(\mathbf{r})],$$

in which $V_{ext}(\mathbf{r})$, $V_H[n(\mathbf{r})]$ and $V_{xc}[n(\mathbf{r})]$ are the external potential of the nuclei, the Hartree and the exchange-correlation potentials, respectively. The $n(\mathbf{r})$ is the ground state electron density defined as,

$$n(r) = 2\frac{\Omega_c}{(2\pi)^3}\sum_j \int_{BZ} |\psi_{\mathbf{k}j}(\mathbf{r})|^2 \Theta(E_F - \epsilon_{\mathbf{k}j}) d^3\mathbf{k}, \tag{2.23}$$

where, Ω_c is the volume of a unit cell, E_F is the Fermi energy and Θ is a Heaviside step function (which is one for positive and zero for negative arguments) and are excluded the eigenvectors corresponding to empty states from the sum.

For practical purpose, the above equation is approximated - *i.e.* the integrals are discretized and are written as,

$$2\frac{\Omega_c}{(2\pi)^3}\sum_j \int_{BZ} ...\Theta(E_F - \epsilon_{\mathbf{k}j}) d^3\mathbf{k} \rightarrow \frac{1}{N_{kpt}}\sum_{\mathbf{k}} f_{\mathbf{k}j}..., \tag{2.24}$$

where $f_{\mathbf{k}j}$ are the occupation number taking values of either zero or one and N_{kpt} is defined as a regular mesh consisting of k-points. There are several schemes proposed to construct such meshes in the literature [8, 9]. The major advantage of this approximation is that only a finite number of k-points are needed to evaluate the charge density and hence the total energy of the system. Another consequence of this approach is that the larger the super cells (which defines the boundary condition), the fewer k-points are needed to perform the calculation. This can be interpreted, because the Brillouin cell becomes smaller in the reciprocal space when a larger supercell is used.

By virtue of the plane wave basis set, a Fourier representation of the Kohn-Sham equations (Eq. 2.15) is possible. By inserting Eq. 2.21 into Eq. 2.15 and multiplying the left-hand-side with $e^{-i(\mathbf{k}+\mathbf{G}')\mathbf{r}}$ and integrating over $\mathbf{r}$, one gets a matrix eigenvalue equation:

$$\sum_{\mathbf{G}}(\frac{\hbar^2}{2m}) \parallel \mathbf{k}+\mathbf{G} \parallel^2 \delta_{\mathbf{G}'\mathbf{G}} + V_{eff}(\mathbf{G}'-\mathbf{G})c_{\mathbf{G}}^{\mathbf{k}j} = \epsilon_{\mathbf{k}j}c_{\mathbf{G}'}^{\mathbf{k}j}. \qquad (2.25)$$

In practice the Fourier expansion (Eq. 2.21) of the wave function is truncated using a kinetic energy cut-off defined in terms of plane wave vectors $(\mathbf{k}+\mathbf{G})$. This cut-off energy, E_{pw} is defined as below,

$$(\frac{\hbar^2}{2m}) \parallel \mathbf{k}+\mathbf{G} \parallel^2 \leqq E_{pw}. \qquad (2.26)$$

E_{pw} is one of the most important parameters and hence it should be converged reasonably well.

The next major approximation used in plane wave DFT is the use of pseudopotentials. Although core electrons do not participate in chemical bonding as they are strongly localized around the nucleus, the rigorous representation of these electrons in the PW scenario is a difficult task. For example, the oscillatory wave function of the core electron (see Φ_{AE} in the Fig. 2.1) requires a large number of plane waves and hence its calculations becomes practically unfeasible. This situation can be avoided by neglecting the orthogonal relationship of the core-valence electrons using a non-local potential, called a pseudopotential. The solutions of the resulting approximation (pseudo-orbitals) are very close to the valence orbitals in the outer regions of the systems but lack many oscillations (*i.e.* nodeless valence wavefunctions) in the core regions required for the core-valence orthogonality.

The main parameter to decide the accuracy of the pseudopotential approach is the cut-off radius ($\mathrm{R_{cut}}$) where the Columb potential from the pseudopotentials and bare Coulomb potential of the system has the same value. Thus the pseudo orbital will match the corresponding all electron orbital outside this point as indicated in Fig. 2.1. By reducing $\mathrm{R_{cut}}$ one can make a more accurate pseudopotential ('hard' pseudopotential) but at the same time the DFT calculations becomes computationally more expensive. This technical difficulty can be handled by using Vanderbilt ultrasoft pseudo-potentials [10, 11]. In this approach, fewer plane waves are required in expansions of the electron valence states by relaxing the norm-conservation (of the valence pseudo orbitals) criteria.

In this work we have used two plane wave codes: DACAPO [12] and VASP [13, 14, 15, 16]. The DACAPO is an orthogonalized plane wave (OPW) code
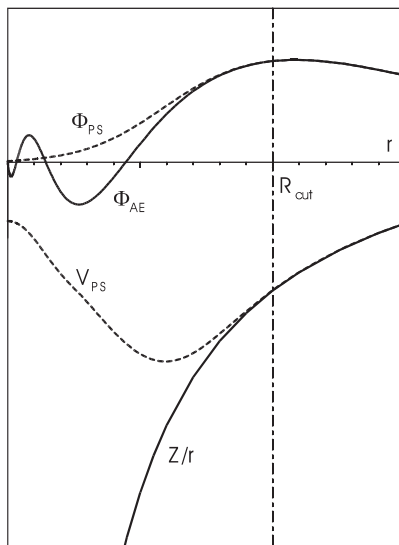
Figure 2.1: A Schematic diagram of the PSP approach. The all electron wavefunction, Φ_{AE} is approximated with the pseudo wavefunction Φ_{PS} and the correspoding all electron potential Z/r is replaced by the pseudo potential, V_{PS}.

and it uses a plane wave basis for the valence electronic states and describes the core-electron interactions with Vanderbilt ultrasoft pseudo-potentials. The VASP code also uses plane wave basis set but the interaction between ions and electrons can be described by the projector-augmented wave (PAW) method [17, 18]. The PAW approach is superior to OPW methods [19] since it preserves the local node structure of orbitals in its scheme, in other words, it treats the inner- electronic wavefunction.

2.3   Reaction path calculation

The reaction path (RP) can be a miniature representation of the whole PES, by connecting initial, final and transition states with a suitable reaction coordinate. Though there is no universal method to locate the TS or to obtain a reaction path, there are a variety of useful alternative methods [20]. Here an outline of the nudged elastic band (NEB) method and optimization schemes are presented.

2.3.1   The Nudged elastic band methods

The nudged elastic band (NEB) is one of the 'iterative' methods to find the reaction path and/or the transition state [21, 22, 23]. The NEB defines a minimum energy path (MEP) by connecting, generally, two minima on the PES.

In the NEB method, as a first approximation, an initial elastic band is made by a linear interpolation between the initial and final configurations. This band consists of a number of geometries, called 'images'. Then the force acting upon an image i is,

$$F_i^{NEB} = -\nabla V(R_i) + F_i^{s||},\tag{2.27}$$

where

$$F_i^{s||} = k_{i+1}(R_{i+1} - R_i) - k_i(R_i - R_{i-1}). \tag{2.28}$$

In the above equations, R_i is the Cartesian geometry of an image i and k_i is a 'spring constant' between $R_i - R_{i-1}$ and it defines the stiffness of the harmonic spring (or an 'elastic band') connecting these images. Since F_i^{NEB} has two independent terms it can be written as,

$$F_i^{NEB} = F_i^{\perp} + F_i^{s||}, \tag{2.29}$$

where $F_i^{\perp}$ and $F_i^{s||}$ (See Fig. 2.2) are the perpendicular and parallel force components to the band, respectively. By defining a tangent vector of an image $\hat{\tau}_i$ along the MEP, the above components can be written as,

$$F_i^{\perp} = -\nabla V(R_i) + (\nabla V(R_i).\hat{\tau}_i)\hat{\tau}_i \tag{2.30}$$

and

$$F_i^{s||} = (k_{i+1}(R_{i+1} - R_i) - k_i(R_i - R_{i-1}))\hat{\tau}_i. \tag{2.31}$$
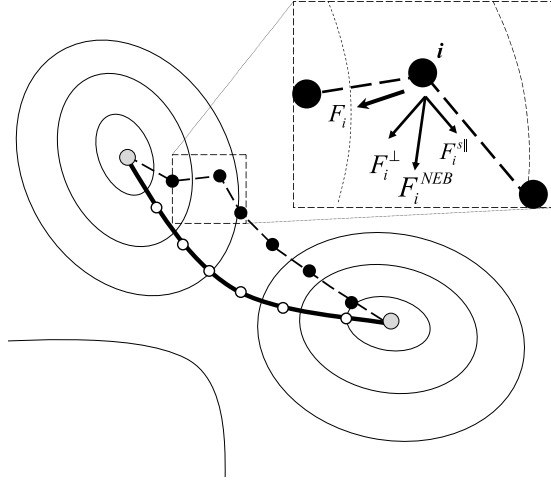
Figure 2.2: The initial (black dots) and final (circles) images of a NEB calculation. The different force components of an image i are shown in the inset.

Since an image along the MEP satisfies a necessary condition, *i.e.*, $F_i^{\perp} = -\nabla V(R_i) + (\nabla V(R_i).\hat{\tau}_i)\hat{\tau}_i = 0$, a minimization algorithm can be applied to move the initial images in the direction defined by $F_i^{\perp}$. This process can be iterated until all the images in the calculation lie on the MEP. The convergence rate of a NEB calculation is mainly dependent on the closeness between the true MEP and its initial estimate and the number of images.

Several modifications of the NEB have been developed, such as climbing-image NEB [24] and Adaptive-NEB [25], to give an accurate estimate of the saddle point.

2.3.2 Optimization methods

The methods described above use the optimization or minimization of the forces with or without constraints. Thus a short review of these methods is presented here. Fig. 2.3 shows an illustration of the common optimization methods applied to the two dimensional Rosenbrock function ($f(x, y) = (1 - x)^2 + 100(y - x^2)^2$), which is widely used as a test function for optimizing problems [26, 27].

- Steepest descent:

  The steepest descent (SD) method is the simplest and the slowest method among the optimization methods discussed. The gradient - or the force components - are used to find the directions of the displacement vector, which can be represented as,

  $$x_{n+1} = x_n - h_i \nabla V(x_n), \, n \geq 1.$$

  where x_n is the sequence of points which converged to a local minimum, h_i is the step size, which is usually positive and an order of magnitude less than unity, and $\nabla V(x_n)$ is the gradient at the point x_n.

- Quasi-Newton:

  The Quasi-Newton (QN) method is an improved version of Newton's iterative method, which requires a second derivative matrix (Hessian). This method does not require the Hessian matrix explicitly, but an approximated inverse of the Hessian matrix, Q, and the derivative matrix. Several implementations are available for QN to update the Q matrix, for example the BFGS (Broyden, Fletcher, Goldfarb, Shanno) scheme. This scheme may be written as,

  1. $d^n = -Q^n \nabla V(x_n)$
  2. $\alpha_n = \frac{-\nabla V(x_n)^T \cdot d^n}{d_k^T Q^n d_n}$ (Wolfe's condition)
  3. $x_{n+1} = x_n + \alpha_n d^n, \, n \geq 1.$

  where d^n is the direction vector and α_n is the variable step length which is usually obtained by a line search procedure, by minimizing $\nabla V(x_n)^T \cdot d^n$.

- Conjugate gradient:

  In the conjugate gradient method, the direction of descent is obtained by using the previous 'conjugate' (or linearly independent) directions and the present SD direction. The attractive feature is that it does not require any knowledge of the Hessian matrix. The general description of the iterations is as follows:

  1. $\beta = \frac{[\nabla V(x_n)]^T \nabla V(x_n)}{[\nabla V(x_{n-1})]^T \nabla V(x_{n-1})}$ (Fletcher-Reeves formula)
  2. $d^n = -\nabla V(x_n) + \beta d^{n-1}$
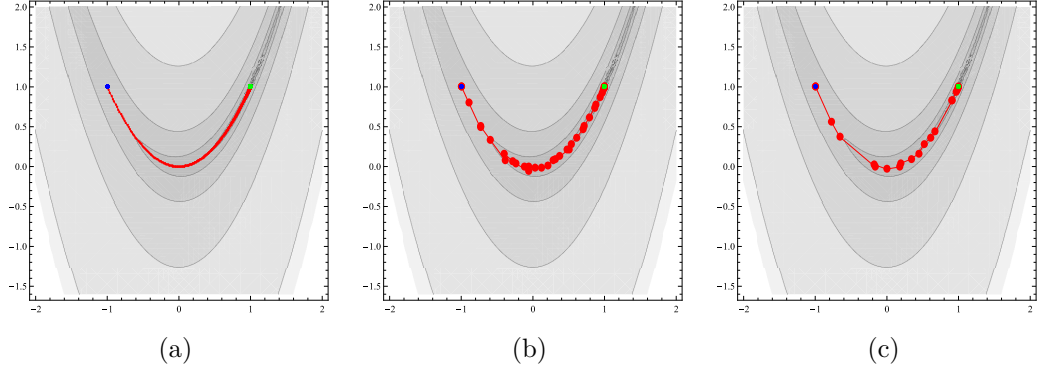
Figure 2.3: Contour plots of Rosenbrock function of two variables with different minimizers. The paths are started at [-1,1] and terminated at its global minimum [1,1]. The steepest descent path (a) converges with 724 steps, the quasi-Newton method (b) with 38 and the conjugate gradient method (c) with 22 steps.

$$3.\ x_{n+1} = x_n + d^n,\ n \geq 1.$$

2.4   Vibrational normal modes

The vibrational energy of a molecule is one of the three main quantized internal energies, apart from the electronic and rotational energies. Many physically interesting and important properties like zero point energy are related to the vibrational motion of the molecule. In this section a small description of vibrational normal modes is provided.

A molecule can be considered as a N-coupled mass points and thus viewed as a coupled simple harmonic oscillator system - a dynamic system vibrating according to Hooke's law. This N-atom oscillator can be then described by the Lagrangian, L as

$$L = T - V, \tag{2.32}$$

where T and V are the kinetic and potential energy terms. To solve this, particularly in a 'normal mode' approach, one can define a set of mass-weighted normal mode coordinates, q_k, $k = \{1, 2, 3..., 3N\}$ and $q_i = \sqrt{m_j}\triangle x_j$, $q_{i+1} = \sqrt{m_j}\triangle y_j$, $q_{i+2} = \sqrt{m_j}\triangle z_j...$, where j labels the atoms and i the 3N Cartesian coordinates. Using these coordinates, Eq. 2.32 can easily be uncoupled, *i.e.*, avoiding the cross terms and leaving T and V as diagonal matrices [28]. For this the above equation is first written as,

$$L = \frac{1}{2}\sum_{i=1}^{3N}\dot{q}_i^2 - \frac{1}{2}\sum_{i,j=1}^{3N}\left.\frac{\partial V}{\partial q_i \partial q_j}\right|_0 q_i q_j, \tag{2.33}$$
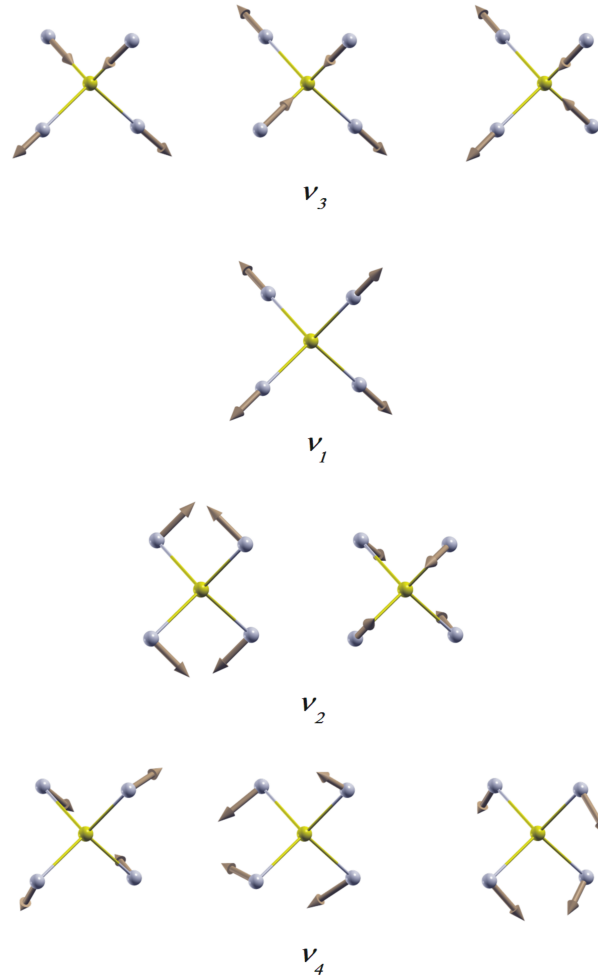
Figure 2.4: The nine vibrational normal modes of methane are plotted with the degenracies and displayed in the descending order in the vibrational energy.

or in vector-matrix form as,

$$L = \frac{1}{2}\dot{q}^t\dot{q} - \frac{1}{2}q^tFq. \tag{2.34}$$

Here, the superscript, t indicates the transpose and F is the second derivative or the Hessian matrix. The above equation determines the dynamics of the vibrating system. The F can be computed by taking numerical derivatives instead of the analytical gradients. Since F is a symmetric matrix, an orthogonal or similarity transform is exists to diagonalize F :

$$W^tFW = \Omega, \tag{2.35}$$

where Ω is the diagonal matrix, W is a matrix of order 3N, and $W^tW = I$, where I is an identity matrix. Eq. 2.35 is nothing but an eigenvalue equation, where each element of Ω is an eigenvalue (harmonic frequency) associated with a specific column of W, the normal mode.

There are 9 vibrational normal modes present in theCH$_4$ system. From the point group analysis of the T_d character table of the methane one can see that the

symmetry species of the normal modes of methane:

$$\Gamma_{CH_4} = A_1 + E + 2T_2. \tag{2.36}$$

Here, A_1, E and T_2 are the irreducible representations in which the T_2 modes are infrared and Raman active while the A_1 and E modes are only Raman active. The mode E is doubly degenerate and the T_2 modes are triply degenerate. Using spectroscopic notations, we can represent these modes as ν_1, ν_2, ν_3 (ν_4) for A_1, E and T_2, respectively. The ν_1 mode describes the symmetric stretch mode, ν_2 represents symmetric bend modes, ν_3 corresponds to the asymmetric stretches and ν_4 describes the asymmetric bending modes (see Fig. 2.4). The below table lists the normal mode frequencies of these vibrations [29].

CH_4 normal modes	Frequencies (cm^{-1})
ν_1	2916
ν_2	1533
ν_3	3019
ν_4	1311

2.5   Growing the potential energy surface

The reaction dynamics of a system can be elucidated if a PES of the system is known, by performing classical and quantum scattering calculations. Obtaining and fitting the PES, especially for a high dimensional system $CH_4/Ni(111)$ is a computationally demanding task. In this work, we employed the GROW code [30, 31, 32] which is based on the modified Shepard (MS) interpolation method to fit the DFT potential energy surface. The computational cost is reduced by applying the following approximations (1) the surface atoms are taken as frozen (the static-surface model), and (2) the use of the Born-Oppenheimer approximation (neglecting electron-hole pair excitations).

2.5.1   Electronic structure calculations

The DFT calculations are carried out using the DACAPO code [12]. The generalized gradient approximation is used to describe the exchange-correlation energy of the electrons. We used the RPBE functional [7] for the GGA and it was constructed from the PBE functional to satisfy a constraint upon approximate exchange-correlation functionals - the Leib-Oxford bound[33]. Many DFT studies in various gas-surface reactions show that the functional gives better chemisorption energies than the PBE functional [7]. The ion cores are approximated using ultrasoft pseudo-potentials and a plane-wave basis set is used for the electronic orbitals.

2.5.2 Modified Shepard interpolation method

We used the modified Shepard (MS) interpolation method extended to gas-surface reactions by Crespos *et al.* to grow the PES [34]. In this method, interpolated data are calculated by a weighted series of Taylor expansions centered on DFT data points, sampled throughout the configuration space of the system. To monitor the growth of the PES, the convergence of the reaction probability of interest is calculated. The main feature of the MS method is that the new points are added only to the dynamically relevant region of configuration space. This thus avoids the use of regular grids and DFT optimizations.

To define the configuration space, a symmetry unique triangle is defined (see Fig 2.5). To construct this triangle, the approximation was made that the interaction of CH_4 with the fcc site is equal to the interaction of CH_4 with the hcp site. Inverse interatomic distances, $Q_i = 1/R_i$, are used as coordinates in this method and the vector defining any configuration of the system is given by $\mathbf{Q} = \left(1/R_1, \ldots, 1/R_{n(n-1)/2}\right)$, where n is the number of atoms used to describe the system. These inverse interatomic distances are used to get a physically more reasonable behavior when two atoms are close to each other. For each geometry $\mathbf{Q}$, a set of $3n-6$ algebraically independent linear combinations of the $n\left(n-1\right)/2$ interatomic distances, $\zeta\left(\mathbf{Q}\right)$, can be defined [31] in terms of the inverse distance as,

$$\zeta_m = \sum_{k=1}^{n(n-1)/2} U_{mk}Q_k \qquad (m = 1, \ldots, 3n-6), \qquad (2.37)$$

where U_{mk} is the transformation matrix from reciprocal bond lengths to the new coordinates. Now, the potential energy at a configuration $\mathbf{Q}$ can be expanded as a second-order Taylor expansion $T_i\left(\mathbf{Q}\right)$

$$
\begin{aligned}
T_i\left(\mathbf{Q}\right) \;=\; & V\left[\mathbf{Q}\left(i\right)\right] + \sum_{k=1}^{3n-6}\left[\zeta_k - \zeta_k\left(i\right)\right]\left.\frac{\partial V}{\partial \zeta_k}\right|_{\mathbf{Q}=\mathbf{Q}(i)} \\
& +\frac{1}{2}\sum_{k=1}^{3n-6}\sum_{j=1}^{3n-6}\left[\zeta_k - \zeta_k\left(i\right)\right]\left[\zeta_j - \zeta_j\left(i\right)\right]\left.\frac{\partial^2 V}{\partial \zeta_k \partial \zeta_j}\right|_{\mathbf{Q}=\mathbf{Q}(i)}
\end{aligned}
\qquad (2.38)
$$

where $V\left[\mathbf{Q}\left(i\right)\right]$ is the potential value at $\mathbf{Q}\left(i\right)$, and the gradients at this point are computed analytically by DACAPO. The second derivatives are computed from the gradients using forward differencing using a lower level of theory, *i.e.* by applying a 2 layer Ni slab and a lower E_{pw} and a k-point grid containing less points than the values used for the potential.

The total potential energy at any configuration $\mathbf{Q}$ is then taken as

$$V\left(\mathbf{Q}\right) = \sum_{g \in G} \sum_{i=1}^{N_{data}} w_{g \circ i}\left(\mathbf{Q}\right) T_{g \circ i}\left(\mathbf{Q}\right) \qquad (2.39)$$

where $T_{g \circ i}\left(\mathbf{Q}\right)$ represents a second-order Taylor expansion and $w_{g \circ i}\left(\mathbf{Q}\right)$ a normalized weight function (see Refs. [31] and [34] for more details). N_{data} is the number of DFT data configurations in the interpolation, G is the symmetry group, and $g \circ i$ denotes the transformation of the i'th data point by the group element g. To take into account the full symmetry of the system, a sum is taken over both the DFT data points and their symmetry equivalent points.
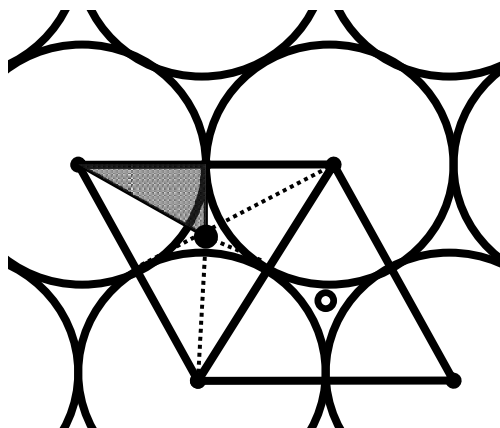
Figure 2.5: The shaded triangle represents the symmetry unique triangle of the unit cell. The large circle indicates the Ni atoms and the dark and open circle represents fcc and hcp sites respectively.

As was said before, the MS interpolation scheme adds DFT points not uniformly in the PES but only in the regions where the dynamics is apparently important. This scheme is in contrast with other interpolation methods [35, 36]. The classical trajectory method is used to find these regions by spotting the presence of the molecules during dynamics calculations. The new points are added according to one of the following criteria [30, 31, 32]: (1) The h-weight criterion, which is based on the assumption that the best location for a new point would be in the region most frequently visited by the trajectories, (2) the variance criterium, which is based on the assumption that the accuracy of the PES will be best improved if the new point is added in the region where the determination of the energy is suspected to be the most inaccurate.

2.5.3   Implementation of the MS method in GROW

An iterative procedure is used to grow the PES [30, 31, 32]. A short outline is given below.

1. An initial PES is constructed mainly from the NEB calculations, where the data set consists of optimized initial and final geometries and the transitions state. In addition to this we used a sparse set of optimized DFT CH_4 geometries distributed over the unit cell for the GROW calculation.

2. Using this initial PES a few classical trajectories (typically ten) are run. We have grown the PES using simultaneously several translational energies, to assure the accurate representation of the PES for the whole energy range of interest. Along each trajectory the molecular geometries explored by the simulation are periodically stored.

3. From the stored geometries a new point is chosen and added to the PES according to one of the two criteria described in the above section.

4. The continuation of the process: the program loops back to step 2

5. Convergence test: After about 100 points are added, the accuracy of the PES is checked by computing an accurate value of the desired observable (the reaction probability) from a more extensive classical trajectory simulation (approximately, 10 000 trajectories). The growth process is stopped when the observable is considered to be converged, within a given tolerance.

2.6 The classical trajectory method

Classical mechanics based on Newton's law of motion may provide an approximate picture of the collision dynamics of a chemical reaction. The numerical solution of Newton's equations of motion yields the position of each and every atom as a function of time, in what are called trajectories. Statistical mechanics provides a link between the macroscopic observables and the microscopic world obtained from the classical trajectory (CT) simulations via the microcanonical ensemble and its ergodic property. These relations can be written for an observable, a, as

$$\langle a \rangle = \frac{\int dx \, a(x) \delta(\hat{H}(x) - E)}{\int dx \, \delta(\hat{H}(x) - E)} = \lim_{\tau \to \infty} \int_0^\tau dt \, a(x_t) \equiv \tilde{a}. \qquad (2.40)$$

The above equation describes that the expectation value, a, of a microcanonical ensemble is equal to the time average over the classical trajectories.

Technically, several algorithms exist to perform the numerical integration and in this work, a velocity-Verlet algorithm has been used [37]. This algorithm is a simple, robust and reversible method and allows large time steps. The algorithm can be represented in terms of the variables *viz.*, position(q), force ($\mathbf{f}$), and velocity ($\mathbf{v}$) as,

$$\begin{cases} q_{n+1} = q_n + \mathbf{v}_n \delta t + \frac{\mathbf{f}(q_n)}{2m} \delta t^2 \\[2ex] \mathbf{v}_{n+1} = \mathbf{v}_n + \left(\frac{\mathbf{f}(q_{n+1}) + \mathbf{f}(q_n)}{2m} \right) \delta t \end{cases} \qquad (2.41)$$

A main initial procedure in CT method is to choose a set of initial conditions where a Monte Carlo sampling method is used to simulate the molecular initial conditions for each set of initial parameters (such as translational, rotational energies etc).

In the quasi classical trajectory (QCT) method the initial zero point energy (ZPE) of the molecule is included in the dynamics [38]. This method allows us to include quantum effects in the classical simulation in an approximate way. The QCT is susceptible to the so-called ZPE violation problem but for an activated system this problem is expected to play a minor role at energies above the threshold to reaction [39]. The QCT method generally gives accurate results for activated molecule-surface reactions [40, 41, 42, 43, 44]. This is mainly achieved by treating the 'vibrational softening' (adiabatic transfer of energy from internal to translational motion which takes place when a molecule approaches the surface) in the QCT method [45].

2.7 Quantum Dynamics and MCTDH method

2.7.1 Quantum dynamics: general concepts

To extract the details of the reaction dynamics at the quantum level, one needs to solve the Schrödinger equation of motion of the atomic nuclei:

$$i\hbar\frac{\partial \Psi(R,t)}{\partial t} = \hat{H}(R,t) = (\hat{T}_n + E(R))\Psi(R,t). \tag{2.42}$$

Here, $\hat{T}_n$ is the KE operator of the nuclei, $E(R)$ is the electronic energy (*i.e.* Potential energy from the PES), and $\Psi(R,t)$ represents a time dependent wavefunction of all the nuclear coordinates, R.

Since the time dependent Schrödinger equation (TDSE) is a linear-hyperbolic differential equation it is an initial value problem. In other words, to calculate the time evolution of the system only the initial state specification is needed. If the $\Psi(R,t_0)$ is known, then the general solution to the above Eq. 2.42 is given by,

$$\Psi(R,t) = \hat{U}(t - t_0)\Psi(R,t_0), \tag{2.43}$$

where $\hat{U}(t - t_0)$ is the time evolution operator, which is defined as:

$$\hat{U}(t,t_0) = e^{-(i/\hbar)\hat{H}(t-t_0)}. \tag{2.44}$$

The basic operation (propagation) to solve the TDSE is to apply the Hamiltonian operator to the wavefunction ($\Psi(R,t_0)$) recursively, to generate a new wavefunction [46]. From Eq. 2.43 and 2.44, it can be readily seen that,

$$\Psi(R,t) = \hat{U}(t-t_0)\Psi(R,t_0) = \{1 - \left(\frac{i\hat{H}(t-t_0)}{\hbar}\right) - \frac{1}{2!}\left(\frac{\hat{H}(t-t_0)}{\hbar}\right)^2$$
$$+ \frac{i}{3!}\left(\frac{\hat{H}(t-t_0)}{\hbar}\right)^3 + ...\}\Psi(R,t_0). \tag{2.45}$$

In general, the initial state, $\Psi(R,t_0)$ is constructed from the wave packet and its evolution (the translational motion) is then interrogated to compute the desired information, such as reaction probability.

2.7.2 Representation of the wave function

An initial step to solve the TDSE is to expand the time dependent wavefunction in a proper basis set. This is normally carried out by expanding $\Psi(R,t_0)$ in a suitable basis set and then by evaluating the operator action on basis functions. One can use the collocation method, the discrete variable representation (DVR) [47, 48, 49, 50], the finite basis representation (FBR) [47, 48, 49, 50], FFT techniques, and a variational basis (or close coupling) representation. The computational efficiency of any time dependent wave packet (TDWP) method is strongly dependent on the representation of the basis sets.

A. Collocation method

Collocation refers to the numerical solution of a set of equations such that the result is exact at a discrete set of points [46]. Let $\Psi(r)$ be a given wave function which can be represented by an expansion of N linearly independent analytic basis function $(f_n(r))$ obeying the appropriate boundary conditions:

$$\Psi(r) = \sum_{n=1}^{N} C_n f_n(r). \tag{2.46}$$

Here, the coefficients, C_n are found by relating the wave functions at N points in r to the expansion and solving N linear equations by a matrix inversion, *viz.*,

$$\Psi(r_i) = \sum_{n=1}^{N} C_n f_n(r_i) \approx \mathbf{\Psi} = \mathbf{f}\mathbf{C}. \tag{2.47}$$

In Eq. 2.47, $\mathbf{f}$ is defined as an N dimensional square matrix which transforms the coefficients of the vector $\mathbf{C}$ into the wave function vector, $\mathbf{\Psi}$ (an approximation to Ψ). The inverse matrix, $\mathbf{f}^{-1}$ can be used to obtain the vector $\mathbf{C}$ from the vector $\mathbf{\Psi}$ by $\mathbf{C} = \mathbf{f}^{-1}\mathbf{\Psi}$. This demonstrates that the action of a non-local operator, $\hat{O}(r)$ on Ψ can be computed in a set of finite basis of f_n , using:

$$\hat{O}(r)\Psi(r) \approx \sum_{n=1}^{N} C_n \hat{O}(r) f_n(r) \approx \sum_{n=1}^{N} C_n f_n'(r). \tag{2.48}$$

B. FBR and DVR methods

The collocation method can be greatly simplified if the linearly independent basis functions $f_n(r)$ of Eq. 2.46, are chosen to be eigen functions of the operator, $\hat{O}(r)$ and are taken to be mutually orthogonal over the N discrete points at r_i. In other words, if we can write a relation of basis functions such as,

$$\sum_{k=1}^{N} f_n^*(\mathbf{r}_k) f_m(\mathbf{r}_k) = \delta_{n,m}, \tag{2.49}$$

the matrix $\mathbf{f}$ in Eq. 2.47 does not have to be inverted anymore and the following identity holds for Eq. 2.47:

$$\sum_{k=1}^{N} f_m^*(\mathbf{r}_k) \Psi(\mathbf{r}_k) = \sum_{n=1}^{N} \sum_{k=1}^{N} C_n f_n(\mathbf{r}_k) f_m^*(\mathbf{r}_k) = \sum_{n=1}^{N} C_n \delta_{n,m} = C_m. \tag{2.50}$$

Since f_n are the eigenfunctions of $\hat{O}$ Eq. 2.48 reduces to

$$\hat{O}(r)\Psi(r) \approx \sum_{n=1}^{N} C_n \hat{O}(r) f_n(r) \approx \sum_{n=1}^{N} C_n o_n f_n(r) \approx \sum_{n=1}^{N} C_n' f_n(r). \tag{2.51}$$

Here the operator $\hat{O}(r)$ is considered to be diagonal in the $\mathbf{C}$ representation. The action of $\hat{O}$ on Ψ can now be evaluated in three steps:

1. Transforming the DVR of Ψ ($\mathbf{\Psi}$) into the finite basis representation (FBR) of Ψ *i.e.* $\mathbf{C}$, by using $\mathbf{f}^{-1} = \mathbf{f}^{\dagger}$ because of Eq. 2.49.

2. Applying the operator $\hat{O}(r)$ on the FBR of $\Psi(r)$ to get $\mathbf{C'}$ - the FBR of $\hat{O}(r)\Psi(r)$. At this step the operator $\hat{O}(r)$ can be represented by a diagonal matrix *viz.*, $O_{mn} = \delta_{mn}o_n$ by virtue of the FBR.

3. Transforming $\mathbf{C'}$, the FBR of $\hat{O}(r)\Psi(r)$, back to the DVR of $\hat{O}(r)\Psi(r)$ *i.e.* $\mathbf{\Psi'}$, by using $\mathbf{f}$.

The DVR and FBR are considered to be conjugate to each other since the matrices $\mathbf{f}$ anf $\mathbf{f}^{-1}$ are used to transform between these representation of the wave function. Additionally, in the vector-matrix notation a complete procedure of applying $\hat{O}(r)$ on $\Psi(r)$ can now be expressed as:

$$\mathbf{\Psi'} = \mathbf{f}\mathbf{O}\mathbf{f}^{-1}\mathbf{\Psi} \tag{2.52}$$

This method of applying an operator to a grid based wave function is called the pseudo-spectral (PS) method. The DVRs are generally the time-independent bases and widely used in many wavepacket propagation calculations. By using a variety of basis functions, a number of different DVRs has been developed: the harmonic oscillator DVR used for vibrational motion, Legendre DVR for rotations, and exponential and sine DVRs used for free motion with or without periodic boundary conditions.

C. The Fourier representation

There are three properties of the plane wave functions that make the representation of a wave function much simpler. Firstly, they are eigenfunctions of the kinetic energy operator (*i.e.* $\nabla_r^2 e^{ik.r} = -k^2 e^{ik.r}$), secondly, they are mutually orthogonal to a series of N equally spaced grids $r_n = nL/N$ over the range of [0,L]:

$$\sum_{n=0}^{N-1} e^{\frac{-2\pi ip.r_n}{L}} e^{\frac{2\pi iq.r_n}{L}} = N\delta_{p,q}. \tag{2.53}$$

and thirdly, they form a complete set for periodic or bandwidth limited functions of r [51]. Note that Eq. 2.53 is exact and is resembles Eq. 2.49. Using Eq. 2.53 the discrete space conjugate to r_n is given by $k_m = \frac{2\pi m}{L}$ where $0 \leq m \leq N - 1$. In this representation the matrix elements of the matrix $\mathbf{f}$ in Eq. 2.47 , f_{mn} has a simple form: $f_{mn} = e^{2\pi imn/N}$. It immediatly follows that the FBR or the coefficients of the discretized wave function is given by $\mathbf{C} = \mathbf{f}^{-1}\mathbf{\Psi}$. These transforms based on plane wave basis are called Fourier transforms and in its advanced versions (FFT) the problem scales approximately as $Nlog_2N$ [52].

2.7.3   The MCTDH method

In general, the numerical effort of conventional wave packet propagation schemes increases exponentially with the number of degrees of freedom. The multi configuration time-dependent Hartree (MCTDH) method is an in-principle exact method and its ability lies in the fact that it uses a variational principle to derive equations

of motion [53, 54, 55]. This method uses optimized time-dependent one-particle basis functions and thus arrives at a compact representation of the state vector at the expense of more complicated equations of motion. The single-particle functions in MCTDH method are usually represented by standard DVR or FFT-schemes.

A. Wavefunction Ansatz and Equations of Motion

The solution of the TDSE (Eq. 2.42) is supposed to be distinct and and well-resolved in position. This immediately leads to a better approximation for the time dependent wavefunction: using linear combination of the single particle functions (SPFs). The MCTDH method uses the following wavefunction ansatz to solve the TDSE for a system with f degrees of freedom (DOFs) described by nuclear coordinates $Q_1, ..., Q_f$:

$$\psi \left(Q_1, \ldots Q_f, t \right) = \sum_{j_1=1}^{n_1} \cdots \sum_{j_f=1}^{n_f} A_{j_1 \ldots j_f} \left(t \right) \prod_{\kappa=1}^{f} \varphi_{j_\kappa}^{(\kappa)} \left(Q_\kappa, t \right). \tag{2.54}$$

Here, $A_{j_1}, \ldots, A_{j_f}$ are the MCTDH expansion coefficients and $\varphi \left(Q_\kappa, t \right)$ are the n_κ single particle functions associated with the degree of freedom κ. The Ansatz is similar to the standard wavepacket expansion, except that the SPFs provide a time-dependent basis set. In general, the SPFs are represented on a time-independent primitive basis set with N_κ points for the κ'th degrees of freedom, *viz.*,

$$\varphi_{j_\kappa}^{(\kappa)} \left(Q_\kappa, t \right) = \sum_{i_\kappa=1}^{N_\kappa} c_{i_\kappa, j_\kappa}^{(\kappa)} \left(t \right) \chi_{i_\kappa}^{(\kappa)} \left(Q_\kappa \right). \tag{2.55}$$

A DVR or Fourier representation is usually chosen to represent the basis function, $\chi_{i_\kappa}^{(\kappa)} \left(Q_\kappa \right)$. Using a technique called mode-combination, SPFs can be used to describe the motion in more than one degree of freedom [56].

To formulate the working equations of MCTDH one needs to introduce the single-hole functions. The single-hole functions $\Psi_l^{(\kappa)}$ are defined as the linear combination of Hartree products of $(f-1)$ SPFs that do not contain a SPF for the coordinate Q_κ

$$\Psi_l^{(\kappa)} = \sum_{J}^{\kappa} A_{J_l^\kappa} \varphi_{j_1}^{(1)} \ldots \varphi_{j_{\kappa-1}}^{(\kappa-1)} \varphi_{j_{\kappa+1}}^{(\kappa+1)} \ldots \varphi_{j_f}^{(f)}. \tag{2.56}$$

Here J_l^κ denotes a composite index J with the κ'th entry set at l, and $\sum_{J}^{\kappa}$ is the sum over the indices for all degrees of freedom excluding the κ'th. By defining the composite index J and the configurations $\Phi_J : A_J = A_{j_1 \ldots j_f}$ and $\Phi_J = \prod_{\kappa=1}^{f} \varphi_{j_\kappa}^{(\kappa)}$, the equations of motion can be derived using this ansatz in the Dirac–Frenkel variational method. The resulting coupled differential equations can be then written as:

$$i \dot{A}_J = \sum_{J} \left\langle \left. \Phi_J \right| H \left| \Phi_L \right\rangle A_L \tag{2.57}$$

$$i \dot{\varphi}_j^{(\kappa)} = \sum_{lm} \left(1 - P^{(\kappa)} \right) \left(\rho^{(\kappa)} \right)_{jl}^{-1} \langle H \rangle_{lm}^{(\kappa)} \varphi_m^{(\kappa)}, \tag{2.58}$$

where $P^{(\kappa)}$ denotes the projector on the space spanned by the SPF for the κ'th degree of freedom

$$P^{(\kappa)} = \sum_{j=1}^{n_\kappa} \left| \varphi_j^{(\kappa)} \right\rangle \left\langle \varphi_j^{(\kappa)} \right|, \tag{2.59}$$

and $\langle H \rangle^{(\kappa)}$ and $\rho^{(\kappa)}$ are, respectively, the mean-fields and density matrices that can be obtained from the single-hole functions :

$$\langle H \rangle_{jl}^{(\kappa)} = \left\langle \Psi_j^{(\kappa)} \right| H \left| \Psi_l^{(\kappa)} \right\rangle \tag{2.60}$$

$$\rho_{jl}^{(\kappa)} = \left\langle \Psi_j^{(\kappa)} \middle| \Psi_l^{(\kappa)} \right\rangle = \sum_J^\kappa A_{J_j^\kappa}^* A_{J_l^\kappa}. \tag{2.61}$$

The populations of the natural orbitals, which are defined as the eigenvalues of the density operator in each degree of freedom (Eq. 2.61), reflect the degree of convergence of the wave function with respect to the size of the time-dependent basis set. In particular, a small value of the lowest natural population indicates that enough SPFs have been used for the single particle to achieve convergence. Eqs. 2.57 and 2.58 are the MCTDH equations of motion for the simplest choice of constraints.

B. Refitting the PES

To integrate the equations of motion of MCTDH the evaluation of the Hamiltonian matrix, $\langle \Phi_J | H | \Phi_L \rangle$ and the mean-fields, $\langle H \rangle$ at each time step of the integration is necessary. These f and $(f-1)$ dimensional integrals are circumvented if the Hamiltonian is written as a sum of products of single-particle operators :

$$H = \sum_{r=1}^{s} c_r \prod_{\kappa=1}^{f} h_r^{(\kappa)} \tag{2.62}$$

with expansion coefficients c_r. The KEO usually has the product form of Eq. 2.62, but (in general) the potential energy term does not have this form. To cope with this issue, MCTDH uses the 'potfit' algorithm [57, 58] based on the approximation theorem by Schmidt.

If the PES is given on a product grid, $V\left(Q_{i_1}^{(1)}, \ldots, Q_{i_f}^{(f)}\right) \equiv V_{i_1 \ldots i_f}$, then the elements of the symmetric positive semi-definite potential density matrices $\varrho^{(\kappa)}$ can be written as

$$\varrho_{jl}^{(\kappa)} = \sum_{i_1=1}^{N_1} \cdots \sum_{i_{\kappa-1}=1}^{N_{\kappa-1}} \sum_{i_{\kappa+1}=1}^{N_{\kappa+1}} \cdots \sum_{i_f=1}^{N_f} V_{i_1 \ldots i_{\kappa-1} j i_{\kappa+1} \ldots i_f} V_{i_1 \ldots i_{\kappa-1} l i_{\kappa+1} \ldots i_f}. \tag{2.63}$$

The orthonormal eigenvectors $v_j^{(\kappa)}$ and the associated eigenvalues $\lambda_j^{(\kappa)}$ of these matrices are called natural potentials and natural potential populations, respectively. The potential now can be approximated by using a set of expansion order, $\{m_\kappa\}$

$$V^{app}\left(Q_{i_1}^{(1)},\ldots,Q_{i_f}^{(f)}\right) \approx \sum_{j_1=1}^{m_1}\cdots\sum_{j_f=1}^{m_f} C_{j_1\ldots j_f} v_{j_1}^{(1)}\left(Q_{i_1}^{(1)}\right)\ldots v_{j_f}^{(f)}\left(Q_{i_f}^{(f)}\right). \qquad (2.64)$$

The expansion coefficients $C_{j_1\ldots j_f}$ are determined by the overlaps between the potential and the natural potentials,

$$C_{j_1\ldots j_f} = \sum_{i_1=1}^{N_1}\cdots\sum_{i_f=1}^{N_f} V_{i_1\ldots i_f} v_{i_1 j_1}^{(1)}\ldots v_{i_f j_f}^{(f)} \qquad (2.65)$$

If the expansion orders and the number of grid points are equal, the fitted and the exact potential are identical ($V^{app} \to V$ for $\{m_\kappa\} \to \{N_\kappa\}$), at the grid point.

C. Flux Analysis

The MCTDH method uses the complex absorbing potential(CAP)/flux method for analysing reactive scattering events [59, 60]. The CAP is an artificial negative imaginary potential located in the product channel. At the end of the DVR grid the CAP absorbs the dissociated part of the wavefunction to avoid unphysical reflections from the end of the grid. The MCTDH package comprises monomial CAPs

$$-iW\left(Q\right) = -i\eta\left(Q - Q_c\right)^b \Theta\left(Q - Q_c\right) \qquad (2.66)$$

where η, b and Q_c denote the strength, the order and the starting point of the CAP, respectively. $\Theta\left(Q - Q_c\right)$is the Heaviside step function, allowing to switch on the CAP when $Q > Q_c$($\Theta = 0$ when $Q \leqslant Q_c$ and $\Theta = 1$ for $Q > Q_c$).

By using the CAP/flux formalism, the reaction probability $P_i\left(E_{Z_i}\right)$ can be defined as:

$$P_i\left(E_{Z_i}\right) = \frac{2}{\pi\left|\Delta E_{Z_i}\right|^2}\mathrm{Re}\left\{\int_0^\infty d\tau g\left(\tau\right)\exp\left(iE_{Z_i}\right)\right\} \qquad (2.67)$$

where ΔE_{Z_i} denotes the energy distribution of the initial wave packet for translation normal to the surface. The value of ΔE_{Z_i} determines the energy range for which the reaction probability can be computed in one single calculation. The working equations relate the time evolution of the initial wave packet, via the dissociation arrangement channel CAP, W_r, to the desired initial-state selected reaction probabilities.

Bibliography

[1] M. Born and E. Oppenheimer, Ann. Phys. **84**, 457 (1927).

[2] P. Hohenberg and W. Kohn, Phys. Rev. B **136**, 864 (1964).

[3] W. Kohn and L. J. Sham, Phys. Rev. A **140**, 1133 (1965).

[4] W. Koch and M. C. Holthausen, *A Chemist's Guide to Density Functional Theory* (Wiley-VCH, Weinheim, 2002).

[5] J. P. Perdew, J. A. Chevary, S. H. Vosko, K. A. Jackson, M. R. Pederson, D. J. Singh, and C. Fiolhais, Phys. Rev. B **46**, 6671 (1992).

[6] J. P. Perdew, *Electronic Structure of Solids* (Akademie Verlag, Berlin, 1991).

[7] B. Hammer, L. B. Hansen, and J. K. Nørskov, Phys. Rev. B **59**, 7413 (1999).

[8] D. J. Chadi and M. L. Cohen, Phys. Rev. B **8**, 5747 (1973).

[9] H. J. Monkhorst and J. D. Pack, Phys. Rev. B **13**, 5188 (1976).

[10] P. E. Blöchl, Phys. Rev. B **41**, 5414 (1990).

[11] D. Vanderbilt, Phys. Rev. B **41**, 7892 (1990).

[12] S. R. Bahn and K. W. Jacobsen, Comput. Sci. Eng. **4**, 56 (2002), the DA-CAPO code is freely available at, http://www.camp.dtu.dk/software.

[13] G. Kresse and J. Hafner, Phys. Rev. B **47**, 558 (1993).

[14] G. Kresse and J. Hafner, Phys. Rev. B **49**, 14251 (1994).

[15] G. Kresse and J. Furthmüller, Comput. Mat. Sci. **6**, 15 (1996).

[16] G. Kresse and J. Furthmüller, Phys. Rev. B **54**, 11169 (1996).

[17] P. E. Blöchl, Phys. Rev. B **50**, 17953 (1994).

[18] G. Kresse and D. Joubert, Phys. Rev. B **59**, 1758 (1999).

[19] C. Herring, Phys. Rev. **57**, 1169 (1940).

[20] D. J. Wales, *Energy landscapes* (Cambridge University Press, Cambridge, 2003).

[21] G. Mills and H. Jónsson, Phys. Rev. Lett. **72**, 1124 (1994).

[22] G. Mills, H. Jónsson, and G. K. Schenter, Surf. Sci. **324**, 305 (1995).

[23] H. Jónsson, G. Mills, and K. W. Jacobsen, *Classical and Quantum Dynamics in Condensed Phase Simulations* (World Scientific, Singapore, 1998).

[24] G. Henkelman, B. P. Uberuaga, and H. Jónsson, J. Chem. Phys. **113**, 9901 (2000).

[25] P. Maragakis, S. A. Andreev, Y. Brumer, D. R. Reichman, and E. Kaxiras, J. Chem. Phys. **117**, 4651 (2002).

[26] M. A. Bhatti, *Practical Optimization Methods* (Springer-Verlag, New York, 2000).

[27] W. Press, S. Teukolsky, W. Vetterling, and B. Flannery, *Numerical Recipes in C* (Cambridge University Press, Cambridge, 1992).

[28] D. A. McQuarrie, *Quantum Chemistry* (University Science Books, New Delhi, 2007), 2nd edition.

[29] G. Herzberg, *Infra-Red and Raman Spectra of Polyatomic Molecules* (D. Van Nostrand Company, New York, 1945).

[30] M. J. T. Jordan, K. C. Thompson, and M. A. Collins, J. Chem. Phys. **102**, 5647 (1995).

[31] K. C. Thompson, M. J. T. Jordan, and M. A. Collins, J. Chem. Phys. **108**, 8302 (1998).

[32] R. P. A. Bettens and M. A. Collins, J. Chem. Phys. **111**, 816 (1999).

[33] Y. Zhao and D. G. Truhlar, J. Chem. Phys. **128**, 184109 (2008).

[34] C. Crespos, M. A. Collins, E. Pijper, and G. J. Kroes, J. Chem. Phys. **120**, 2392 (2004).

[35] H. F. Busnengo, A. Salin, and W. Dong, J. Chem. Phys. **112**, 7641 (2000).

[36] R. A. Olsen, H. F. Busnengo, A. Salin, M. F. Somers, G. J. Kroes, and E. J. Baerends, J. Chem. Phys. **116**, 3841 (2002).

[37] W. C. Swope, H. C. Andersen, P. H. Berens, and K. R. Wilson, J. Chem. Phys. **76**, 637 (1982).

[38] M. Karplus, R. N. Porter, and R. D. Sharma, J. Chem. Phys. **43**, 3259 (1965).

[39] Y. Guo, D. L. Thompson, and T. D. Sewell, J. Chem. Phys. **104**, 576 (1996).

[40] D. A. McCormack and G. J. Kroes, Phys. Chem. Chem. Phys. **1**, 1359 (1999).

[41] D. A. McCormack, G. J. Kroes, R. A. Olsen, I. A. Groeneveld, J. N. P. van Stralen, E. J. Baerends, and R. C. Mowrey, Faraday Discuss. **117**, 109 (2000).

[42] E. Pijper, M. F. Somers, G. J. Kroes, R. A. Olsen, E. J. Baerends, H. F. Busnengo, A. Salin, and D. Lemoine, Chem. Phys. Lett. **347**, 277 (2001).

[43] P. Rivière, H. F. Busnengo, and F. Martín, J. Chem. Phys. **123**, 074705 (2005).

[44] G. J. Kroes and M. F. Somers, J. Theor. Comput. Chem. **4**, 493 (2005).

[45] H. F. Busnengo, C. Crespos, W. Dong, J. C. Rayez, and A. Salin, J. Chem. Phys. **116**, 9005 (2002).

[46] R. Kosloff, J. Phys. Chem **92**, 2087 (1988).

[47] A. S. Dickinson and P. R. Certain, J. Chem. Phys. **49**, 4209 (1968).

[48] I. P. Hamilton and J. C. Light, J. Chem. Phys. **84**, 306 (1986).

[49] J. V. Lill, G. A. Parker, and J. C. Light, Chem. Phys. Lett. **89**, 483 (1982).

[50] G. C. Corey, J. W. Tromp, and D. Lemoine, *Numerical grid methods and their applications to the Schrödinger equation* (Kluwer Academic, Dordrecht, 1993).

[51] G. B. Arfken and H. J. Weber, *Mathematical methods for physicists* (Academic Press, San Diego, 1995).

[52] A. Besprozvannaya and D. J. Tannor, Comput. Phys. Commun. **63**, 569 (1991).

[53] H.-D. Meyer, U. Manthe, and L. Cederbaum, Chem. Phys. Lett. **165**, 73 (1990).

[54] M. H. Beck, A. Jäckle, G. A. Worth, and H.-D. Meyer, Phys. Rep. **324**, 1 (2000).

[55] H.-D. Meyer, F. Gatti, and G. A. Worth, *Multidimensional Quantum Dynamics: MCTDH theory and applications* (Wiley-VCH, Weinheim, 2009).

[56] A. Raab, G. A. Worth, H.-D. Meyer, and L. S. Cederbaum, J. Chem. Phys. **110**, 936 (1999).

[57] A. Jäckle and H.-D. Meyer, J. Chem. Phys. **109**, 3772 (1998).

[58] A. Jäckle and H.-D. Meyer, J. Chem. Phys. **104**, 7974 (1996).

[59] D. Neuhasuer and M. Baer, J. Chem. Phys. **90**, 4351 (1989).

[60] U. V. Riss and H.-D. Meyer, J. Phys. B **26**, 4503 (1993).

Chapter 3

Towards an understanding of the vibrational mode specificity for dissociative chemisorption of CH$_4$ on Ni(111): A 15 dimensional study

Abstract

We present a fifteen-dimensional (15D) vibrational mode following calculation along the minimum energy path (MEP) of the dissociative chemisorption of CH$_4$ on Ni(111), based on density functional theory (DFT). The MEP has been obtained from the (climbing image) nudged elastic band and steepest descent methods employing a periodic DFT code. The MEP displays a late barrier of 1.09 eV, which is reduced to 0.95 eV after zero-point energy corrections, and a considerable CH bond elongation at the transition state, in accordance with earlier calculations. Our vibrational calculations within the harmonic approximation show a significant involvement of the different vibrational coordinates in reaching the transition state. The couplings between the normal modes have been analyzed along the MEP, various crossing and avoided crossing regions have been identified and discussed in connection with the corresponding Massey velocities and parameters. Based on our analysis we find that pre-exciting the symmetric stretch vibration should be approximately 3 times as efficient in promoting reaction as pre-exciting the asymmetric stretch vibration. The analysis also suggests that the bend vibrations do not couple well to the reaction coordinate, whereas the stretches are efficiently coupled to the reaction coordinate. Both results are in good agreement with experiments.

3.1   Introduction

The current commercial scheme to produce hydrogen is steam reforming of hydrocarbons using nickel as catalyst, in which methane is the major feedstock [1, 2]. To enhance the yield of this reaction, a detailed understanding of the rate-limiting step is necessary.

Molecular beam experiments indicate that putting energy into vibrational and translational motion is efficient in promoting dissociation of methane [3, 4], whereas rotational excitation only makes a minor contribution to increased reactivity [5]. State-resolved sticking coefficient measurements by Juurlink *et al.* for CH_4 on the Ni(100) surface showed that pre-excitation of the asymmetric stretch vibration, ν_3, enhances the reaction, even though the equivalent amount of translational energy is more effective in increasing the reactivity [6]. In contrast, a strong preference for the excitation of ν_3 over translational energy activation was found from the reaction probability measurements by Utz and co. on the Ni(111) surface [7]. The second overtone of the triply degenerate bending state, $3\nu_4$, was found to be less effective in promoting reaction than the ν_3 excitation even though $3\nu_4$ contains more energy [8]. The mode specific reactivity study by Beck *et al.* showed that the reactivity of CD_2H_2 excited with two quanta of vibrational energy in one CH bond is much greater than that of the molecule excited with one quantum in each of two CH bonds on the Ni (100) surface [9, 10]. On Ni(100), the reactivity of CH_4 pre-excited with one quantum of the symmetric stretch mode, ν_1, is about an order of magnitude higher than that of CH_4 pre-excited with one quantum of the asymmetric stretch mode, ν_3, and it is similar to the reactivity of CH_4 in the $2\nu_3$, state [11, 12]. Although the (100) surface of Ni is more reactive than (111) surface towards CH_4, the trends regarding the effect of vibrational pre-excitation on reaction are similar. For instance, Juurlink *et al.*, found the $1\nu_3$ stretch excited state of CH_4 to be more reactive than the $3\nu_4$ bend excited state, on both Ni(111) and Ni(100)[8].

Much theoretical work has been done, both using density functional theory (DFT) and ab initio theories, to describe the minimum energy path (MEP) and the transition state of methane dissociation on Ni surfaces. Using a cluster model and treating the electron correlation at the configuration interaction level, Yang and Whitten reported a barrier of 0.74 eV [13]. Kratzer *et al.* [14], using a plane wave DFT approach employing the PW91 functional [15, 16], found that the cleavage of the CH bond occurred preferentially atop of a Ni surface atom, with the reactive CH bond oriented towards the adjacent hollow site, and a barrier height to dissociation of 1.12 eV. Burghgraef *et al.* [17] predicted an important role for the CH stretch in the dissociation, a loose transition state, and a barrier of 1.04 eV using a cluster approach within DFT using the gradient corrected B88 functional for exchange [18] in combination with the Stoll correction for correlation[19, 20]. Abild-Pedersen *et al.* [21] reported a barrier of 1.09 eV using the nudged elastic band (NEB) method together with periodic DFT using the RPBE functional [22], also taking the spin-polarization of the electrons into account. Watwe *et al.* [23] found an activation energy of 1.32 eV using the same approach as Abild-Pedersen *et al.*, but without considering spin-polarization. Henkelman *et al.*, as well as Nave *et al.*, performed periodic DFT calculations showing the importance of the lattice

reconstruction and the puckering of the nickel atom for the reactivity [24, 25, 26]. The effect of tunnelling, particularly at low incident energies, and the effect of the mass of the surface atoms on the surface reconstruction have also been studied [27].

A 'quasidiatomic' quantum-dynamics model proposed by Luntz and Harris illustrated the effect of the incident translational and initial vibrational energies of methane on the reactivity [28]. The statistical model by Harrisson, based on microcanonical unimolecular rate theory [29], predicted sticking probabilities and threshold energy for the CH bond by considering the vibrational excitation [30, 31]. The wave packet calculations by Milot including all nine internal vibrations, predicted that the symmetric stretch is more effective than the asymmetric stretch and bend modes at promoting reaction [32].

A local mode description by Halonen et al. using a spectroscopically fitted London-Eyring-Polanyi-Sato potential, pointed out the importance of the ν_1 mode as the CH_4 molecule approaches the surface, both in its fundamental and overtone states [33]. Although their work was based on a four-dimensional quantum vibrational calculation which only considers the CH stretch manifolds, the model predicts the splitting of degenerate levels, avoided crossings, the effectiveness of symmetric over anti-symmetric stretches and the subsequent localization of the vibrational energy into the reactive CH bond. The nature of avoided curve crossing was qualitatively examined using a Landau–Zener semiclassical treatment, and the result showed that these crossings are not purely diabatic or adiabatic. Another important observation was the 'quarantaining' of the vibrational energy in the CH_3 group in the case of asymmetric excitation of ν_3 mode, making CH_3 behave as a spectator group.

In the present work a vibrational analysis within the harmonic approximation is performed along the MEP of the CH_4/Ni(111) system employing DFT using the PW91 functional, with the goal being to understand better the differences between the methane vibrational modes in promoting reaction. Our work aims to improve upon the pioneering work of Halonen *et al.* by considering the effect of all fifteen molecular degrees of freedom of methane interacting with the Ni(111) surface instead of only the four CH-stretches and the motion towards the surface. The methods used are described in Section 3.2. In Section 3.3 the results are presented and discussed before we conclude in Section 3.4.

3.2 Methods

3.2.1 Electronic structure method

The electronic structure calculations have been performed using spin-polarized DFT [34, 35]as implemented in the Vienna ab initio simulation program (VASP) [36, 37, 38, 39]. Projector augmented wave (PAW) pseudopotentials were used to represent the electron - ion-core interactions and the Kohn-Sham wavefunctions were expanded in a plane wave basis set [40, 41]. In all calculations the PW91 functional [15, 16] , together with the Vosko-Wilk-Nusair representation of the local density approximation [42] , was chosen to describe the exchange-correlation interaction at the generalized gradient approximation (GGA) level.

plane wave cut–off (eV)	E_{chem} (eV)
300	1.0696
350	1.0894
400	1.0918
450	1.0916
500	1.0917
550	1.0923
600	1.0914

Table 3.1: Convergence of the chemisorption energy (see Eq. 3.1) at a (fixed) transition state geometry with respect to the plane wave cut-off. All calculations were done using a three layer nickel slab and a 2×2 unit cell. The plane wave cut-off tests were done using a grid of 9×9×1 k-points.

k-point grid	E_{chem} (eV)
3×3×1	1.0544
5×5×1	1.0999
7×7×1	1.0798
9×9×1	1.0918
11×11×1	1.0972
13×13×1	1.0961

Table 3.2: Convergence of the chemisorption energy (see Eq. 3.1) at a (fixed) transition state geometry with respect to the k-point sampling of the system. All calculations were done using a three layer nickel slab and a 2×2 unit cell. The k-point tests were done using a plane wave cut-off of 400 eV.

The bulk lattice constant of fcc Ni was found to be 3.52 Å by minimization of the total energy with respect to the bulk lattice constant, in good agreement with the experimental value of 3.52 Å. A 15×15×15 Monkhorst-Pack k-point grid and a plane wave cut-off of 600 eV were used in these calculations.

Interlayer relaxations were carried out for a Ni slab with an exposed (111) surface. Using a 2×2 unit cell and a three layer slab we obtained a relaxed value of 2.005 Å for the interlayer separation. This value is smaller by 1.34% relative to the experimental bulk interlayer distance of 2.03 Å. A vacuum distance of 16 Å was found to give converged results for this slab, as confirmed by a calculations using vacuum distances up to 21 Å.

The chemisorption energy of a CH_4 molecule absorbed on Ni(111) is calculated as

$$E_{chem} = E_{CH4+Ni(111)} - E_{CH4(g)+Ni(111)}. \qquad (3.1)$$

Here, $E_{CH4+Ni(111)}$ is the total energy of the Ni(111) slab with the CH_4 molecule adsorbed and $E_{CH4(g)+Ni(111)}$ is the energy with CH_4 in its equilibrium gas phase

geometry 5 Å above the Ni(111) slab. The system was modelled using a frozen three layer nickel slab (see above) and a 2×2 unit cell, with a supercell size of 20 Å in the direction perpendicular to the slab (a vacuum distance of 16 Å). A three layer slab was chosen as a compromise between computational efficiency and accuracy: DFT calculations carried out with another plane wave code [22, 43]showed that a three layer slab yields reasonably well converged chemisorption energies. The k-point and plane wave sampling were done by converging the total energy to within 1 meV with respect to the associated parameters. A plane wave cut-off of 450 eV (Table 3.1) and a Gamma centered grid of 11×11×1 k-points were needed (Table 3.2). In all slab calculations, the projection operators were evaluated in reciprocal space with an additional grid for the augmentation charges and avoiding wrap-around errors with tight numerical convergence.
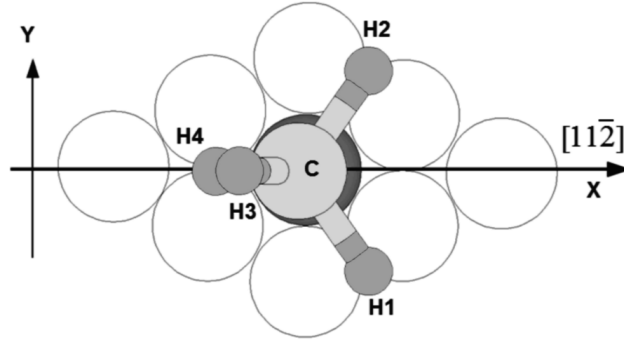

Figure 3.1: The C_S symmetry plane associated with methane dissociating on the Ni(111) surface along the MEP. This plane passes through the C, H3 and H4 atoms and the atop nickel atom (dark circle) and is along the [11$\bar{2}$] incidence direction. The H4 atom is closer to the surface than the H3 atom.

3.2.2 Minimum energy path

The MEP was obtained in mass un-weighted coordinates primarily by using a climbing image nudged elastic band method (CI-NEB) [44, 45, 46]with eleven intermediate images. We used a CI-NEB module [47] in conjunction with VASP for the CI-NEB calculations. The Cartesian force components of the initial and final structures were minimized to less than 10-5 eV/Å for each atom. The minimization of the band was done by a quasi-Newton method until the maximum force acting on any atom was smaller than 0.01 eV/Å. The transition state was verified by a frequency calculation which gave a single imaginary frequency, where we used finite differencing of energies to get accurate Hessian matrix elements. Then a dense MEP was obtained partly by NEB calculations between the CI-NEB obtained configurations and partly by a steepest descent (SD) procedure starting

from the transition state. The computationally expensive NEB method was used only near the flat-potential region where the noise in the DFT force is large relative to the force along the reaction coordinate, so that the SD method becomes numerically unstable. The precise direction of the descent towards the reactants was determined from the imaginary mode eigenvector at the transition state. A step length of 0.1 Å was used in the first step and a length of 0.01 Å was used in the consecutive steps. In all calculations a frozen nickel slab was used (see Section 3.2.1). The motion of methane was always restricted to a plane along the $[11\bar{2}]$ incidence direction that intersects surface nickel atoms (see Fig. 3.1). C_S symmetry with respect to this plane was enforced for the whole system in the NEB and SD calculations, in accordance with the CI-NEB results for which this restriction was not enforced. In the calculations of the MEP, the electronic occupancies were determined according to a tetrahedron method with Blöchl corrections with an energy smearing of 0.1 eV [48], to get accurate energies.

We defined a mass dependent reaction coordinate, ρ_n, as

$$\rho_n = \sum_{l=1}^{15} d\rho_i = \sum_{i=1}^{n} \sqrt{\sum_{l=1}^{15} dx_{l_i}^2} \,, \tag{3.2}$$

where ρ_n is the reaction coordinate of the n'th configuration in the MEP and $d\rho_i$ is the distance in the mass-weighted Cartesian coordinates between the $(i-1)$'th and i'th configuration on the reaction path. The x_{l_i} is any of the l=1-15 mass-weighted Cartesian atomic coordinates of methane.
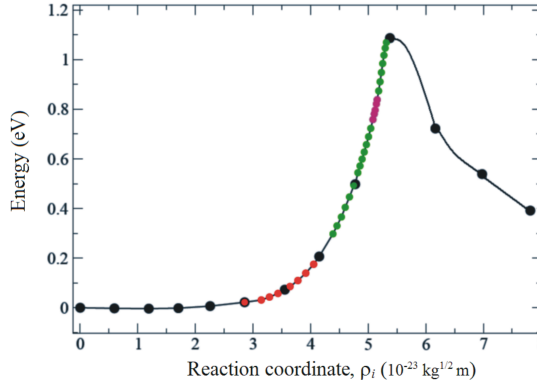
Figure 3.2: The potential energy along the MEP is shown for CH$_4$+Ni(111), as obtained from the CI-NEB, NEB and steepest descent calculations. The CI-NEB points (black), NEB points (red) and steepest descent points (green, violet) are shown together with the early crossing (red) and the late crossing (violet) regions.

3.2.3   Vibrational analysis

To obtain the vibrational eigenvalues and eigenvectors along the MEP within the harmonic approximation, the Hessian matrix elements were calculated by finite

differencing of the gradients using a standard two point central difference formula. A Cartesian displacement of 0.001 Å was used everywhere except in the region we call the early crossing region (ECR, see Section 3.3 below) where a value of 0.02 Å was used. A larger displacement was chosen in the ECR to diminish the numerical noise. To obtain accurate eigenvalues of degenerate vibrational states, a Fermi smearing of a width of 0.1 eV was applied to the electronic occupancies near the Fermi level. The major challenge we faced in this project was the numerical noise in the Hessian matrix elements, due to inaccuracies in the DFT gradients. To solve this problem, the Hessian matrices along the MEP were recalculated by fitting the gradients as a function of the reaction coordinate (Eq. 3.2). A nonlinear least-square method of Levenberg-Marquardt [49] was used to fit the force components against a collection of 13 transcendental and/or algebraic model functions and in each case we chose the model function that provided the best fit. Next, at each point along the MEP the Hessian matrix was mass weighted and C_S symmetry was imposed (see Section 3.2.2). The normal modes were obtained by diagonalizing this symmetrized Hessian matrix. A detailed description of the procedure used is provided in the supplementary information.

3.2.4 Massey model for vibrational coupling

The Massey velocities (v_m) [33, 50] and parameters (M_p) were calculated along the MEP to determine the nature of the vibrational couplings (adiabatic or diabatic) between modes along the MEP. These quantities are defined as

$$v_m = \frac{|E_a^i - E_b^i|}{|\hbar \langle {}^a\psi_i | \frac{\partial}{\partial \rho} | {}^b\psi_i \rangle|}, \tag{3.3}$$

and

$$M_p = \frac{v_m}{v_\rho}. \tag{3.4}$$

Here, E_a^i and E_b^i are the a'th and b'th vibrational eigenvalues ($a, b \in [0, \infty]$) at the i'th point along the reaction coordinate, ${}^a\psi_i$ and ${}^b\psi_i$ the corresponding vibrational wavefunctions, and v_ρ is the velocity of methane along the MEP at the selected point (see Section 3.2.5).

   In our approach, we make two approximations to calculate the Massey velocity in Eq. (3.3), and we restrict ourselves to evaluating couplings between specific vibrational states. The first approximation is to use finite differencing to calculate the dot-product in the denominator:

$$\langle {}^a\psi_i | \frac{\partial}{\partial \rho} | {}^b\psi_i \rangle \approx \langle {}^a\psi_i | \left[\frac{|{}^b\psi_{i+1}\rangle - |{}^b\psi_{i-1}\rangle}{\rho_{i+1} - \rho_{i-1}} \right] = \frac{\langle {}^a\psi_i | {}^b\psi_{i+1} \rangle - \langle {}^a\psi_i | {}^b\psi_{i-1} \rangle}{\rho_{i+1} - \rho_{i-1}}. \tag{3.5}$$

By choosing a dense enough grid in combination with the fitting procedure described in Section 3.2.3, we have made sure the error made is negligible. In order to make the second approximation, we restrict ourselves to couplings between states in which only one vibrational mode is excited with one quantum (fundamentals).

Assuming that these states may be well described within the normal mode approximation and that the difference between the CH_4 geometries $(i-1)$ and $(i+1)$ is small, we may replace the dot-product of the vibrational wave functions with the corresponding dot-product of the Cartesian normal mode eigenvectors, ${}^a\chi_i$. A corollary of the above assumption is that in the crossing region and for these small geometry differences, basis functions describing other normal modes do not change their overlap with their neighbouring equivalent basis functions, and that these overlaps are 1. The assumed equivalence between the overlap integral and the dot product can be written as

$$\langle {}^a\psi_i | {}^b\psi_{i+1} \rangle \approx \langle {}^a\chi_i | {}^b\chi_{i+1} \rangle, \langle {}^a\psi_i | {}^b\psi_{i-1} \rangle \approx \langle {}^a\chi_i | {}^b\chi_{i-1} \rangle, \tag{3.6}$$

(See the supplementary document for further justification based on the '$\hbar$-deformation' [51] of the classical eigenvectors to their quantum counterparts). This represents a reasonable approximation for the overlap between the fundamental vibrational modes $(a, b \in [0, 14])$, and therefore the Massey velocities are calculated according to (substituting Eqs. 3.5 and 3.6 into Eq. 3.3):

$$\frac{|E_a^i - E_b^i|}{\hbar \left[\frac{\langle {}^a\chi_i | {}^b\chi_{i+1} \rangle - \langle {}^a\chi_i | {}^b\chi_{i-1} \rangle}{\rho_{i+1} - \rho_{i-1}} \right]}. \tag{3.7}$$

3.2.5   Velocities along the reaction coordinate

To obtain Massey parameters (Eq. 3.4) the velocities along the reaction coordinate of the methane, v_ρ , at the relevant configurations must be known. From the geometries at the ECR it can be seen that the motion of CH_4 is mainly along the surface normal. Nearer to the transition state (in what we call the late crossing region (LCR)) it is more complicated, and it involves rotations as well as translations. The velocity along the reaction coordinate needs to be calculated by using the definition of the reaction coordinate given in Section 3.2.2. The kinetic energy along the reaction coordinate at the crossing regions can be written as

$$T_\rho = \frac{1}{2} V_\rho^2, \tag{3.8}$$

where, V_ρ is the mass-weighted velocity of the system along the reaction coordinate. From Eq. 3.8 the velocity along the reaction path can be estimated using the kinetic energy calculated from

$$T_\rho = T_i + \triangle E_{vib} - \triangle V_{LCR}, \tag{3.9}$$

where T_i is the initial kinetic energy, $\triangle E_{vib}$ the vibrational energy change and $\triangle V_{LCR}$ the potential energy change from the initial configuration.

3.3   Results and discussion

3.3.1   The minimum energy path

First we obtained a converged CI-NEB path from an initial state where CH_4 is in the gas phase (i.e., 5 Å above the surface) and a final state where the dissociated

fragments of hydrogen and methyl are adsorbed in the hcp and fcc hollow sites, respectively. A late barrier was obtained, with a height of 1.09 eV (Fig. 3.2 and Table 3.3). This late barrier points to the importance of the vibrational excitation in this system according to Polanyi rules [52], which states that the later the barrier is the more effective the excitation of vibrational motion is for promoting reaction compared to increasing the collision energy. The geometry of the transition state (TS) and the barrier height were found to be consistent with previous DFT results using the PW91 functional. The comparison is particularly good for the plane wave periodic DFT results of Kratzer *et al.* [14] and Nave and Jackson [25], the agreement being less good for the *ab initio* embedded cluster-calculation results of Yang and Whitten [13] (Table 3.3).

	this work	Ref. 20	Ref. 14	Ref. 13
Angles (degrees)				
H3-C-H4	80			
C-Ni$_\text{atop}$ - fcc$_\text{hollow}$	91			
H4-C-Ni	48			
H1-C-H2	112			
θ	133	133	125	125
Distances (Å)				
C-H1, C-H2	1.10			
C-H3	1.10			
C-H4	1.59	1.61	1.59	1.53
Ni$_\text{atop}$-C	2.13			
Ni$_\text{atop}$-H4	1.59			
Z_C	2.13	2.07	2.13	2.33
Z_{H4}	1.04			
Barrier height (eV)	1.09	1.09	1.12	0.72

Table 3.3: Selected angles, distances and the barrier of the TS obtained by different studies. H4 is the reacting hydrogen atom, θ is the polar angle (H4-C-surface normal) and Ni_atop is the Ni atom above which the methane molecule dissociates. The barrier height is given without zero-point energy corrections. See also Figs. 3.1, 3.3, 3.4, and 3.5.

From Table 3.3 and Figs. 3.3 and 3.4 it is seen that the TS geometry displays a considerable CH bond elongation (a large C-H4 distance). In the TS geometry, the H atom resulting from the dissociation of CH4 is already close to the hcp hollow site atomic chemisorption minimum geometry. The C atom is however still located above the atop Ni atom. Only after the TS has been passed does the methyl fragment move over to the fcc-hollow site chemisorption minimum geometry of CH$_3$. As noted before, the CH$_4$+Ni(111) system displays C_S symmetry along the MEP with respect to a plane passing through the atop Ni atom above which CH$_4$ dissociates and lying parallel to the [11$\bar{2}$] incidence direction (Fig. 3.1). Although we did not explicitly impose any geometrical constraints in the

CI-NEB calculations, the motion of methane was always such that C_S symmetry was preserved.
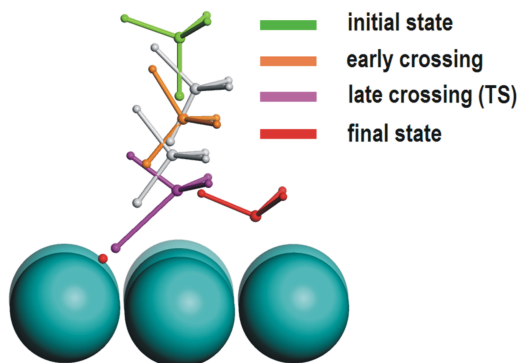

Figure 3.3: Selected geometries from the converged CI-NEB calculation along the MEP. The approximate geometries corresponding to the two crossing regions are also indicated.
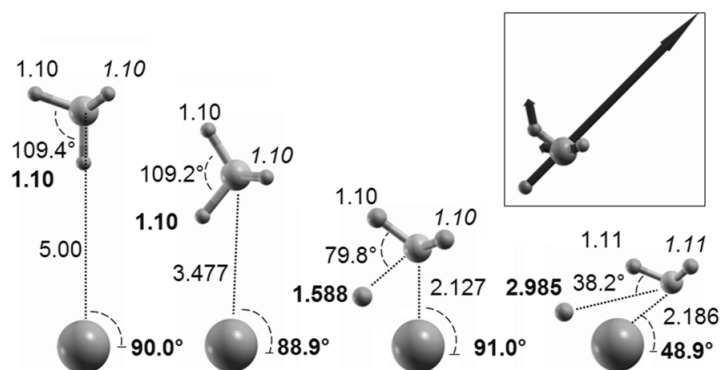
Figure 3.4: The initial (a), early crossing (b), TS (c) and final state (d) geometries relative to atop nickel atom. The inset shows the imaginary mode of the TS where all the vectors are elongated for clarity. The longest vector is along the dissociating CH bond.

3.3.2   Vibrational analysis

To obtain a sufficiently dense set of configurations for an accurate vibrational analysis, the MEP was obtained partly by NEB calculations between the CI-NEB obtained configurations and partly by a SD procedure starting from the transition state using mass un-weighted coordinates. The equivalence of the MEP in mass weighted and mass un-weighted coordinates system has been established elsewhere

[53]. The imaginary mode of the TS (see inset in Fig. 3.4) was used in the first step of the SD procedure. A large step length (0.1 Å) was needed in the first step to move away from the 'flat' region near the TS. As seen from Fig. 3.2, the part of the MEP obtained with the SD procedure smoothly connects points obtained with the CI-NEB procedure, as does the part obtained from the NEB calculations.

Label	Initial	Early crossing	Late crossing	TS	Final (CH$_3$)
ν_3,A"	3096	3087	3107	3066	2951
ν_3,A'	3085	3084	3095	3048	2950
ν_3,A'	3083	3043	2990	2953	2890
ν_1,A'	2978	2947	1829	1556	1341
ν_2,A'	1514	1510	1574	1394	1334
ν_2,A"	1514	1496	1376	1347	1191
ν_4,A'	1296	1288	1343	1126	
ν_4,A'	1294	1286	1174	755	
ν_4,A'	1293	1280	1080	678	
	55	91	590	390	1142
	52	81	211	352	1066
	43	51	177	175	1049
	5	35	83	156	479
	-25	32	74	36	477
	-54	-31	-240	-890	312
					267
					186
					179

Table 3.4: The nine largest methane vibrational frequencies are displayed at the initial configuration, the early and late crossing regions and the transition state, together with the six largest frequencies of the adsorbed methyl radical (final state). The modes are labelled according to the gas phase methane modes and their C_S symmetry in CH$_4$+Ni(111) (see Fig. 3.1). The six (nine) modes evolving from the free rotations and translation of methane (H and CH_3) are unlabelled. Imaginary frequencies are indicated with a minus sign. All units are in cm^{-1}.

The vibrational frequencies obtained along the MEP using the procedure described in Section 3.2.3 are displayed in Fig. 3.5 and listed for some selected points in Table 3.4. The results show that in moving from the initial state to the TS most vibrational frequencies change considerably. This is a clear indication that many of the vibrational coordinates are involved in the dissociation. It is seen that the vibrational energy levels at the initial configuration closely resembles those of a gas phase methane molecule, as they should. In moving towards the TS region, the degeneracies among the ν_2, ν_3 and ν_4 vibrational energy levels are lifted. The modes can be labelled according to their C_S symmetry in CH$_4$ + Ni(111), giving
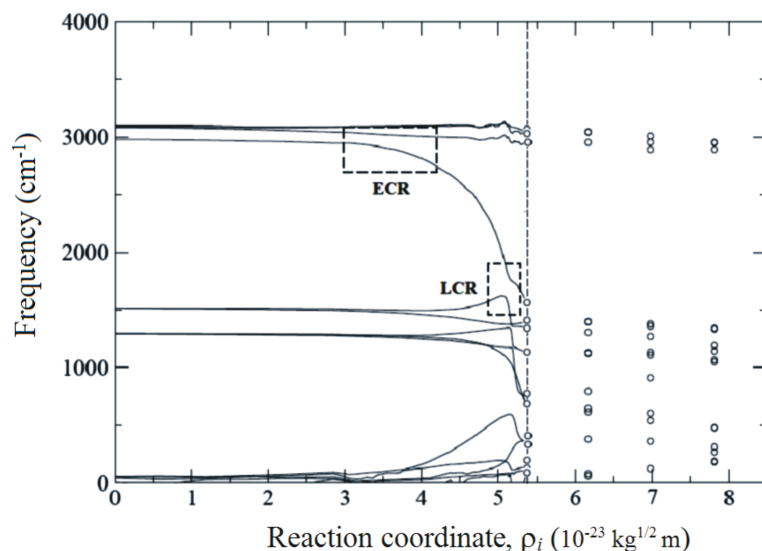
Figure 3.5: The vibrational frequencies along the reaction coordinate (see also Figs. 3.2 and 3.3) are displayed. Early and late crossings were observed around a reaction coordinate value of about 3.5 $10^{-23}kg^{1/2}m$ and 5.1 $10^{-23}kg^{1/2}m$, respectively. The dashed line indicates the transition state, and the early and late crossing regions are marked by ECR and LCR, respectively.

nine A' modes (symmetric vibrations with respect to the C_S plane, Fig. 3.1) and six A'' modes (anti-symmetric vibrations with respect to the C_S plane). For CH_4 in its initial position 5 Å above the surface (the geometry is displayed in Fig. 3.4(a)) the ν_1 mode is of A' symmetry, the two ν_2 vibrations split into one of A' and one of A'' symmetry, and the three ν_3 and three ν_4 vibrations each split into two of A' and one of A'' symmetry. Figure 3.5 and Table 3.4 also display how the three free rotations and the three free translations of the gas phase methane molecule evolve into frustrated modes. Three of these frustrated modes have A' symmetry.

Based on the obtained vibrational spectrum the zero-point energy (ZPE) can be calculated along the MEP that together with the potential energy profile yields an effective potential for vibrationally adiabatic motion of the molecule in its ground vibrational state (Fig. 3.6). An effective potential barrier height of 0.95 eV is obtained. A comparison of the potential and the effective potential along the MEP shows that ZPE effects may effectively lower the barrier to reaction by 0.14 eV.

As already noted, there are two important avoided crossing regions of the vibrational modes, one near the entrance channel (the ECR) and another one near the TS (the LCR) (see Fig. 3.5). In general, the features of the crossings can be studied by tracking the symmetry character of the normal modes and by calculating the Massey parameter, from which the crossing probability may be deduced in a crossing region. The DFT potential energy corresponding to the ECR and LCR are about 0.07 and 0.79 eV, respectively. The ECR is located in
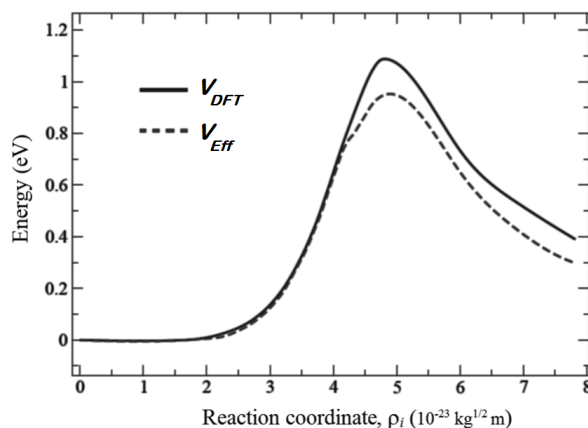
Figure 3.6: The DFT energies along the MEP with and without ZPE correction. The dashed red line represents V_{Eff}, which is the effective potential. The blue line is the potential energy along the MEP, V_{DFT}.

the region where the molecule is just beginning to climb the barrier. The geometry (Fig. 3.4(b)) is slightly reoriented with respect to the initial geometry, in which the reactive CH bond points towards the surface (Fig. 3.4(a)). The ECR shows an avoided crossing involving the vibrational fundamentals with the third and fourth largest vibrational frequencies, the associated modes having A' character. After the crossing, a 'quarantaining' of the CH stretch vibrations is observed in the CH_3 group for the third mode [33], whereas an enhancement of the amplitude of the CH stretch along the dissociating bond was found for the fourth vibrational mode. Both features are clearly shown in Fig. 3.7.

This localized CH stretch and the further softening (decreasing frequency) displayed by the vibrational fundamental with the fourth largest frequency after the crossing can be used to understand the larger reactivity of the ν_1 mode compared to that of ν_3. The ECR involves only one of the three ν_3 stretch vibrations. In other words, due to the degeneracy of the ν_3 mode, the probability is only 1/3 that CH_4 in the $1\nu_3$ state will enter the ECR along the upper curve in Fig. 3.7, which may then lead to reaction. Pre-excitation of the ν_3 mode with one quantum will promote reaction if the molecule comes in along this curve and crosses diabatically to the lower curve. To estimate the probability of the crossing, we calculated the corresponding Massey velocity employing the techniques of Section 3.2.4 and found a value of $2.560 \ 10^{-10} kg^{1/2} ms^{-1}$.

For the calculation of the Massey parameter applicable to the experiments on the reactivity of $1\nu_1$ and $1\nu_3$ methane, we used CH_4 mass weighted velocities along the reaction coordinate of $4.035 \ 10^{-10} kg^{1/2} ms^{-1}$ and $4.592 \ 10^{-10} kg^{1/2} ms^{-1}$, which correspond to the experimental collision velocities of 0.508 eV and 0.658 eV, respectively [12]. Here, we have taken into account that the molecule loses 0.07 eV of its translational energy to reach the crossing. The corresponding Massey parameters were calculated to be 0.64 and 0.56. The Massey parameter of the crossing qualitatively characterizes a transition as adiabatic, diabatic, or mixed, and the fact that the Massey parameter is of the order of one suggests that the crossing is neither

fully adiabatic nor fully diabatic. (In our analysis, we will assume that a Massey parameter in the range 0.5 - 1.5 corresponds to a mixed adiabatic/diabatic transition, with the probability of either transition being approximately 50%.) This value suggests that pre-excitation of ν_1 with one quantum should be 3 times more effective for promoting the reaction than pre-exciting ν_3, due to the asymptotic degeneracy of the latter mode and only one of the three asymptotic modes coupling to the reaction coordinate. (Our model suggests a probability of 0.5 that a molecule entering the ECR in the ν_1 state continues on the lower, reactive curve. It suggests a probability of $\frac{1}{3} \times \frac{1}{2}$ that a molecule originally in a $1\nu_3$ state enters the ECR and leaves it on the lower reactive curve.) These results demonstrate the capability of the model introduced by Halonen *et al.*, and elaborated here, to explain the experimental results of Maroni *et al.* [12], in a semi-quantitative way (the observed reactivity of methane excited in the ν_1 mode is an order of magnitude higher than that of ν_3 excited methane on Ni(100), we compute a factor 3 for CH_4+Ni(111)). Furthermore, our model confirms a characteristic feature of the previous calculations of lower dimensionality[33]: the localization of the vibrational energies in either the reactive and/or the umbrella spectator mode during the progress of the reaction.
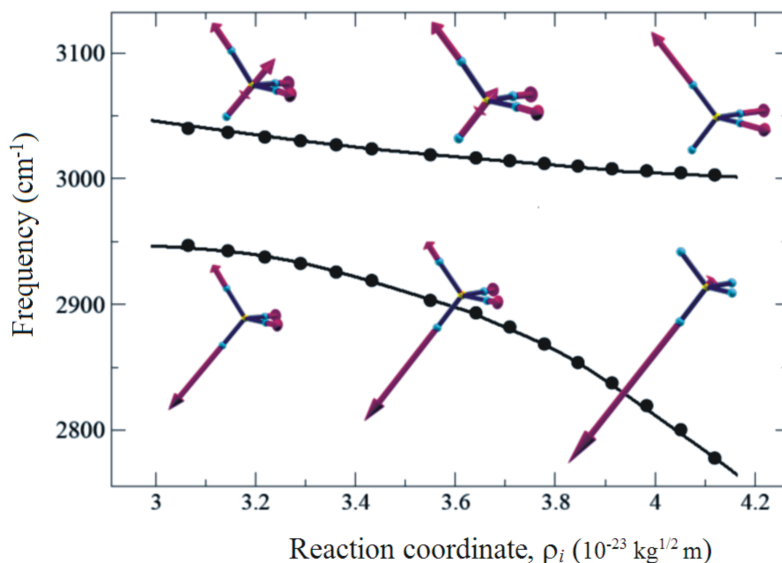
Figure 3.7: The third and fourth largest vibrational frequencies are shown as a function of the reaction coordinate, in the region where these modes display an avoided crossing. The vibrational modes at three positions are displayed. Small vectors on the C atom were not shown for the sake of clarity.

Near the TS a number of avoided crossings and symmetry-allowed crossings were observed (see Fig. 3.8). We studied in detail the first avoided crossing (labelled LCR in Fig. 3.5 and occurring at $\rho \approx 5.1 \ 10^{-23}kg^{1/2}m$ in Fig. 3.8) of the

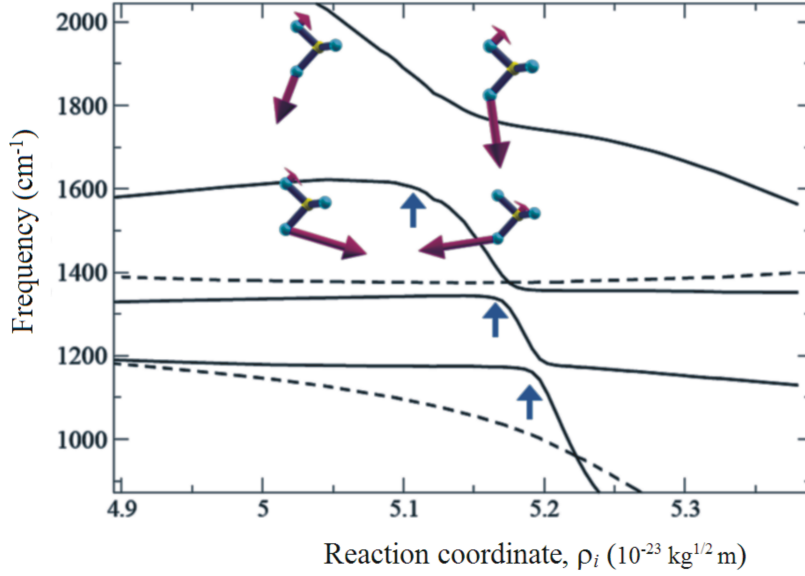Figure 3.8: The frequencies of the interacting A' modes are shown as a function of the reaction coordinate by solid lines. Avoided crossings are indicated by the blue arrows and the A" modes are indicated by the dashed lines. The two vibrational modes involved in the first avoided crossing are shown before and after the crossing.

fourth and fifth vibrational states (in the following we will simply refer to the vibrational fundamental with the n'th largest frequency as the n'th vibrational state). Before the crossing, the fourth and fifth modes correspond to stretch and bend modes, respectively, with an A' character of vibration. Following the procedure outlined in Section 3.2.5, a vibrational energy release of 0.142 eV was estimated at the LCR, which was acquired from the frequency-lowering of the fourth vibrational state. We also take into account that the molecule has to spend 0.79 eV in climbing the potential wall. With the initial kinetic energies of 0.508 eV and 0.658 eV, Eq. 3.9 then gives kinetic energies of 0.094 eV and 0.244 eV along the reaction coordinate, respectively. For calculating these kinetic energies and $V_{\Delta LCR}$, we applied a semi-empirical correction to the potential at the LCR by scaling the potential with the ratio of the experimental activation barrier of 0.77 eV [54] and the DFT barrier height of 1.09 eV. The $V_{\Delta LCR}$ is found to be 0.556 eV. Finally, we obtain from Eq. 3.8 the mass-weighted velocities of methane along the reaction coordinate at the LCR as $4.564 \ 10^{-10} kg^{1/2}ms^{-1}$ and $5.063 \ 10^{-10} kg^{1/2}ms^{-1}$, respectively. The Massey velocity found from Eq. 3.7 at the LCR (see Section 3.2.5) was $3.455 \ 10^{-11} kg^{1/2}ms^{-1}$, much smaller than that corresponding to the early crossing region. We obtain Massey parameters of 0.08 and 0.07 for the two collision energies. These low values for the Massey parameter indicate that the fourth and fifth vibrational states will pass through the LCR crossing in a diabatic fashion at the corresponding collision energies. This qualitatively shows the efficiency of the stretch vibrations to promote the reaction as compared to that of the bend vibrations, as observed by the state-resolved measurements of Juurlink *et al.* [8]: According to our calculations, methane pre-excited in a stretch vibration moves

through the LCR in a predominantly diabatic fashion, efficiently coupling to the TS mode as the molecule approaches the dissociation barrier, whereas methane pre-excited in a ν_2 vibration only weakly couples to the TS mode, using little energy in vibration as it moves diabatically through the LCR. Our findings are in qualitative agreement with those of Juurlink *et al.*, who in measurements on the reactivity of the $1\nu_3$ stretch excited and $3\nu_4$ bend excited states found a much larger vibrational efficacy of the ν_3 mode, with the $1\nu_3$ state showing a larger reactivity in spite of its vibrational energy being lower than that of the $3\nu_4$ state.

This work shows some similarities between the involvement of the vibrational coordinates of CH_4 in H abstraction reactions in the gas phase [55, 56] and in the dissociative chemisorption reaction studied here. The lowering of CH_4 frequencies is very similar in both systems. For instance, a large lowering of the ν_1 frequency as well as crossings similar to those seen here in the LCR and ECR were also observed in the gas phase reaction of CH_4 with chlorine [55, 56]. A feature observed in both reactions is that the excitation of the symmetric stretch mode enhances the reaction rate. The involvement of the frustrated molecule-surface modes in the TS region is a characteristic feature of the gas-surface reaction, that is absent in the gas phase system.

3.4   Conclusions

We have performed a vibrational analysis study based on the density functional theory, to understand the role of vibrational mode specificity in the dissociative chemisorption of methane on Ni(111). To the best of our knowledge, this is the first full-dimensional (with respect to the degrees of freedom of the molecule) study for analyzing the effect of various normal modes along a minimum energy path for a dissociative chemisorption reaction of a polyatomic molecule. We used nudged elastic band and steepest descent methods to obtain a dense MEP. The vibrational analysis was done along the MEP within the harmonic approximation. A late barrier of 1.09 eV was found, with a zero-point energy correction of 0.14 eV giving an effective barrier of 0.95 eV. The transition state resembles the product state with a considerable CH bond elongation thus indicating the importance of the stretch modes over the bend modes. These results were in agreement with previous studies.

For an accurate vibrational analysis the noise in the Hessian matrix elements was reduced by applying a fitting method to the DFT forces and a point-group symmetrization of the matrix elements. A considerable involvement of different vibrational coordinates was observed in reaching the transition state. The vibrational analysis along the MEP revealed the couplings between the normal modes and identified different allowed and avoided crossing regions with the help of the character of the vibrations. Two important avoided crossings have been discussed in connection with the corresponding Massey velocities and parameters. Based on this analysis, we find that the pre-excitation of the symmetric stretch vibration should be approximately 3 times more efficient in promoting reaction than pre-excitation of the asymmetric stretch. Our analysis implies that the bend vibrations are not strongly coupled to the reaction coordinate whereas the stretches are efficiently coupled to the reaction coordinate, thus indicating the effective-

ness of stretch modes in promoting reaction. In general, these results are in good agreement with previous mode-specific experiments.

Acknowledgements

Bibliography

[1] S. C. Tsang, J. B. Claridge, and M. L. H. Green, Catal. Today **23**, 3 (1995).

[2] G. A. Olah and A. Molnar, *Hydrocarbon Chemistry* (Wiley-Interscience, New Jersey, 2003).

[3] M. B. Lee, Q. Y. Yang, and S. T. Ceyer, J. Chem. Phys. **87**, 2724 (1987).

[4] P. M. Holmblad, J. Wambach, and I. Chorkendorff, J. Chem. Phys. **102**, 8255 (1995).

[5] L. B. F. Juurlink, R. R. Smith, and A. L. Utz, Faraday Discuss. **117**, 147 (2000).

[6] L. B. F. Juurlink, P. R. McCabe, R. R. Smith, C. L. DiCologero, and A. L. Utz, Phys. Rev. Lett. **83**, 868 (1999).

[7] R. R. Smith, D. R. Killelea, D. F. DelSesto, and A. L. Utz, Science **304**, 992 (2004).

[8] L. B. F. Juurlink, R. R. Smith, D. R. Killelea, and A. L. Utz, Phys. Rev. Lett. **94**, 208303 (2005).

[9] P. Maroni, *PhD thesis* (Ecoles Polytechniques Fédérales de Lausanne, Lausanne, 2005).

[10] R. D. Beck, P. Maroni, D. C. Papageorgopoulos, T. T. Dang, M. P. Schmid, and T. R. Rizzo, Science **302**, 98 (2003).

[11] M. P. Schmid, P. Maroni, R. D. Beck, and T. R. Rizzo, J. Chem. Phys. **117**, 8603 (2002).

[12] P. Maroni, D. C. Papageorgopoulos, M. Sacchi, T. T. Dang, R. D. Beck, and T. R. Rizzo, Phys. Rev. Lett. **94**, 246104 (2005).

[13] H. Yang and J. L. Whitten, J. Chem. Phys. **96**, 5529 (1992).

[14] P. Kratzer, B. Hammer, and J. K. Nørskov, J. Chem. Phys. **105**, 5595 (1996).

[15] J. P. Perdew, J. A. Chevary, S. H. Vosko, K. A. Jackson, M. R. Pederson, D. J. Singh, and C. Fiolhais, Phys. Rev. B **46**, 6671 (1992).

[16] J. P. Perdew, J. A. Chevary, S. H. Vosko, K. A. Jackson, M. R. Pederson, D. J. Singh, and C. Fiolhais, Phys. Rev. B **48**, 4978 (1993).

[17] H. Burghgraef, A. P. J. Jansen, and R. A. v. Santen, Chem. Phys. **177**, 407 (1993).

[18] A. D. Becke, Phys. Rev. A **38**, 3098 (1988).

[19] H. Stoll, E. Golka, and H. Preuss, Theoret. Chim. Acta **55**, 23 (1980).

[20] H. Stoll, C. M. E. Pavildou, and H. Preuss, Theoret. Chim. Acta **49**, 143 (1978).

[21] F. Abild-Pedersen, O. Lytken, J. Engbaek, G. Nielsen, I. Chorkendorff, and J. K. Nørskov, Surf. Sci. **590**, 127 (2005).

[22] B. Hammer, L. B. Hansen, and J. K. Nørskov, Phys. Rev. B **59**, 7413 (1999).

[23] R. Watwe, H. S. Bengaard, J. R. Rostrup-Nielsen, J. A. Dumesic, and J. K. Nørskov, J. Catal. **189**, 16 (2000).

[24] G. Henkelman, A. Arnaldsson, and H. Jonsson, J. Chem. Phys. **124**, 44706 (2006).

[25] S. Nave and B. Jackson, J. Chem. Phys. **127**, 224702 (2007).

[26] S. Nave and B. Jackson, Phys. Rev. Lett. **98**, 173003 (2007).

[27] S. Nave and B. Jackson, J. Chem. Phys. **130**, 54701 (2009).

[28] A. C. Luntz and J. Harris, Surf. Sci. **258**, 397 (1991).

[29] V. A. Ukraintsev and I. Harrison, J. Chem. Phys. **101**, 1564 (1994).

[30] A. Bukoski and I. Harrison, J. Chem. Phys. **118**, 9762 (2003).

[31] H. L. Abbott, A. Bukoski, D. F. Kavulak, and I. Harrison, J. Chem. Phys. **119**, 6407 (2003).

[32] R. Milot and A. P. J. Jansen, Phys. Rev. B **61**, 15657 (2000).

[33] L. Halonen, S. L. Bernasek, and D. J. Nesbitt, J. Chem. Phys. **115**, 5611 (2001).

[34] P. Hohenberg and W. Kohn, Phys. Rev. **136**, B864 (1964).

[35] W. Kohn and L. J. Sham, Phys. Rev. **140**, A1133 (1965).

[36] G. Kresse and J. Hafner, Phys. Rev. B **47**, 558 (1993).

[37] G. Kresse and J. Hafner, Phys. Rev. B **49**, 14251 (1994).

[38] G. Kresse and J. Furthmuller, Comput. Mater. Sci. **6**, 15 (1996).

[39] G. Kresse and J. Furthmuller, Phys. Rev. B **54**, 11169 (1996).

[40] P. E. Blochl, Phys. Rev. B **50**, 17953 (1994).

[41] G. Kresse and D. Joubert, Phys. Rev. B **59**, 1758 (1999).

[42] S. H. Vosko, L. Wilk, and M. Nusair, Can. J. Phys. **58**, 1200 (1980).

[43] S. R. Bahn and K. W. Jacobsen, Comput. Sci. Eng. **4**, 56 (2002), the DA-CAPO code can be freely available at, http://www.camp.dtu.dk/software.

[44] H. Jonsson, G. Mills, and K. Jacobsen, *Classical and Quantum Dynamics in Condensed Phase Simulations* (World Scientific, Singapore, 1998).

[45] G. Henkelman, B. P. Uberuaga, and H. Jonsson, J. Chem. Phys. **113**, 9901 (2000).

[46] G. Henkelman and H. Jonsson, J. Chem. Phys. **113**, 9978 (2000).

[47] VTST code can be downloaded from, http://theory.cm.utexas.edu/vsttools/code/.

[48] P. E. Blochl, O. Jepsen, and O. K. Anderson, Phys. Rev. B **49**, 16223 (1994).

[49] W. H. Press, B. P. Flannery, S. A. Teukolsky, and W. T. Vetterling, *Numerical Recipes in C: The Art of Scientific Computing* (Cambridge University Press, Cambridge, 1992).

[50] M. S. Child, *Molecular Collision Theory* (Dover, New York, 1996).

[51] I. Loris and R. Sasaki, Physics Letters A **327**, 152 (2004).

[52] J. C. Polanyi, Acc. Chem. Res. **5**, 161 (1972).

[53] W. Quapp, *The Reaction Path in Chemistry: Current Approaches and Perspectives* (Kluwer, Dordrecht, 1995).

[54] R. C. Egeberg, S. Ullmann, I. Alstrup, C. B. Mullins, and I. Chorkendorff, Surf. Sci. **497**, 183 (2002).

[55] W. T. Duncan and T. N. Truong, J. Chem. Phys. **103**, 9642 (1995).

[56] J. C. Corchado, D. G. Truhlar, and J. Espinosa-Garcia, J. Chem. Phys. **112**, 9375 (2000).

Supplementary Information

I. Fitting of the Hessian matrix

In the fitting of the Hessian matrix elements as functions of the reaction coordinate, one can take advantage of symmetry. The non-diagonal elements may be written in the form of numerical derivatives as

$$H(\alpha, \beta) = \frac{E(\Delta\alpha, \Delta\beta) - E(\Delta\alpha, -\Delta\beta) - E(-\Delta\alpha, \Delta\beta) + E(-\Delta\alpha, -\Delta\beta)}{4\delta^2}. \quad (3.10)$$

Here, α and β label any of the 15 atomic coordinates in $\{C_x, C_y, \ldots, H_{4z}\}$, $E(\Delta\alpha, \Delta\beta)$ denotes the DFT energy of CH_4 interacting with Ni(111) with a small displacement along α and β, and δ the small displacement used in the second order differencing. For example, the $H(C_x, C_y)$ (or $H(C_y, C_x)$) is 0, since $E(\Delta C_x, \Delta C_y) = E(\Delta C_x, -\Delta C_y)$ and $E(-\Delta C_x, \Delta C_y) = E(-\Delta C_x, -\Delta C_y)$.
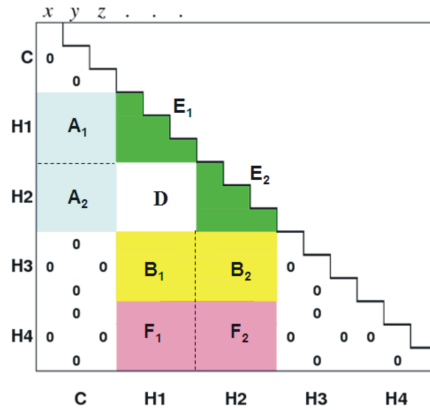
Figure 3.9: The schematic Hessian matrix for methane interacting with Ni(111) in a geometry with C_S symmetry. The 18 zeros are displayed in the lower triangle in addition with the sub-block matrices of A, D, B and F and the two triangular blocks of E_1 and E_2. The sub blocks of these main blocks are separated by a line.

From Eq. 1, one can deduce the symmetry properties of H of methane interacting with Ni(111) in a geometry belonging to the C_S symmetry (see Fig. 1): (1)

there are always 18 zero elements in the lower triangle of the Hessian matrix (see Fig. S1), (2) the main block matrices A, B and F (see Fig. 1) can be split up in six 3×3 sub-blocks, namely A_1, A_2, B_1, B_2, F_1 and F_2, in which the absolute values of all the corresponding elements in the sub-blocks corresponding to each other are numerically identical to each other except for the sign of their off-diagonal elements, (3) the triangular matrices E_1 and E_2 are also numerically the same except for the sign of their off-diagonal terms, (4) the block D is a unique block and its off-diagonal terms differ only from each other in their sign. The symmetry properties (2) and (3) may also be described as follows: let X be A, or B, or C, or E, or F. We then have for $(i, j = 1, 2, 3)$:

$$X_{ii}^1 = X_{ii}^2, \tag{3.11}$$

$$X_{ij}^1 = -X_{ij}^2, \tag{3.12}$$

The symmetry property (4) can be described by

$$D_{ij} = -D_{ji}. \tag{3.13}$$

As stated before, the numerical noise in the forces obtained from the plane wave code may alter the symmetry properties of H. To obtain a correct C_S symmetrized H, we first fitted the components of the force (gradient components) to functions of ρ, 13 model functions listed in Table 1. In each case, we simply selected the function providing the best fit by calculating the average absolute deviation. In the second step, we obtained noise reduced Hessian matrix elements using a second order numerical differencing of the force components. The obtained H was then symmetrized using

$$\hat{H}_{ij} = \hat{H}_{ji} = \frac{H_{ij} + H_{ji}}{2}. \tag{3.14}$$

The additional symmetry conditions discussed above were imposed by inserting zeros in the places illustrated in Fig. S1. We also applied 'numerical padding' to the sub-blocks. This was achieved by: (1) averaging the sub-blocks in A, B, E and F matrices by,

$$\hat{X}_{ij}^1 = \hat{X}_{ij}^2 = \frac{|X_{ij}^1| + |X_{ij}^2|}{2} \tag{3.15}$$

followed by the mapping the signs of X_{ij}^1 onto $\hat{X}_{ij}^1$ and then applying Eq. 3 to the off-diagonal elements of $\hat{X}_{ij}^2$, (2) symmetrizing the D block using,

$$\hat{D}_{ij} = \frac{|D_{ij}| + |D_{ji}|}{2} \tag{3.16}$$

and applying

$$\hat{D}_{ij} = -\hat{D}_{ji}. \tag{3.17}$$

1.	$a_1 + a_2 x$
2.	$a_1 + a_2 x + a_3 x^2$
3.	$a_1 + a_2 x^2$
4.	$a_1 + a_2 x^3$
5.	$a_1 + a_2 x + a_3 x^2 + a_4 x^3 + a_5 x^4$
6.	$a_1 + a_2 x + a_3 x^2 + a_4 x^3 + a_5 x^4 + a_6 x^5$
7.	$a_1 + a_2/x$
8.	a_1/x
9.	$a_1 + a_2/x + a_3/x^2$
10.	$a_1 + a_2/x + a_3/x^2 + a_4/x^3$
11.	$a_1 x + a_2/x^2 + a_3/x^3$
12.	$a_1(sin(x)cos(x)/x) + a_2 sin(x) + a_3 cos(x) + a_4 x$
13.	$a_1 sin(x) + a_2 cos(x)$

Table 3.5: The table shows the 13 model functions used in the fitting of the force-components. The a_i are the coefficients of the model functions. x denotes the reaction coordinate.

II. Approximation of the vibrational wavefunction by normal modes

In this section we justify the use of normal modes instead of the vibrational wave function for the Massey velocity calculations by stating the close correspondence of the *inner product* in the quantum function and classical normal eigenvector spaces. This close correspondence is based on the quantum eigenfunction being a '$\hbar$-deformation' of the classical normal mode solution.

The classical and quantum mechanical solutions of a harmonic oscillator resemble each other in several ways. Although for the system considered (CH_4 interacting with a rigid Ni(111) surface) the classical solution - the normal modes- lies on a limited 15-dimensional Hilbert space (since it is defined in an $\Re^n$ space with n=15), it shows many one-to-one correspondences with its quantum counterpart (the vibrational eigenfunction) such as unique vibrational eigenvalues and having similar spatial-properties such as orthogonality, completeness, norm, Schwarz inequality (or in general, the Gram determinants[1]) etc. Furthermore, the *inner product* in both the quantum function and classical normal mode eigenvector spaces are defined in the space of L^2 (i.e. Lebesgue space with 2-norm), which is a square-integrable (or square-summable) linear space [2]. In quantum eigenfunction space the *projection* of a vibrational eigenfunction at ρ_i on another eigenfunction at ρ_j is evaluated as the overlap integral, whereas it corresponds to the dot product of the corresponding normal mode coefficients in the classical case.

In addition to this, a proof exists of the correspondence between the classical eigenvector and vibrational quantum eigenfunction [3]. This is based on the '$\hbar$-deformation' of the classical eigenvector. The proof of this deformation does not depend on the number of particles or the potential and assumes that the quantum eigenfunctions are square integrable over $\Re^n$.

Following the above arguments, one can write the relation between the vibrational eigenfunction, Ψ, of a harmonic oscillator and the corresponding normal mode eigenvector, F, as

$$\lim_{\hbar \to 0} \Psi = F, \tag{3.18}$$

where, $F = \sum_i f_i x_i$, f_i are the components of F with respect to the Cartesian coordinates, x_i. Similarly another vibrational quantum eigenfunction, Φ corresponding to a different normal mode eigenvector, G can be written as,

$$\lim_{\hbar \to 0} \Phi = G, \tag{3.19}$$

where, $G = \sum_i g_i x_i$, and g_i are the vector components of the normal mode G. Then the correspondence between the overlap integral of Ψ and Φ, and the dot product of the F and G is related by,

$$\lim_{\hbar \to 0} \langle \Psi | \Phi \rangle = \sum_i f_i g_i = \langle F | G \rangle. \tag{3.20}$$

Bibiliography:

1. *Methods of Mathematical Physics*, Vol. 1, by R. Courant and D. Hilbert, Interscience publishers, inc., New York, (7/e), pgs. 34, 62 (1966).

2. *Real Analysis: Measure Theory, Integration, and Hilbert Spaces*, by E. M. Stein and R. Shakarchi, Princeton University Press, pg. 157 (2004).

3. I. Loris and R. Sasaki, Physics Letters A, **327**, 152 (2004).

Chapter 4

Quantum dynamics of dissociative chemisorption of CH$_4$ on Ni(111): Influence of the bending vibration

This chapter is based on:

G. P. Krishnamohan, R. A. Olsen, G. J. Kroes, F. Gatti, and S. Woittequand, J. Chem. Phys., in press.

Abstract

Two-, three- and four-dimensional quantum dynamic calculations are performed on the dissociative chemisorption of CH$_4$ on Ni(111) using the multiconfiguration time-dependent Hartree method (MCTDH). The potential energy surface used for these calculations is 15-dimensional (15D) and was obtained with density functional theory for points which are concentrated in the region that is dynamically relevant to reaction. Many reduced-dimensionality calculations were already performed on this system, but the molecule was generally treated as a pseudo-diatomic. The main improvement of our model is that we try to describe CH$_4$ as a polyatomic molecule, by including a degree of freedom describing a bending vibration in our 3D and 4D models. Using a polyspherical coordinate system, a general expression for the 15D kinetic energy operator is derived, which discards all the singularities in the operator and includes rotational and Coriolis coupling. We use 7 rigid constraints to fix the CH$_3$ umbrella of the molecule to its gas phase equilibrium geometry and to derive two-dimensional, three-dimensional, and four-dimensional Hamiltonians, which were used in the MCTDH method. Only four degrees of freedom evolve strongly along the 15D minimum energy path: the distance of the center of mass of the molecule to the surface, the dissociative C-H bond distance, the polar orientation of the molecule and the bending angle between the dissociative C-H bond and the umbrella. A selection of these coordinates is included in each of our models. The polar rotation is found to be important in determining the mode selective behavior of the reaction. Furthermore, our calculations are in good agreement with the finding of Xiang et al. [Y. Xiang, J. Z. H. Zhang, and D. Y. Wang, *J. Chem. Phys.*, **117**, 7698 (2002)] in their reduced dimensional calculation that the helicopter motion of the umbrella symmetry axis is less efficient than its cartwheel motion for promoting the reaction. The effect of pre-exciting the bend modes is qualitatively incorrect at higher energies, suggesting

the necessity of including additional rotational and vibrational degrees of freedom in the model.

4.1   Introduction

Because of its industrial significance, methane dissociation on metals is one of the most studied reactions in surface science. The dissociative chemisorption of methane on nickel to form surface-adsorbed methyl and hydrogen is rate-limiting in the chief industrial process (steam reforming) for producing the energy carrier of the future (hydrogen) [1]. The dissociative chemisorption probability of CH_4 has been measured for selectively pre-excited vibrational modes as a function of the normal translational energy E_{Z_i} and surface temperature T_S in molecular beam experiments for many metal surfaces, and particularly Ni(100) and Ni(111) [2, 3, 4, 5, 6, 7, 8, 9, 10, 11, 12, 13, 14]. The experimental results bring to light the non-statistical behaviour of the reaction. Juurlink et al. found that one quantum of the antisymmetric C-H stretch ν_3 is slightly less effective than E_{Z_i} in promoting reactivity on Ni(100) [6, 7] while Schmid et al. found that two quanta of ν_3 is only 80% as effective as E_{Z_i} [8]. Likewise, Juurlink et al. showed that three quanta of the triply degenerate bending vibration ν_4 is only 72% as effective as the normal collision energy [12]. In contrast, Smith et al. found that one ν_3 quantum is 25% more effective than E_{Z_i} on Ni(111) [11]. For doubly deuterated methane (CD_2H_2) on Ni(100), Beck et al. observed that the reaction probability with two quanta of excitation in one C-H bond was greater by as much as a factor of 5 than with one quantum of excitation in each of the two C-H bonds [9]. Juurlink et al. [12] found that $3\nu_4$ promotes reaction less effectively than one antisymmetric C-H stretch ν_3 quantum on both Ni(100) and Ni(111), even through $3\nu_4$ contains 30% more energy . The symmetric stretch ν_1 is much more effective for promoting reaction than the antisymmetric stretch ν_3 on Ni(100) [13]. State-resolved experiments on dissociative chemisorption of methane have recently been reviewed by Juurlink et al. [14].

These results clearly exclude the possibility of using statistical models to describe correctly the mechanism of this process and attest to the importance of full-dimensional calculations of the reaction dynamics to understand the vibrational selectivity. Furthermore, calculations are necessary to yield predictions of the vibrational efficacy of the ν_2 symmetric bend mode (which is not infrared active) and that of stretch-bend combination bands for promoting the reactivity.

Up to now, dynamics calculations on CH_4/Ni(111) were generally performed with approximate models, where CH_4 is described as a pseudodiatomic molecule R-H, with R = CH_3 [15, 16, 17, 18, 19]. However, such models do not allow one to check the relative efficiency of the vibrational modes since only one C-H stretch is included and, they do not properly include effects of the rotational orientation of CH_4. This last problem was partially fixed with some new models including the full 3D rotation of the molecule [20, 21].

The first dynamics study of methane dissociation, by Luntz and Harris [15], focused on thermally assisted tunneling. Methane was modeled as a quasidiatomic R-H and only two molecular degrees of freedom were included: the R-H bond length, r, and the center of mass (COM) distance of the molecule above the surface,

Z. The bond was held fixed at an angle approximating that of the transition state. The authors used an empirical reduced dimensionality potential energy surface (PES) with parameters meant to describe the interaction of CH_4 with a Pt(111) or a Ni(111) surface. Their PES was taken as universal, neglecting the dependence on the metal substrate. This restriction was mainly due to the lack of information available on CH_4/metal surface systems at the time. The model used provided qualitative agreement with molecular beam [2, 22, 23] and thermal activation experiments [24].

Jansen and Burghgraef proposed a three dimensional model including in addition to r and Z the polar orientation of CH_4, β (defined as the angle between the threefold axis of CH_3 and the surface normal) [16]. They built an analytical potential energy surface based on density functional theory (DFT) calculations on CH_4 on Ni(111) [25, 26] and they computed dissociation using the MCTDH method. They observed that the dissociation probability scales exponentially with the translational energy of CH_4 and that the inclusion of the rotation decreases the dissociation probability.

Subsequently, Carré and Jackson [17] proposed a pseudo-four dimensional model, which in addition to the polar orientation of C-H also considered the projection of the molecule's angular momentum J on the surface, m_J (where m_J is conserved since the surface was treated as flat). They used a LEPS (London-Eyring-Polyani-Sato) potential [27, 28, 29] to fit the results of Yang and Whitten's ab initio studies of CH_4 dissociation over the atop site of Ni(111) [30, 31]. Their results showed good agreement with experiments for the dependence of the dissociation probability on incident energy and surface temperature. However, the PES was built for Ni(111) and the experimental results used for the comparison were for CH_4/Ni(100) [3].

Jackson and co. have recently published a set of papers focusing on the lattice motion and relaxation effects on the reactivity [18, 19, 32, 33, 34]. The lattice motion was included with a new degree of freedom Q, corresponding to the displacement of an atop nickel atom along the normal to the surface. Although these reduced dimensionality models do not yet allow the computation of relative vibrational efficiencies for promoting dissociation, they provide important insights into other features of the reaction such as surface temperature (T_S) effects.

The semirigid vibrating rotor target (SVRT) model was applied to CH_4/Ni(111) to describe the effect of the 3D rotational motion of the molecule on reaction [20, 21]. In this treatment, the molecule is decomposed into two rigid components ($H+CH_3$) with the pseudovibrational coordinate r describing the distance between the H-atom and the center of mass of CH_3. The DOF used were Z, r, θ and χ, the torsional angle of the $H - CH_3$ complex along the coordinate r. The M_J-dependence was included using the flat surface approximation. This model is still a pseudo-diatomic one with a correction to describe the 3D rotation. The autors have shown with their model that the dissociation probability is strongly dependent on the molecule's initial orientation with respect to the surface as characterized by the combination of the three quantum numbers (J, M_J, K).

A 10D model, including all nine vibrational degrees of freedom of the molecule and the molecule-surface distance (Z) has been used in a MCTDH study of inelastic scattering of CH_4 from Ni(111) [35]. The study showed that the PES and orientation of the molecule strongly correlates with the excitation probabilities for

the stretch modes. The excitations of ν_1 and ν_3 stretch modes were found to occur with high probability and an elongation of the reactive C-H bond length was observed - a characteristic feature of a late barrier system. But the link made between inelasticity of the modes in scattering and their effectiveness for promoting reaction was rather speculative.

Many approximate models were already used to study some specific features of the dissociative chemisorption of $CH_4/Ni(111)$. Our ultimate goal is to check the relative efficiency of the methane vibrational modes for promoting reaction. To achieve this, we need a new theoretical approach including the description of the 9 vibrational modes for promoting reaction. The first innovation of our work is the use of a 15 dimensional PES obtained from DFT. For the dynamics, we derive a general expression for the 15D kinetic energy operator (KEO) consistent with the potential. In our approach, we only study the system with reduced dimensionality Hamiltonians. This was achieved by deriving reduced dimensional KEOs from the fifteen dimensional KEO using the method of constraints. First, we describe the theoretical methods used for this work in Sections 4.2 and 4.3. Then, we present the results obtained from two-, three- and four-dimensional (2D, 3D and 4D) constrained models in Sections 4.4.1, 4.4.2 and 4.4.3, respectively. Conclusions are provided in Section 4.5.

4.2   Potential Energy Surface

We use the modified Shepard (MS) interpolation method [36, 37, 38] to build the 15D PES for the $CH_4/Ni(111)$ system. This method, which was originally developed for gas phase systems, has been adapted to molecule-surface reactions [39]. The degrees of freedom considered for this part are the fifteen Cartesian coordinates of the CH_4 atoms. The PES is grown using classical trajectories to ensure that the PES is mostly based on points in the dynamically relevant regions of coordinate space.

We make two main approximations: (a) Firstly, we use the Born-Oppenheimer approximation, assuming that the reaction takes place on the electronic ground state PES and that electron-hole pair excitations are not important for this system [40, 41]. (b) Secondly, we keep the surface atoms fixed in the calculations, thereby neglecting energy transfer to and from phonons. We make this approximation even though the work by Nave and Jackson has shown that energy exchange with phonons may have an important role, but in our work we want to focus on the effects of pre-exciting different vibrations and of pre-exciting the rotation of the molecule on reaction.

4.2.1   DFT calculations

The electronic structure calculations used spin-polarized DFT [42, 43] as implemented in the DACAPO code [44, 45]. Nonlocal ultrasoft pseudopotentials were used to represent the electron - ion-core interactions and the Kohn-Sham wave functions were expanded in a plane wave basis set. In all calculations the RPBE functional is chosen to describe the exchange-correlation interaction at the generalized gradient approximation (GGA) level.

The bulk lattice constant of fcc Ni was found to be 3.56 Å by minimizing the total energy with respect to the bulk lattice constant. This is in good agreement with the experimental value of 3.52 Å [46]. A $8 \times 8 \times 8$ Monkhorst-Pack k-point grid [47] and a plane wave (PW) cut-off of 800 eV were used in the bulk calculations.

To get a Ni slab with an exposed (111) surface, interlayer distance relaxation was carried out using a 25 Å supercell with a PW cut-off of 600 eV, a density wave (DW) cut-off of 800 eV and a $6 \times 6 \times 1$ Monkhorst-Pack grid. It was found that a 3 layer slab is sufficient to converge the CH_4/Ni(111) interaction energy to within 0.02 eV. In this slab the interlayer distance was slightly compressed by 0.029 Å with respect to the bulk case.

CH_4 + Ni(111) was modeled using a fixed three layer nickel slab and a 2×2 unit cell. A vacuum distance of 12 Å was found to be adequate to converge the interaction energy to within 1 meV. The Brillouine zone sampling was done by using a Chadi-Cohen scheme [48] where 9 k-points were used in the irreducible Brillouine zone and the interaction energy was converged to within 0.04 eV. A PW cut-off of 350 eV and a density wave cut-off of 700 eV were needed to get the desired accuracy of 0.04 eV in the molecule-surface interaction energy calculation. The effect of spin-polarization was found to be important for obtaining an accurate reaction barrier height. The spin-polarized and spin-unpolarized barrier heights differ by 0.25 eV.

To calculate Hessian matrix elements for the GROW code we used a two layer slab with a vacuum distance of 8 Å. This was chosen as a compromise between computational efficiency and accuracy. The interlayer distance was relaxed for the two layer slab and a compression of 0.0274 Å was found with respect to the bulk case. A PW cut-off of 300 eV, a DW cut-off of 600 eV and a $3 \times 3 \times 1$ Monkhorst-Pack grid were used. The Hessian matrix elements were calculated by finite differencing of the gradients using a forward difference method, employing Cartesian coordinate displacements of 0.01 Å.

4.2.2 The initial data set of the PES

The initial PES for the GROW calculations was constructed from reaction path geometries and a sparse set of optimized DFT CH_4 geometries distributed over the unit cell for the GROW calculation (see below). We obtained a converged nudged elastic band (NEB) [49, 50] reaction path based on an initial state where CH_4 is in the gas phase and a final state where the dissociated fragments of hydrogen and methyl are adsorbed on the hcp and fcc hollow sites, respectively [51]. For this, we used the NEB module from the Atomistic simulation environment (ASE) [45, 52] program in conjunction with the DFT code DACAPO. In the DFT calculations, Cartesian force components of the initial and final structures were minimized to less than 10^{-4} eV/Å for each atom. The motion of methane was always restricted to a plane along the incidence direction that intersects nearest neighbour surface nickel atoms. The minimization of the band was done by a quasi-Newton method until the maximum force acting on all atoms was less than 0.1 eV/Å. This minimum energy path (MEP) was described by 10 images between the initial and final states. The DFT points describing the reaction path therefore consist of 12 points. Another MEP consisting of 38 DFT data points was obtained using adaptive-NEB

(ANEB) [53] and NEB calculations without imposing any geometrical constraints on the methane. These points did not belong to the initial data set but were added to the PES at an early stage of its growing phase (after 20% of the growth of the PES had been completed). Furthermore, we have also used the ANEB method to find the transition state (see Fig. 4.1), which was also added to the data set.

To reduce the computational cost of building a 15-dimensional PES, all other DFT calculations (i.e. all those excluding the (A)NEB calculations) for the GROW code were restricted to a symmetry unique triangle located in the surface unit cell (Fig. 4.2). To construct this triangle, the approximation was made that the interaction of CH_4 with the fcc site is equal to the interaction of CH_4 with the hcp site. In other words, we treat the plane indicated by the dashed line in Fig. 4.2 as a mirror plane. The approximation was tested with initial geometries, barrier geometries and the final dissociated geometries, in which the energy difference was largest for the dissociated geometry, i.e. 15 meV. This approximation leads to the choice of a symmetry unique triangle indicated by dashed lines and red dots in Fig. 4.2. By applying the appropriate symmetry operations, all geometries can be related to this triangle.
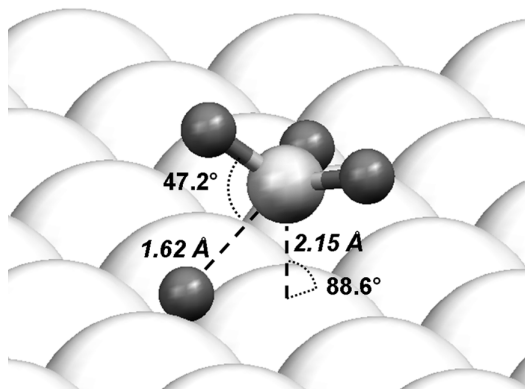

Figure 4.1: The transition state geometry of methane adsorbed on a Ni(111) surface as obtained using the ANEB method. The H atom is near the hcp-hollow site and the C atom is above a surface Ni atom.

Additionally, the initial PES was built using a number of selected DFT points in the symmetry unique triangle, including four sets of points in which each set consists of 29 optimized DFT geometries. The carbon atom-surface distances of these sets were fixed at 2, 2.5, 3 and 4.25 Å above the surface and its XY values as indicated in Fig. 4.2, after which all other coordinates of CH_4, i.e., the coordinates of the H-atoms, were optimized. These geometries were also included in the initial PES together with three optimized CH_4 geometries, where the carbon atom-surface distance was fixed at 4, 5 and 6 Å above the atop Ni atom. In all cases, we used CH_4 geometries in which one CH bond was pointing towards the surface as our initial state for the geometry optimization. The quasi-Newton method was used for these optimizations.

In summary, the initial data base of DFT points, gradients and Hessians contains data from (1) converged reaction path geometries and (2) non-uniformly

distributed and optimized CH_4 geometries on a grid defined on the symmetry unique triangle located in the surface unit cell. All points (i.e., also the NEB and ANEB points) have their COM located inside this triangle.
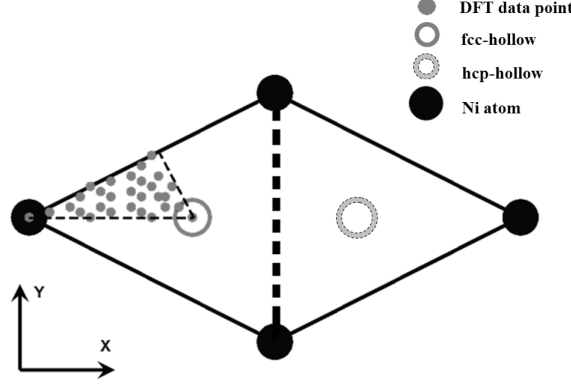

Figure 4.2: The 29 DFT points in the (X, Y) representation in the symmetry unique triangle of the unit cell. The small dots indicate the position of the carbon atoms in the symmetry unique triangle and the thick dashed line indicates the plane that we approximate as a mirror plane.

4.2.3 PES for the dynamics

The PES used for the dynamics was obtained from the interpolation of a set of 4931 DFT data points.

Interpolation

Using the MS method, the interpolated PES is given by a weighted series of Taylor expansions centered on DFT data points, sampled throughtout the configuration space of the system. Any configuration of the system is defined by the vector $\vec{Q} = \left(1/R_1, \ldots, 1/R_{n(n-1)/2}\right)$, where n is the number of atoms needed to model the system. The inverse interatomic distances, $Q_i = 1/R_i$, are used to get a physically more reasonable behavior when two atoms are close to each other [54].

For each geometry $\vec{Q}$, a set of $3n - 6$ algebraically independent linear combinations of the $n(n-1)/2$ interatomic distances, $\zeta\left(\vec{Q}\right)$, can be defined in terms of the inverse distance as

$$\zeta_m = \sum_{k=1}^{n(n-1)/2} U_{mk} Q_k \qquad (m = 1, \ldots, 3n - 6) \tag{4.1}$$

where U_{mk} is the transformation matrix from reciprocal bond lengths to the new coordinates [55]. The potential energy at a configuration $\vec{Q}$ can be expanded as a second-order Taylor expansion $T_i\left(\vec{Q}\right)$

$$\begin{aligned} T_i\left(\vec{Q}\right) &= V\left[\vec{Q}\,(i)\right] + \sum_{k=1}^{3n-6} \left[\zeta_k - \zeta_k\,(i)\right] \left.\frac{\partial V}{\partial \zeta_k}\right|_{\vec{Q}=\vec{Q}(i)} \\ &\quad + \frac{1}{2} \sum_{k=1}^{3n-6} \sum_{j=1}^{3n-6} \left[\zeta_k - \zeta_k\,(i)\right]\left[\zeta_j - \zeta_j\,(i)\right] \left.\frac{\partial^2 V}{\partial \zeta_k \partial \zeta_j}\right|_{\vec{Q}=\vec{Q}(i)} \end{aligned} \tag{4.2}$$

where $V\left[\vec{Q}\left(i\right)\right]$ is the potential value at $\vec{Q}\left(i\right)$, and the gradients at this point are computed analytically by DACAPO. The second derivatives are computed from the gradients using forward differencing.

The total potential energy at any configuration $\vec{Q}$ is then taken as

$$V\left(\vec{Q}\right) = \sum_{g \in G} \sum_{i=1}^{N_{data}} w_{g \circ i}\left(\vec{Q}\right) T_{g \circ i}\left(\vec{Q}\right) \tag{4.3}$$

where $T_{g \circ i}\left(\vec{Q}\right)$ represents a second-order Taylor expansion and $w_{g \circ i}\left(\vec{Q}\right)$ a normalized weight function [39, 56]. N_{data} is the number of DFT data configurations in the interpolation, G is the symmetry group, and $g \circ i$ denotes the transformation of the ith data point by the group element g. To take into account the full symmetry of the system, a sum is taken over both the DFT data points and their symmetry equivalent points.

Switch between gas phase and molecule/surface PES

Since we focus on the reaction of CH_4 in specific initial states, it is important to get a precise description of the vibrational states of CH_4 in the asymptotic region (far from the surface, where the interaction between the molecule and the surface is negligible). To allow this to be done, we calculated the CH_4 gas phase potential (V_M) in the same way as for CH_4/Ni(111) (V_{MS}), but without the surface atoms (Ni).

The PES used for the dynamics is a combination of V_{MS} and V_M. We explain it here for the 2D (Z, R_1) model, but the application to another model is straightforward.

A switching function is used along the Z coordinate to switch from the gas phase to the molecule-surface PES. For all our calculations, the Z-grid starts at 1 a_0 from the surface and ends at 12 a_0. When the molecule is far from the surface (at the beginning of the propagation), we use the gas phase potential

$$V(Z, R_1) = V_M(R_1) \qquad 10 < Z \leqslant 12\, a_0 \tag{4.4}$$

The resulting PES is independent of Z in this region. From 10 to 8 a_0 the potential is switched from V_M to $V_{MS}(Z = 8\, a_0)$

$$V(Z, R_1) = [1 - f_s(Z)]\, V_{MS}(Z = 8\, a_0, R_1) + f_s(Z)\, V_M(R_1), \qquad 8 < Z \leqslant 10\, a_0 \tag{4.5}$$

where $f_s(Z)$ is the switch function [57] defined as

$$f_S(Z) = \frac{1}{2} - \frac{1}{2}\cos\gamma, \qquad \gamma = \frac{[Z - (Z_0 - \Delta Z)]\,\pi}{2\Delta Z} \tag{4.6}$$

with $Z_0 = 9\, a_0$ and $\Delta Z = 1\, a_0$ V_M and $V_{MS}(Z = 8\, a_0)$ are only slightly different and so 2 a_0 are enough to switch from one to the other potential. Finally, in the interaction region, $Z \leqslant 8\, a_0$, we use V_{MS}

$$V(Z, R_1) = V_{MS}(Z, R_1), \qquad Z \leqslant 8\, a_0 \tag{4.7}$$

4.3   Models and methods

Although the PES is full-dimensional as far as the molecular degrees of freedom are concerned, we present in this paper dynamical models including only the most

important molecular degrees of freedom (DOFs) of the system. These DOFs are the molecule-surface distance (Z), the distance between the COM of CH_3 and H (R_1), the polar angle of orientation of the umbrella symmetry axis (β) and the angle between R_1 and the symmetry axis of the CH_3 umbrella (θ_1). The remaining coordinates (Section 4.3.1) are kept fixed to parameters corresponding to relevant geometries of the system. These parameters are chosen to achieve the following description of the system: (a) The X,Y COM coordinates of the molecule are kept fixed to values corresponding to impact on a top site. (b) The CH_3 umbrella is kept frozen to its gas phase geometry during the reaction. (c) The first and third Euler angles defining the orientation of the molecule (α and γ) and the azimuthal orientation of the reactive bond relative to the CH_3 umbrella (φ_1) are kept fixed to the transition state geometry values.

## 4.3.1 Kinetic energy operator

We report the kinetic energy operator (KEO) and the method used to derive it in this part of our paper. The 3 degrees of freedom (X, Y, Z) corresponding to the translational motion of the molecule with respect to the surface are not considered further below since the translation is not coupled to the vibrational and rotational motions of the molecule. The KEO operator for the COM motion is

$$-\frac{\hbar^2}{2M}\left[\frac{\partial^2}{\partial X^2} + \frac{\partial^2}{\partial Y^2} + \frac{\partial^2}{\partial Z^2}\right]. \tag{4.8}$$

Here, M is the mass of the molecule.

4.3.1.1 Full-D KEO

The polyspherical approach [58, 59, 60] is a general method for deriving kinetic energy operators. This formalism, which is based on a polyspherical parametrization of a N-atom system, can be applied whatever the number of atoms and whatever the set of vectors: Jacobi, Radau, valence, etc. In this formalism, the KEO is not restricted to the total $J = 0$ case and hence may include overall rotation and Coriolis coupling. This approach begins with choosing a set of $N - 1$ vectors which connect the N atoms of the system. For the present case, the four Jacobi vectors, $\vec{R}_i$ ($i = 1, \ldots, 4$), that are represented in Fig. 4.3 are chosen to describe the configuration of CH_4. $\vec{R}_2$ is the vector joining two H-atoms of the rigid CH_3 umbrella, $\vec{R}_3$ is the vector joining the COM of $\vec{R}_2$ to another H-atom belonging to this umbrella, $\vec{R}_4$ is the vector joining the COM of $\vec{R}_3$ (the COM of the three H-atoms belonging to the umbrella) to the C-atom and $\vec{R}_1$ is the vector joining the COM of $\vec{R}_4$ (the COM of the CH_3 umbrella) to the remaining, reactive H-atom. These four vectors are in turn parametrized by 9 polyspherical coordinates (R_1, R_2, R_3, R_4, θ_1, θ_2, θ_3, φ_1, φ_2), and three Euler angles (α, β, γ) which orient the molecule such that $\vec{R}_4$ is parallel to the body-fixed z-axis and $\vec{R}_3$ lies in the (xz, $x > 0$) body-fixed half-plane. The vectors $\vec{R}_1$, $\vec{R}_2$ and $\vec{R}_3$ are parametrized by their spherical angles in the body-fixed frame (Fig. 4.4). The three Euler angles α, β, γ correspond respectively to the spherical angles φ_4, θ_4, φ_3 defined in the space-fixed (SF) frame.
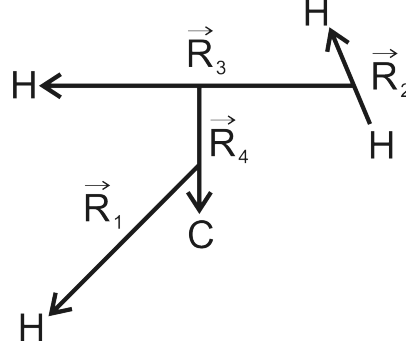
Figure 4.3: Jacobi vectors for CH_4.

The 12D KEO of the CH_4 molecule in polyspherical coordinates appears as a particular case of the general expression which is discussed in Ref. [58]. Comparing with eqs. (4), (A1), (A2) and (A3) of Ref. [58] one has to apply these general equations to the present case characterized by $N = 5$ atoms. The algorithm, outlined in Ref. [58], yields the KEO

$$\hat{T} = \sum_{l,m}^{9} \frac{\hat{P}_l^\dagger G_{l,m} \hat{P}_m}{2} + \sum_{l=1}^{9} \sum_{a=x,y,z} \frac{\hat{P}_l^\dagger C_{l,a} \hat{J}_a + \hat{J}_a C_{a,l} \hat{P}_l}{2} + \sum_{a=x,y,z} \sum_{b=x,y,z} \frac{\hat{J}_a \Gamma_{a,b} \hat{J}_b}{2} \quad (4.9)$$

where $\hat{P}_l$ denote the momenta conjugate to the 9 polyspherical coordinates and the $\hat{J}_a$ denote the body-fixed components of the total angular momentum $\hat{\vec{J}}$. The matrix $\mathbf{G}$, $\mathbf{C}$ and $\mathbf{\Gamma}$ parametrize the vibrational, Coriolis and rotational kinetic couplings.

The full 12D operator that we derived will be presented elsewhere [61].
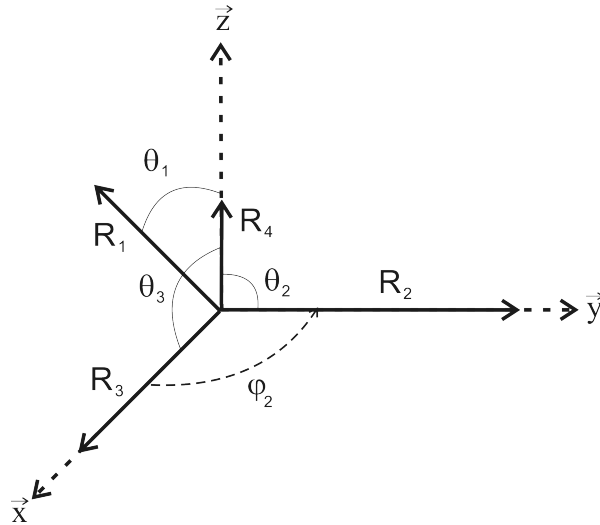
Figure 4.4: Polyspherical coordinates for CH_4. Only the non-zero angles of our constrained model are represented.

4.3.1.2 Rigidly constrained KEO

We subject the system to the following constraints:

$$
\begin{aligned}
R_2|_0 &= R_{H-H} = 3.393 \, a.u. \\
R_3|_0 &= R_{H_2-H} = 2.939 \, a.u. \\
R_4|_0 &= R_{H_3-C} = 0.693 \, a.u. \\
\theta_2|_0 &= \tfrac{\pi}{2} \\
\theta_3|_0 &= \tfrac{\pi}{2} \\
\varphi_1|_0 &= 0 \\
\varphi_2|_0 &= \tfrac{\pi}{2}
\end{aligned}
\tag{4.10}
$$

The constraints applied on R_2, R_3, R_4, θ_2, θ_3 and φ_2 are used to fix the CH_3 umbrella of the molecule to its gas phase equilibrium geometry. The one applied on φ_1 is used to place the reactive C-H bond in the plane containing $\vec{R}_3$ and $\vec{R}_4$, the reactive C-H bond almost lying in this plane in the transition state.

Constrained KE operators cannot be directly obtained from Eq. (4.9). The rigorous derivation of rigidly and adiabatically constrained operators was presented in a general context in Ref. [62]. In the rigidly constrained approach, several internal degrees of freedom, the m inactive molecular coordinates $\mathbf{q''}$, are frozen, while the remaining $n = 3N - 6 - m$ molecular coordinates $\mathbf{q'}$ are active. The constrained kinetic energy operator reads

$$
2\hat{T}_{rigid} = \begin{bmatrix} \hat{\mathbf{P}}'^\dagger & \hat{\mathbf{P}}''^\dagger & \hat{\mathbf{J}} \end{bmatrix} \begin{bmatrix} \mathbf{G'} & \boldsymbol{\sigma}^T & \mathbf{C'}^T \\ \boldsymbol{\sigma} & \mathbf{G''} & \mathbf{C''}^T \\ \mathbf{C'} & \mathbf{C''} & \boldsymbol{\Gamma} \end{bmatrix} \begin{bmatrix} \hat{\mathbf{P}}'^T \\ \hat{\mathbf{P}}''^T \\ \hat{\mathbf{J}}^T \end{bmatrix}
\tag{4.11}
$$

where the sandwiched matrix is $(3N - 3)$-dimensional. Since here the inactive coordinates are fixed once and for all, the $m = 3N - 6 - n$ rigid constraints on the molecular vibrations can be expressed as

$$
q_i'' = q_i''|_0, \quad i = 1, \ldots, 7
\tag{4.12}
$$

The resulting rigorous KEO can be obtained by applying the coordinate transformation from $\{q', q''\}$ to $\{q', q''|_0\}$. We then obtain the following expression of the constrained KEO

$$
\begin{aligned}
2\hat{T}_{rigid} = \; & \hat{\mathbf{P}}'^\dagger \left(\mathbf{G'} - \boldsymbol{\sigma}^T \cdot \mathbf{G''}^{-1} \cdot \boldsymbol{\sigma} \right)\Big|_0 \hat{\mathbf{P}}'^T + \hat{\mathbf{J}} \left(\mathbf{C'}^T - \boldsymbol{\sigma}^T \cdot \mathbf{G''}^{-1} \cdot \mathbf{C''}^T \right)\Big|_0 \hat{\mathbf{P}}'^T \\
& + \hat{\mathbf{P}}' \left(\mathbf{C'} - \mathbf{C''} \cdot \mathbf{G''}^{-1} \cdot \boldsymbol{\sigma} \right)\Big|_0 \hat{\mathbf{J}}^T + \hat{\mathbf{J}} \left(\boldsymbol{\Gamma} - \mathbf{C''} \cdot \mathbf{G''}^{-1} \cdot \mathbf{C''}^T \right)\Big|_0 \hat{\mathbf{J}}^T
\end{aligned}
\tag{4.13}
$$

where $|_0$ means that the inactive coordinates are fixed to their equilibrium geometries (4.10).

The KEO corresponding to our constrained model finally reads

$$
\hat{T} = -\frac{M_{R_1}}{2} \frac{\partial^2}{\partial R_1^2} - \frac{1}{2} \left(\frac{M_{R_3} M_{R_4}}{M_{R_4} R_3^2 + M_{R_3} R_4^2} + \frac{M_{R_1}}{R_1^2} \right) \frac{\partial^2}{\partial \theta_1^2} + \frac{1}{2} \sum_{a=x,y,z} \hat{J}_a \Gamma_{rigid}^{(aa)} \hat{J}_a
\tag{4.14}
$$

where $\boldsymbol{\Gamma}_{rigid} = \left(\boldsymbol{\Gamma} - \mathbf{C''} \cdot \mathbf{G''}^{-1} \cdot \mathbf{C''}^T \right)\Big|_0$ is the matrix which parametrizes the rotation of the constrained model and contains the following non-zero elements

$$\Gamma_{rigid}^{(xx)} = \frac{M_{R_2} M_{R_4} \left[M_{R_2} M_{R_3} R_1^2 + \frac{M_{R_1} \left(M_{R_3} R_2^2 + M_{R_2} R_3^2 \right)}{\sin^2 \theta_1} \right]}{M_{R_2} M_{R_4} R_1^2 \left(M_{R_3} R_2^2 + M_{R_2} R_3^2 \right) \cot^2 \theta_1 + \left(M_{R_4} R_2^2 + M_{R_2} R_4^2 \right) \left[M_{R_2} M_{R_3} R_1^2 + \frac{M_{R_1} \left(M_{R_3} R_2^2 + M_{R_2} R_3^2 \right)}{\sin^2 \theta_1} \right]}$$

$$\Gamma_{rigid}^{(yy)} = \frac{M_{R_3} M_{R_4}}{M_{R_4} R_3^2 + M_{R_3} R_4^2}$$

$$\Gamma_{rigid}^{(zz)} = \frac{M_{R_2} M_{R_3} \left[M_{R_2} M_{R_4} R_1^2 \cot^2 \theta_1 + \frac{M_{R_1} \left(M_{R_4} R_2^2 + M_{R_2} R_4^2 \right)}{\sin^2 \theta_1} \right]}{M_{R_2} M_{R_4} R_1^2 \left(M_{R_3} R_2^2 + M_{R_2} R_3^2 \right) \cot^2 \theta_1 + \left(M_{R_4} R_2^2 + M_{R_2} R_4^2 \right) \left[M_{R_2} M_{R_3} R_1^2 + \frac{M_{R_1} \left(M_{R_3} R_2^2 + M_{R_2} R_3^2 \right)}{\sin^2 \theta_1} \right]}$$

$$\Gamma_{rigid}^{(xz)} = \Gamma_{rigid}^{(zx)} =$$
$$\frac{M_{R_2}^2 M_{R_3} M_{R_4} R_1^2 \cot \theta_1}{M_{R_2} M_{R_4} R_1^2 \left(M_{R_3} R_2^2 + M_{R_2} R_3^2 \right) \cot^2 \theta_1 + \left(M_{R_4} R_2^2 + M_{R_2} R_4^2 \right) \left[M_{R_2} M_{R_3} R_1^2 + \frac{M_{R_1} \left(M_{R_3} R_2^2 + M_{R_2} R_3^2 \right)}{\sin^2 \theta_1} \right]}$$

$$(Eq.\ 15\,a - d)$$

The off-diagonal elements of the matrix $\mathbf{\Gamma}_{rigid}$ are not used in Eq. (4.14) because we demand that the rotational quantum number K is conserved in our models. M_{R_i} is the inverse of the reduced mass associated with the Jacobi coordinate R_i

$$M_{R_1} = \frac{m_{CH_4}}{m_{CH_3} m_H}$$
$$M_{R_2} = \frac{2}{m_H}$$

$$M_{R_3} = \frac{m_{H_3}}{m_{H_2} m_H}$$
$$M_{R_4} = \frac{m_{CH_3}}{m_{H_3} m_C}$$

(4.15)

Finally, the coordinate ranges are

$$0 \leqslant R_1 \leqslant +\infty$$

$$-\pi \leqslant \theta_1 \leqslant \pi$$

(4.16)

The angle θ_1 varies over the full circle rather than the half circle. This unusual range is adopted because the corresponding azimuthal angle φ_1 is kept fixed here.

4.3.2   The MCTDH method

The MCTDH method is a powerful algorithm designed to solve the quantum molecular dynamics equations of motion for large systems. But MCTDH is also very useful for solving low-dimensional systems when large primitive basis sets (DVR-grids) are required. Moreover, it is convenient to use the Heidelberg MCTDH package even for small systems, because the package provides the user with a large number of analysis tools and visualization routines. We just define here the procedures and the tools that we used for this work. More details concerning this method are given in Refs. [63, 64, 65, 66].

4.3.2.1 MCTDH Algorithm

In MCTDH, the wave function is expanded as a linear combination of Hartree products of single-particle functions (SPFs) :

$$\psi\left(Q_1, \ldots Q_f, t\right) = \sum_{j_1=1}^{n_1} \ldots \sum_{j_f=1}^{n_f} A_{j_1\ldots j_f}(t) \prod_{\kappa=1}^{f} \varphi_{j_\kappa}^{(\kappa)}\left(Q_\kappa, t\right) \qquad (4.17)$$

where f is the number of degrees of freedom of the system, $Q_1, \ldots, Q_f$ denote the nuclear coordinates, $A_{j_1}, \ldots, A_{j_f}$ the MCTDH expansion coefficients and $\varphi\left(Q_\kappa, t\right)$ the n_κ SPFs associated with the degree of freedom κ. The multi-configurational nature of Eq. (4.17) results in a correct description of the correlation between the degrees of freedom provided that the SPF basis set is large enough, or, equivalently, that there is a sufficiently large number of configurations.

The SPFs are represented on a time-independent primitive basis set with N_κ points for the κth degree of freedom :

$$\varphi_{j_\kappa}^{(\kappa)}\left(Q_\kappa, t\right) = \sum_{i_\kappa=1}^{N_\kappa} c_{i_\kappa, j_\kappa}^{(\kappa)}(t)\, \chi_{i_\kappa}^{(\kappa)}\left(Q_\kappa\right). \qquad (4.18)$$

The $\chi_{i_\kappa}^{(\kappa)}\left(Q_\kappa\right)$ are usually chosen as the basis functions associated with a discrete variable representation (DVR) or a Fourier representation. The size of this primitive basis is determined by the physical phase-space spanned by the system. The SPFs can also be taken to describe the motion in more than one degree of freedom, using a technique called mode-combination that is described in detail in Refs.[64, 67]. We use this technique in the 3D and 4D calculations described below.

Before presenting the MCTDH working equations, we simplify the notation by etablishing the composite index J and the configurations Φ_J : $A_J = A_{j_1\ldots j_f}$ and $\Phi_J = \prod_{\kappa=1}^{f} \varphi_{j_\kappa}^{(\kappa)}$. We also introduce the single-hole functions $\Psi_l^{(\kappa)}$, which are defined as the linear combination of Hartree products of $(f-1)$ SPFs that do not contain a SPF for the coordinate Q_κ

$$\Psi_l^{(\kappa)} = \sum_{J}^{\kappa} A_{J_l^\kappa} \varphi_{j_1}^{(1)} \ldots \varphi_{j_{\kappa-1}}^{(\kappa-1)} \varphi_{j_{\kappa+1}}^{(\kappa+1)} \ldots \varphi_{j_f}^{(f)}. \qquad (4.19)$$

Here J_l^κ denotes a composite index J with the κ'th entry set at l, and $\sum_J^\kappa$ is the sum over the indices for all degrees of freedom excluding the κ'th.

The MCTDH equations of motion resulting from the Frenkel-Dirac variational principle can then be written as :

$$i\dot{A}_J = \sum_{J} \left\langle \Phi_J \right| H \left| \Phi_L \right\rangle A_L \qquad (4.20)$$

$$i\dot{\varphi}_j^{(\kappa)} = \sum_{lm} \left(1 - P^{(\kappa)}\right) \left(\rho^{(\kappa)}\right)_{jl}^{-1} \langle H \rangle_{lm}^{(\kappa)} \varphi_m^{(\kappa)} \qquad (4.21)$$

where $P^{(\kappa)}$ denotes the projector on the space spanned by the SPF for the κ'th degree of freedom

$$P^{(\kappa)} = \sum_{j=1}^{n_\kappa} \left| \varphi_j^{(\kappa)} \right\rangle \left\langle \varphi_j^{(\kappa)} \right|. \qquad (4.22)$$

Above, $\langle H \rangle^{(\kappa)}$ and $\rho^{(\kappa)}$ are, respectively, the mean-fields and density matrices that can be obtained from the single-hole functions :

$$\langle H \rangle_{jl}^{(\kappa)} = \left\langle \Psi_j^{(\kappa)} \middle| H \middle| \Psi_l^{(\kappa)} \right\rangle \tag{4.23}$$

$$\rho_{jl}^{(\kappa)} = \left\langle \Psi_j^{(\kappa)} \middle| \Psi_l^{(\kappa)} \right\rangle = \sum_J^{\kappa} A_{J_j^\kappa}^* A_{J_l^\kappa}. \tag{4.24}$$

The populations of the natural orbitals, which are defined as the eigenvalues of the density operator in each degree of freedom (Eq. 4.24), reflect the degree of convergence of the wave function with respect to the size of the time-dependent basis set. In particular, a small value of the lowest natural population indicates that enough SPFs have been used for the single particle to achieve convergence. Equations (4.20) and (4.21) are the MCTDH equations of motion for the simplest choice of constraints [64].

4.3.2.2   Refitting the PES

To solve the equations of motion requires the evaluation of the $\langle \Phi_J | H | \Phi_L \rangle$ Hamiltonian matrix and the $\langle H \rangle$ mean-fields at each time step of the integration. These f and $(f-1)$ dimensional integrals are circumvented if the Hamiltonian is written as a sum of products of single-particle operators :

$$H = \sum_{r=1}^{s} c_r \prod_{\kappa=1}^{f} h_r^{(\kappa)} \tag{4.25}$$

with expansion coefficients c_r. The KEO usually has the required form, but this is not the case for the potential energy operator in the general case, and the potential energy expression as obtained from the GROW method in our specific case (the weight functions in Eq. (4.3) depend on all DOFs). However, an efficient procedure (POTFIT)[68, 69] is available to fit the potential to the desired product form. This method is based on the approximation theorem of Schmidt which defines an efficient scheme to generate a product representation of a given multidimensional function.

When the PES is given on a product grid, $V\left(Q_{i_1}^{(1)}, \ldots, Q_{i_f}^{(f)}\right) \equiv V_{i_1 \ldots i_f}$, the elements of the symmetric positive semi-definite potential density matrices $\varrho^{(\kappa)}$ can be written as

$$\varrho_{jl}^{(\kappa)} = \sum_{i_1=1}^{N_1} \ldots \sum_{i_{\kappa-1}=1}^{N_{\kappa-1}} \sum_{i_{\kappa+1}=1}^{N_{\kappa+1}} \ldots \sum_{i_f=1}^{N_f} V_{i_1 \ldots i_{\kappa-1} j i_{\kappa+1} \ldots i_f} V_{i_1 \ldots i_{\kappa-1} l i_{\kappa+1} \ldots i_f}. \tag{4.26}$$

The orthonormal eigenvectors $v_j^{(\kappa)}$ and the associated eigenvalues $\lambda_j^{(\kappa)}$ of these matrices are called natural potentials and natural potential populations, respectively. The natural populations are assumed to be in decreasing order, $\lambda_j^{(\kappa)} \geqslant \lambda_{j+1}^{(\kappa)}$. Choosing a set of expansion orders $\{m_\kappa\}$ one may approximate the potential by

$$V^{app}\left(Q_{i_1}^{(1)}, \ldots, Q_{i_f}^{(f)}\right) \approx \sum_{j_1=1}^{m_1} \ldots \sum_{j_f=1}^{m_f} C_{j_1 \ldots j_f} v_{j_1}^{(1)}\left(Q_{i_1}^{(1)}\right) \ldots v_{j_f}^{(f)}\left(Q_{i_f}^{(f)}\right). \tag{4.27}$$

The expansion coefficients $C_{j_1 \ldots j_f}$ are determined by the overlaps between the potential and the natural potentials,

$$C_{j_1\ldots j_f} = \sum_{i_1=1}^{N_1} \cdots \sum_{i_f=1}^{N_f} V_{i_1\ldots i_f} v_{i_1 j_1}^{(1)} \ldots v_{i_f j_f}^{(f)} \tag{4.28}$$

If the expansion orders and the number of grid points are equal, the approximated and the exact potential are identical ($V^{app} \to V$ for $\{m_\kappa\} \to \{N_\kappa\}$), at the grid point.

In order to decrease the number of expansion terms in Eq. (4.27) by a factor of m_κ, we use the contracted expansion function

$$D_{j_1\ldots j_{\kappa-1} j_{\kappa+1}\ldots j_f} \left(Q_{i_\kappa}^{(\kappa)} \right) = \sum_{j_\kappa=1}^{m_\kappa} C_{j_1\ldots j_f} v_{i_\kappa j_\kappa}^{(\kappa)} \tag{4.29}$$

and rewrite the expansion of the approximated potential as

$$
\begin{aligned}
V^{app} \left(Q_{i_1}^{(1)}, \ldots, Q_{i_f}^{(f)} \right) \;=\;& \sum_{j_1=1}^{m_1} \cdots \sum_{j_{\kappa-1}=1}^{m_{\kappa-1}} \sum_{j_{\kappa+1}=1}^{m_{\kappa+1}} \cdots \sum_{j_f=1}^{m_f} v_{j_1}^{(1)} \left(Q_{i_1}^{(1)} \right) \ldots v_{j_{\kappa-1}}^{(\kappa-1)} \left(Q_{i_{\kappa-1}}^{(\kappa-1)} \right) \\
& \times D_{j_1\ldots j_{\kappa-1} j_{\kappa+1}\ldots j_f} \left(Q_{i_\kappa}^{(\kappa)} \right) v_{j_{\kappa+1}}^{(\kappa+1)} \left(Q_{i_{\kappa+1}}^{(\kappa+1)} \right) \ldots v_{j_f}^{(f)} \left(Q_{i_f}^{(f)} \right).
\end{aligned}
\tag{4.30}
$$

The summation in Eq. (4.29) replaces the upper summation limit m_κ with N_κ. This increases the accuracy of the potential approximation without increasing the number of potential expansion coefficients.

Not all regions of the PES are equally relevant for the dynamics. It is possible to define a relevant zone for the POTFIT procedure where the natural potentials are iteratively improved by a multidimensional iteration procedure.

The potential fit accuracy is finally checked by the calculation of the root-mean-square error (RMS) which is defined as

$$\Delta_{rms} = \sqrt{N_{tot}^{-1} \sum_{i_1=1}^{N_1} \cdots \sum_{i_f=1}^{N_f} \left(V_{i_1\ldots i_f} - V_{i_1\ldots i_f}^{app} \right)^2} \tag{4.31}$$

where $N_{tot} = \prod_{\kappa=1}^{f} N_\kappa$. The natural potentials can also be taken to depend on more than one degree of freedom using the same technique of mode-combination that can be employed for the single particle functions used in the expansion of the wave function [64, 67]. Again, this technique is used in our 3D and 4D calculations reported below.

4.3.2.3 Flux analysis

Initial-state selected reaction probabilities can be computed with the aid of a complex adsorbing potential (CAP) located in the product region combined with a flux analysis approach. The MCTDH package contains exclusively monomial CAPs

$$-iW(Q) = -i\eta \left(Q - Q_c \right)^b \Theta \left(Q - Q_c \right) \tag{4.32}$$

where η, b and Q_c denote the strength, the order and the starting point of the CAP, respectively. $\Theta\left(Q - Q_c\right)$ is the Heaviside step function, allowing to switch on the CAP when $Q > Q_c$ ($\Theta = 0$ for $Q \leqslant Q_c$ and $\Theta = 1$ for $Q > Q_c$).

The initial-state selected dissociation probability $P_i\left(E_{Z_i}\right)$ is calculated by applying a flux analysis method using the CAP. The reaction probability is given by:

$$P_i\left(E_{Z_i}\right) = \frac{2}{\pi\left|\Delta E_{Z_i}\right|^2} \mathrm{Re}\left\{\int_0^\infty d\tau g\left(\tau\right)\exp\left(iE_{Z_i}\right)\right\} \tag{4.33}$$

with

$$g\left(\tau\right) = \int_0^\infty dt\left\langle\Psi\left(t\right)\left|W_r\right|\Psi\left(t+\tau\right)\right\rangle \tag{4.34}$$

where ΔE_{Z_i} denotes the energy distribution of the initial wave packet for translation normal to the surface. The value of ΔE_{Z_i} determines the energy range for which the reaction probability can be computed in one single calculation. The working equations relate the time evolution of the initial wave packet, via the dissociation arrangement channel CAP, W_r, to the desired initial-state selected reaction probabilities.

4.3.3   Models

We define here the initial wave functions and the Hamiltonian operators used in the 2D-, 3D- and 4D-model calculations, reported below.

4.3.3.1   2D (Z, R_1)

The initial wave packet (WP) is located in the asymptotic region (Fig. 4.5). To describe the motion towards the surface we use a Gaussian function $\chi_0\left(Z\right)$ along the scattering coordinate Z defined as

$$\chi_0\left(Z\right) = \left(\sqrt{2\pi}\sigma\right)^{-1/2}\exp\left[-\left(\frac{Z - Z_0}{2\sigma}\right)^2\right]\exp\left[-ip_{Z_0}\left(Z - Z_0\right)\right] \tag{4.35}$$

where σ, p_{Z_0} and Z_0 are the width, the initial average momentum and the initial average position, respectively.

The wave function describing the initial vibrational state v_0 of the molecule is taken as the corresponding eigenfunction of the one dimensional vibrational Hamiltonian

$$\hat{H}_{asy}^{2D} = -\frac{M_{R_1}}{2}\frac{\partial^2}{\partial R_1^2} + V_M\left(R_1\right) \tag{4.36}$$

where $V_M\left(R_1\right)$ is the 1D gas phase potential.
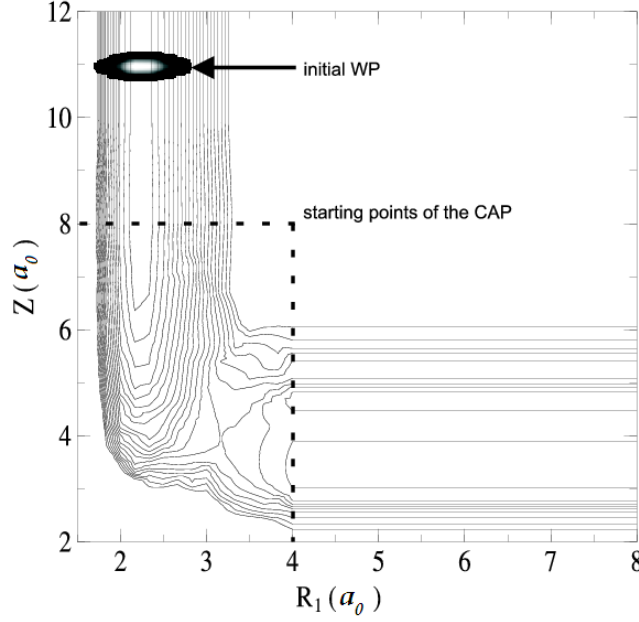
Figure 4.5: 2D (Z, R_1) PES minimized on θ_1 and β.

The initial wave function finally reads

$$\Psi\left(Z, R_1; t = 0\right) = \chi_0\left(Z\right)\varphi_{v_0}\left(R_1\right) \tag{4.37}$$

where $\varphi_{v_0}\left(R_1\right)$ defines the initial reactive CH-stretch vibrational state, corresponding to the quantum number v_0.

The primitive grid used for this calculation is represented by different kinds of DVR/FBR representations. A FFT [70] and a sine DVR [71] are used for the Z and R_1 coordinates, respectively. The sine DVR representation is adapted to the vibrational and dissociative DOF and uses the particle-in-a-box eigenfunctions as a basis. Moreover, the generation of the vibrational eigenfunctions, that we use to get the initial wave function corresponding to the v_0 state, requires the use of a DVR basis for the vibrational DOF as the MCTDH program generates the eigenfunctions by diagonalizing the operator represented as a real matrix.

The KEO used for the 2D calculations is straightforward and does not require the method developed in Section (4.3.1), although it could also be derived by applying constraints as discussed above:

$$\hat{H}^{2D} = -\frac{1}{2m_{CH_4}}\frac{\partial^2}{\partial Z^2} - \frac{M_{R_1}}{2}\frac{\partial^2}{\partial R_1^2} + V\left(Z, R_1\right). \tag{4.38}$$

Here, $V\left(Z, R_1\right)$ is the 2D PES. This potential was first interpolated from the 4931 DFT points (Section 4.2) on a 4D grid $(Z, R_1, \theta_1, \beta)$ with a regular step of 1 degree with respect to θ_1 and β, and then minimized with respect to these two angles. The resulting PES (Fig. 4.5) depends explicitly on Z and R_1, but takes into account the angular and bend vibrational DOFs in an adiabatic picture. The parameters used to refit the PES in the product form are reported in Table 4.1.

	2D	3D	4D
Natural potentials			
m_Z	contr	36	42
m_{R_1}	15		
m_{R_1,θ_1}		contr	contr
m_β			30
Relevant region for iterative optimization procedure			
V (eV)	< 3	Same	Same
Z (a_0)	$2 < Z < 8$	Same	Same
R_1 (a_0)	< 4	Same	Same
Potfit accuracy			
RMS error on all grid points (meV)	6.26	17.81	18.36
RMS error on relevant grid points (meV)	0.75	7.86	7.24

Table 4.1: POTFIT parameters. In the table m_ρ is the number of natural potentials used for the degree (degrees) of freedom ρ and 'contr' indicates that the contraction technique is used.

4.3.3.2   3D (Z, R_1, θ_1)

In this model, we take into account two vibrational degrees of freedom: R_1 and θ_1, the bending angle between $\vec{R}_1$ and the symmetry axis of the frozen umbrella. The initial wave function describing the initial vibrational state is now obtained from the diagonalization of the 2D vibrational Hamiltonian:

$$\hat{H}_{asy}^{3D} = -\frac{M_{R_1}}{2}\frac{\partial^2}{\partial R_1^2} - \frac{1}{2}\left(\frac{M_{R_3}M_{R_4}}{M_{R_4}R_3^2 + M_{R_3}R_4^2} + \frac{M_{R_1}}{R_1^2}\right)\frac{\partial^2}{\partial\theta_1^2} + V_M(R_1,\theta_1). \quad (4.39)$$

Here, $V_M(R_1,\theta_1)$ is the two dimensional gas phase potential.
To achieve this, one has to use mode combination in order to work with 2D SPFs [64]. The eigenfunction of this Hamiltonian corresponding to the selected initial vibrational state v_0 is then used as the initial vibrational wave function $\varphi_{v_0}(R_1,\theta_1)$. The initial wave function now reads

$$\Psi(Z, R_1, \theta_1; t=0) = \chi_0(Z)\varphi_{v_0}(R_1,\theta_1) \quad (4.40)$$

where $\chi_0(Z)$ is the same as for the 2D model.

A FFT and two sine DVR representations are used for Z, R_1 and θ_1, respectively.

Since θ_1 is coupled to the other angles of the system, we now need to apply a rigidly constrained reduction of the full-D KEO (Section 4.3.1.2), yielding

$$\hat{H}^{3D} = -\frac{1}{2m_{CH_4}}\frac{\partial^2}{\partial Z^2} - \frac{M_{R_1}}{2}\frac{\partial^2}{\partial R_1^2} - \frac{1}{2}\left(\frac{M_{R_3}M_{R_4}}{M_{R_4}R_3^2 + M_{R_3}R_4^2} + \frac{M_{R_1}}{R_1^2}\right)\frac{\partial^2}{\partial\theta_1^2} + V(Z, R_1, \theta_1).$$
$$(4.41)$$

Here, $V(Z, R_1, \theta_1)$ is the 3D PES that was first interpolated on a 4D grid $(Z, R_1, \theta_1, \beta)$ with a regular step of 1 degree with respect to β, and then minimized with respect to this angle. The resulting PES depends explicitly on Z, R_1 and θ_1, but takes β into account in an adiabatic picture.

4.3.3.3 4D $(Z, R_1, \theta_1, \beta)$

The initial wave function now also includes the description of the initial rotational state. The first change with respect to the 3D model consists of adding a term corresponding to the initial rotational energy to the gas phase molecular Hamiltonian:

$$
\begin{aligned}
\hat{H}_{asy}^{4D} &= -\frac{M_{R_1}}{2}\frac{\partial^2}{\partial R_1^2} - \frac{1}{2}\left(\frac{M_{R_3}M_{R_4}}{M_{R_4}R_3^2 + M_{R_3}R_4^2} + \frac{M_{R_1}}{R_1^2}\right)\frac{\partial^2}{\partial\theta_1^2} + V_M(R_1, \theta_1) \\
&\quad + \frac{1}{4}\left(\Gamma_{rigid}^{(xx)} + \Gamma_{rigid}^{(yy)}\right)[J(J+1) - K^2] + \frac{1}{2}\Gamma_{rigid}^{(zz)}K^2
\end{aligned}
\tag{4.42}
$$

where the last two terms represent the initial rotational energy corresponding to our model.

The initial wave function describing the initial rotational state is the Wigner d-function, $d_{M_0,K_0}^{J_0}$:

$$
d_{M_0,K_0}^{J_0}(\beta) = \xi_{M_0,K_0}\sqrt{\frac{l!(l+m+n)!}{(l+m)!(l+n)!}}\left(\sin\frac{\beta}{2}\right)^m\left(\cos\frac{\beta}{2}\right)^n P_l^{(m,n)}(\cos\beta) \tag{4.43}
$$

where

$$
m = |M_0 - K_0| \qquad n = |M_0 + K_0| \qquad l = J - \frac{m+n}{2}
$$

and

$$
\xi_{M_0,K_0} = \begin{cases} 1 & \text{if } K_0 \geqslant M_0 \\ (-1)^{K_0 - M_0} & \text{if } K_0 < M_0 \end{cases}
$$

and $P_l^{(m,n)}(\cos\beta)$ is a Jacobi polynomial.

The initial wave function used for the 4D model finally reads:

$$
\Psi(Z, R_1, \theta_1, \beta; t = 0) = \chi_0(Z)\,\varphi_{v_0, J_0, K_0}(R_1, \theta_1)\,d_{M_0,K_0}^{J_0}(\beta) \tag{4.44}
$$

As for the 3D model, a FFT and two sine DVR representations are used for Z, R_1 and θ_1, respectively. A Legendre DVR is employed for the angular degree of freedom, β.

The 4D Hamiltonian is given by

$$
\begin{aligned}
\hat{H}^{4D} &= -\frac{1}{2m_{CH_4}}\frac{\partial^2}{\partial Z^2} - \frac{M_{R_1}}{2}\frac{\partial^2}{\partial R_1^2} - \frac{1}{2}\left(\frac{M_{R_3}M_{R_4}}{M_{R_4}R_3^2 + M_{R_3}R_4^2} + \frac{M_{R_1}}{R_1^2}\right)\frac{\partial^2}{\partial\theta_1^2} \\
&\quad + \frac{1}{2}\left(\Gamma_{rigid}^{(xx)}\hat{J}_x^2 + \Gamma_{rigid}^{(yy)}\hat{J}_y^2 + \Gamma_{rigid}^{(zz)}\hat{J}_z^2\right) + V(Z, R_1, \theta_1, \beta)
\end{aligned}
\tag{4.45}
$$

where the expressions of the rotation coupling matrix elements and the values of the fixed parameters are given in Part. (4.3.1.2). We use directly the 4D PES $V(Z, R_1, \theta_1, \beta)$ described earlier for this model.

4.4   Results

4.4.1   Numerical details

The potential fit parameters (natural potential, relevant region and RMS error) are reported in Table 4.1. The potential fit accuracy is checked by the calculation of the RMS error. For the 2D case, an accuracy of a few meV is reached using only 15 natural potentials in R_1, the RMS error being even lower than 1 meV in the relevant zone. For the 3D case, the RMS error is in the order of a few meV with 36 natural potentials in Z in the relevant zone. For the 4D case, 42 natural potentials in Z and 30 in β are necessary to get the same order of accuracy. From these error estimates, we can assume that the refitting of the PES does not introduce major problems and that the refitted potentials are accurate enough to be used in the wave packet simulations.

The parameters of the WP propagations (propagation time, primitive grid, CAP and SPF) are collected in Tables 4.2, 4.3 and 4.4. It is generally assumed that convergence can be achieved if the natural orbital population is less than 10^{-3}. As was the case for the potential fit procedure, the 2D WP propagations converge quickly and do not request a large computational effort. The lowest natural population over time are smaller than 10^{-5} using only 14 to 17 SPFs in each mode for $v_0 = 0$ to 3. For the more costly 3D and 4D cases, we used enough SPFs in each propagation (for each set of v_0, J, M, K) to get the lowest natural population smaller than 10^{-4}. Thus, we assume that the calculations are converged with respect to the MCTDH parameters.

		Time		
		$t_{final} = 300$ to 500 fs		
		$\Delta t = 1$ fs		
		Grid		
		N_q	q_i (a_0)	q_f (a_0)
Z	fft	324	1	12
R_1	sin	40	1.5	8
		CAP		
	q_i (a_0)	η	b	t_a (fs)
Z	8	0.0005761	3	80
R_1	4	0.0009448	3	0
	SPF ($v_0 = 0$ case)			
	N_{SPF}		lowest $\rho^{(q)}$	
Z	14		7×10^{-6}	
R_1	14		7×10^{-6}	

Table 4.2: 2D propagation parameters. The number of SPFs needed to reach the desired level of convergence depends on the vibrational state under investigation. For $v_0 = 3$, only 15 SPFs in each degree of freedom are necessary to achieve a lowest natural orbital population $< 10^{-5}$.

Time				
$t_{final} = 300$ to 350 fs				
$\Delta t = 1$ fs				
Grid				
		N_q	q_i (a_0)	q_f (a_0)
Z	fft	324	1	12
R_1	sin	40	1.5	8
θ_1	sin	30	$-\pi/2$	$\pi/2$
CAP				
	q_i (a_0)	η	b	t_a (fs)
Z	8	0.0005761	3	80
R_1	4	0.0009448	3	0
SPF $(v_0 = 0$ case$)$				
	N_{SPF}		lowest $\rho^{(q)}$	
Z	19		8×10^{-5}	
R_1, θ_1	19		8×10^{-5}	

Table 4.3: 3D propagation parameters. For $v_0 = 4$, 24 SPFs in each mode are used to achieve the same order of accuracy.

Time				
$t_{final} = 300$ to 350 fs				
$\Delta t = 1$ fs				
Grid				
		N_q	q_i (a_0)	q_f (a_0)
Z	fft	324	1	12
R_1	sin	40	1.5	8
θ_1	sin	30	$-\pi/2$	$\pi/2$
β	Leg	37	0	π
CAP				
	q_i (a_0)	η	b	t_a (fs)
Z	8	0.0005761	3	80
R_1	4	0.0009448	3	0
SPF $(v_0 = 0$ case$)$				
	N_{SPF}		lowest $\rho^{(q)}$	
Z	35		8×10^{-5}	
R_1, θ_1	35		8×10^{-5}	
β	30		8×10^{-5}	

Table 4.4: 4D propagation parameters.
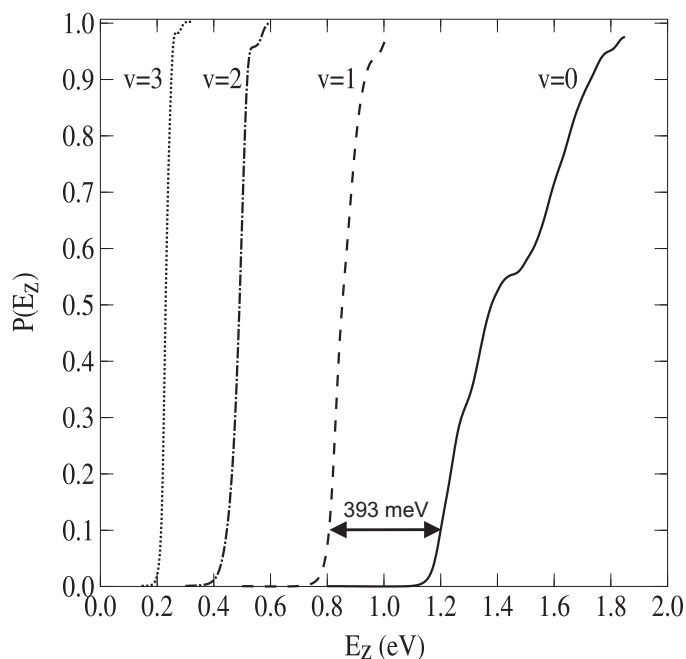
Figure 4.6: 2D model dissociation probabilities. $v_0 = 0$ to 3.

4.4.2   2D (Z, R_1) model

The CH$_4$ dissociation probabilities obtained with the 2D model for $v_0 = 0$ to 3 (corresponding to the R_1 stretching mode only) are plotted as a function of E_{Z_i} in Fig. 4.6. Reaction probabilities increase quickly from 0 to 1 for excited states, being almost step functions, although the reaction probability curve contains some oscillatory structure for the ground state. The vibrational efficacy, η_{vib}^ν is defined as:

$$\eta_{vib}^\nu = \frac{\Delta E_{trans}}{\Delta E_\nu}. \tag{4.46}$$

Here, ΔE_{trans} is the amount of translational energy required to attain the same increase in reactivity as observed for the addition of ΔE_ν of vibrational energy by excitation to the vibrational state ν. The vibrational efficacies measured at $P(E_{z_i}) = 0.1$ are presented in Table 4.5. The vibrational efficacy is bigger than 1 for $v_0 = 1$ ($\eta_{vib}^{1\nu_{R_1}} = 1.07$) and $v_0 = 2$ ($\eta_{vib}^{2\nu_{R_1}} = 1.04$), which means that E_{vib} is more efficient than E_{trans} to promote the reaction for these two vibrational states. The efficacy decreases with respect to the initial vibrational excitation and is lower than 1 for $v_0 = 3$ ($\eta_{vib}^{3\nu_{R_1}} = 0.93$). These results are qualitatively consistent with experiments that provide a value bigger than 1 for the antisymmetric stretch ν_3 on Ni(111): $\eta_{vib}^{1\nu_3} = 1.25$, and a decrease of the vibrational efficacy with respect to the vibrational excitation on Ni(100): $\eta_{vib}^{1\nu_3} = 1$ and $\eta_{vib}^{2\nu_3} = 0.8$.

4.4.3 3D (Z, R_1, θ_1) model

In the following, we denote with v_s and v_b the quantum numbers corresponding to the stretching mode (R_1) and to the bending mode (θ_1). We investigate with this model the five lowest energy vibrational states $v_0 = 0$ to 4 including the ground state $(v_s = 0, v_b = 0)$, the three first excited states of the bending vibration $(v_s = 0, v_b = 1$ to $3)$, and the first excited state of the stretching vibration $(v_s = 1, v_b = 0)$. Information about these vibrational states, including vibrational efficacies, is given in Table 4.6. Note that even though our stretching and bending modes are not CH_4 normal modes, their vibrational energies are very close to the ν_3 and ν_4 ones.
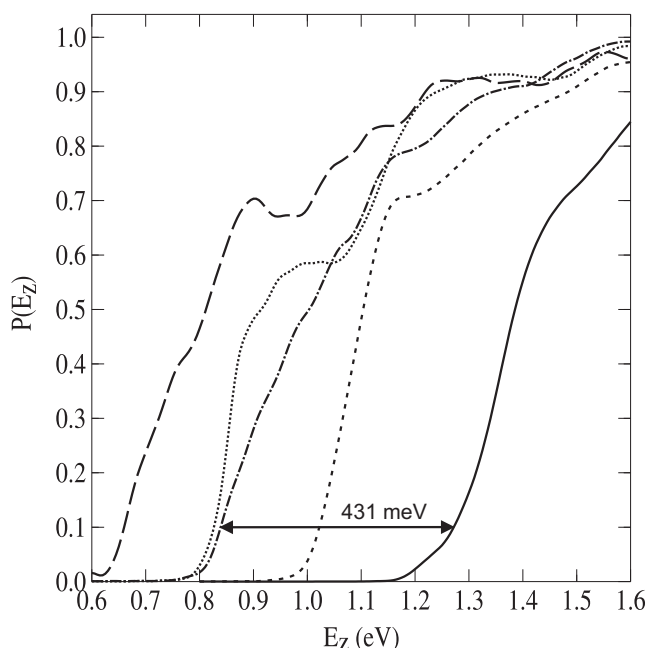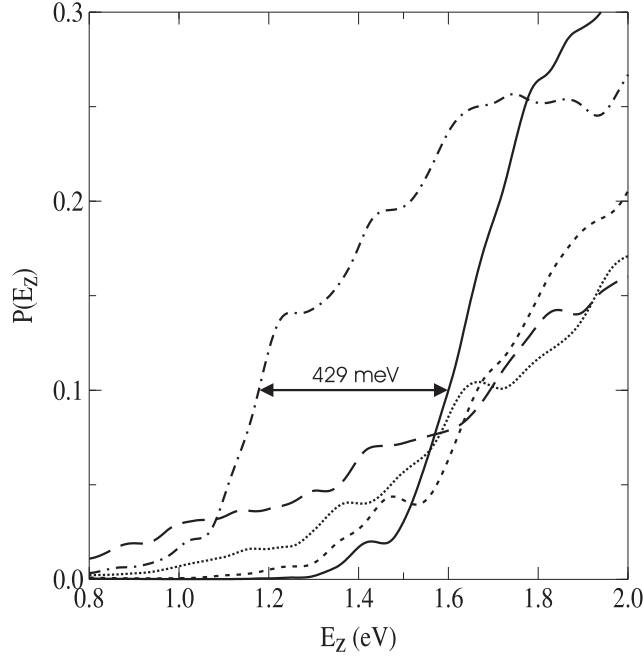

Figure 4.7: 3D model dissociation probabilities. $v_0 = 0$ to 4: $v_0 = 0$ (solid), $v_0 = 1$ (small dash), $v_0 = 2$ (dot), $v_0 = 3$ (dot+dash), $v_0 = 4$ (long dash).

The CH_4 dissociation probabilities, computed for $v_0 = 0$ to 4 are plotted as a function of E_{Z_i} in Fig. 4.7. The dissociation probabilities increase with respect to the initial vibrational energy. The curves for $v_0 = 2$ $(v_s = 0, v_b = 2)$ and $v_0 = 3$ $(v_s = 1, v_b = 0)$ are almost superimposed. These two vibrational states are almost isoenergetic in our calculations (Table 4.6). Experiments show that pre-exciting the stretching vibrational excitations should be more efficient to promote reaction than pre-exciting the bending modes [12]. In the 3D model, the stretching and bending modes seem to contribute equally to the reaction. In other words, the reactivity of this model depends only on the amount of energy put in vibration and not on whether the energy is in the stretching mode or in the bending mode.

The value obtained for the vibrational efficacy of the stretching mode is increased relative to the 2D model one. We find here $\eta_{vib}^{1\nu_{R_1}} = 1.18$ for $v_0 = 3$

v_0	ΔE_{vib} (meV)	ΔE_{trans} (meV)	η_{vib}
1	369	393	1.065
2	723	753	1.041
3	1061	987	0.930

Table 4.5: Vibrational efficacies at $P(E_{Z_i}) = 0.1$. $\Delta E(v_0 = i)$ means $E(v_0 = i) - E(v_0 = 0)$.

v_0	$v_s + v_b$	E_{vib} (meV)	ΔE_{vib} (meV)	ΔE_{trans} (meV)	η_{vib}
0	$0 + 0$	294			
1	$0 + 1$	466	172	250	1.45
2	$0 + 2$	639	345	445	1.29
3	$1 + 0$	670	376	433	1.15
4	$0 + 3$	814	520	612	1.18

Table 4.6: Vibrational efficacies at $P(E_{Z_i}) = 0.1$. $\Delta E(v_0 = i)$ means $E(v_0 = i) - E(v_0 = 0)$. The results are for the 3D model.

($v_s = 1$, $v_b = 0$) against 1.07 for the corresponding vibrational state in the 2D model. The 3D description improves the vibrational efficacy of the stretching mode with regards to the experimental value of the antisymmetric stretching $1\nu_3$ state, where $\eta_{vib}^{1\nu_3} = 1.25$.

4.4.4   4D $(Z, R_1, \theta_1, \beta)$ model

This model also allows the study of the dependence of the reaction probability on the initial ro-vibrational state. We use the flat surface approximation to study the effect of the M_0-dependent orientation (M_0 is conserved during the dynamics) and a similar approximation to treat the quantum number K_0 (the PES in our 4D model does not depend on the angles conjugate to these angular momenta). With this model, we start a calculation with a set of quantum numbers v_0, J_0, M_0 and K_0, where the projections of the total angular momentum on the BF z-axis and on the SF Z-axis are conserved. We present results on the vibrational efficacy of different vibrational states and on the effect of the initial rotational state separately. First, we give results for $J_0 = 0$, $M_0 = 0$, $K_0 = 0$ and varying v_0, and then for $v_0 = 0$ and varying J_0, M_0 and K_0.

Selected vibrational states

Reaction probabilities for $J_0 = 0$, $M_0 = 0$, $K_0 = 0$ and varying v_0 are presented in Fig. 4.8. The vibrational state definition is the same as in the 3D model, but the CH_4 polar rotational motion is now included in the dynamics.

This reaction probabilities are smaller than the corresponding 3D reaction probabilities since all initial polar orientations (i.e., also the less reactive one) of the molecule are now considered. We still observe a dramatic increase of the dissocia-
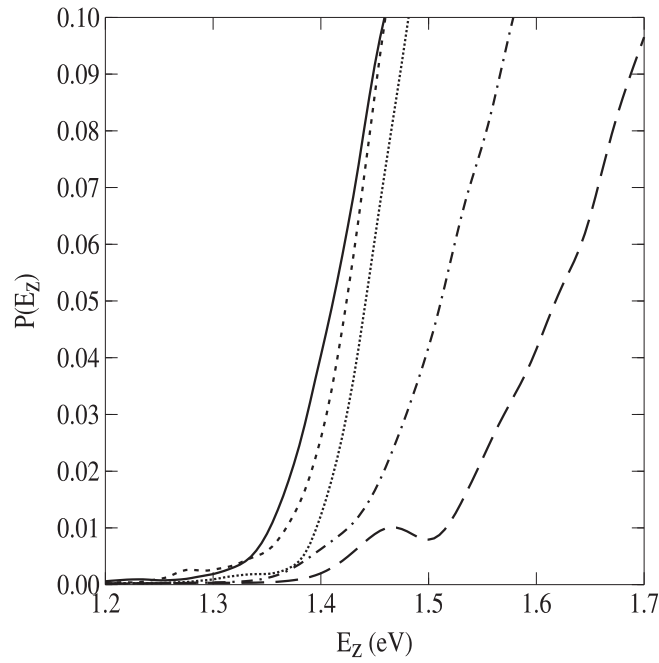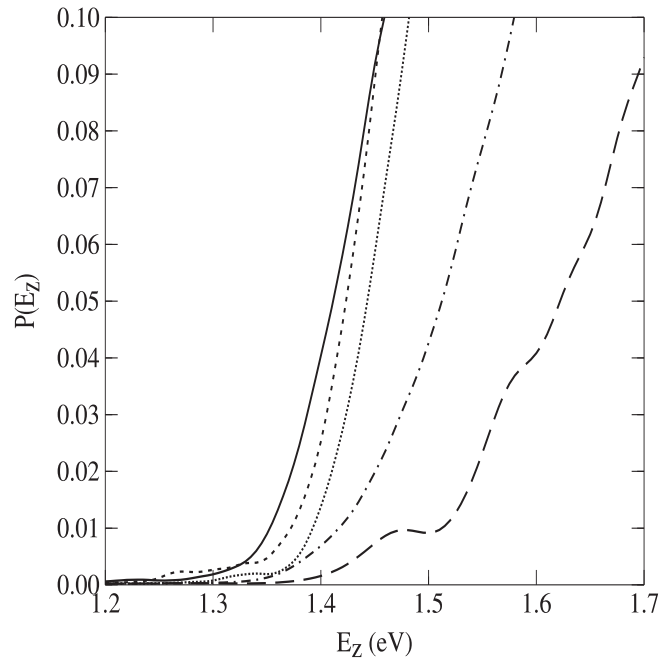
Figure 4.8: 4D model dissociation probabilities. $v_0 = 0$ to 4, $J_0 = 0$: $v_0 = 0$ (solid), $v_0 = 1$ (small dash), $v_0 = 2$ (dot), $v_0 = 3$ (dot+dash), $v_0 = 4$ (long dash).

tion probability with respect to the stretching excitation at low incident energies for $v_0 = 3$ ($v_s = 1$, $v_b = 0$). The vibrational efficacy is almost conserved from the 3D model, we find here $\eta_{vib}^{1\nu_{R_1}} = 1.17$. The explicit description of the rotational motion in the dynamics seems to have no effect on the stretching mode efficacy, but does affect the reactivity of the bend excited states. The thresholds still decreases with increasing initial vibrational excitation, but the reaction probabilities now increase more slowly with vibrational energy than with translational energy. At low energies, the 4D model does not yet reproduce the experimental result that pre-exciting the molecule with one quantum of (ν_3) stretch promotes reaction more than pre-exciting it with 3 bending (ν_4) quanta, presumably because the description of the ν_3 and ν_4 modes is too rudimentary with our low-dimensional model. At higher energies, the description of the effect of pre-exciting the bending mode on reaction is even qualitatively incorrect. However at intermediate energies the model now correctly describes the experimental finding that the $1\nu_3$ state is more reactive than the $3\nu_4$ state [12]. Our results suggests that rotation plays a key role in the vibrational mode selectivity, since it affects the efficacies of stretching and bending modes differently. This result is in good agreement with the 3D vibrating rotor model of Xiang et al. [20] in which the dissociation probability is strongly correlated to the initial rotational orientation of the molecule.

Selected rotational states

In our model, the CH_4 molecule is treated as a three dimensional rotor, not a pseudodiatomic rotor. Thus, we can study rigorously the molecular orientational effects. The 3D rotor has three quantum numbers (J, M, K). J is the angular

momentum of the molecule, M its projection on the SF Z-axis and K its projection on the BF z-axis. Here, the molecular axis is parallel to the symmetry axis of the frozen umbrella, pointing toward the opposite direction to the H-atoms.
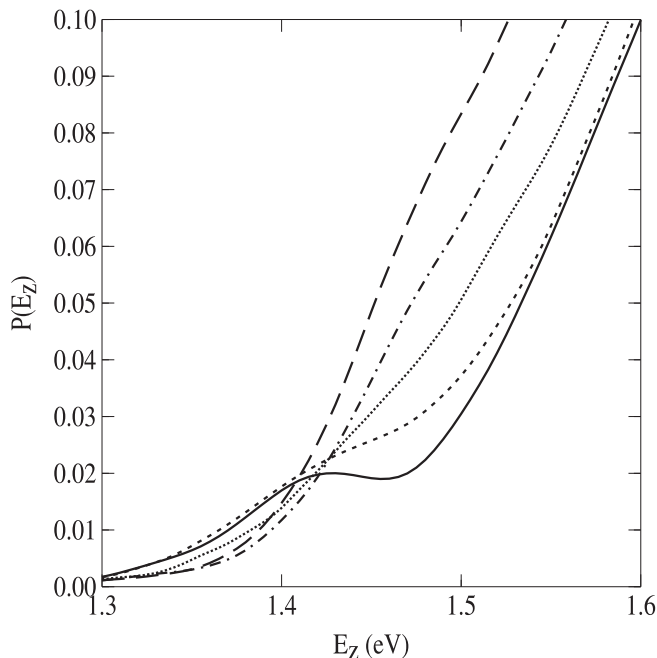
Figure 4.9: 4D model dissociation probabilities. $v_0 = 0$, $J_0 = 0$ to 4, degeneracy averaged over M, $K = 0$: $J_0 = 0$ (solid), $J_0 = 1$ (small dash), $J_0 = 2$ (dot), $J_0 = 3$ (dot+dash), $J_0 = 4$ (long dash).

The reaction probabilities for $J = 0$ to 4, $K = 0$, with degeneracy averaging over M are shown in Fig. 4.9. All J values lead almost to the same reactivity for small energies. This is consistent with the experimental results for $1\nu_3$ $CH_4/Ni(100)$ for E_{Z_i} between 8.9 kJ/mol and 49 kJ/mol showing that the reaction probabilities are almost independent of J [14, 7]. The reaction probabilities intersect at $E_{Z_i} = 1.42$ eV, which is almost equal to the saddle-point energy of our potential, and then separate from each over. For higher energies the probability of dissociation increases slowly with J.

Fig. 4.10 represents reaction probabilities with the CH_4 molecule in the initial rotational level $J = 4$, $K = 0$, with M varying from 0 to 4. The reaction probabilities still increase with translational energy. The dissociation probability decreases with M increasing from 0 to 4, making the helicopter motion $(M = J)$ less efficient than the cart wheel motion $(M = 0)$ for promoting the reaction, as previously found by Xiang et al. [20]. This is not really surprising because in the MEP for dissociation the molecule is not parallel to the surface in the present case. At the transition state, the symmetry axis of the umbrella and the SF Z-axis make an angle of 160°. Therefore the lowest energy path does not favor the parallel approach, but a tilted approach.

Figure 4.10: 4D model dissociation probabilities. $v_0 = 0$, $J_0 = 4$, $M = 0$ to 4, $K = 0$: $M = 0$ (solid), $M = 1$ (small dash), $M = 2$ (dot), $M = 3$ (dot+dash), $M = 4$ (long dash).

Figure 4.11: 4D model dissociation probabilities. $v_0 = 0$, $J_0 = 4$, $K = 0$ to 4, $M = 0$: $K = 0$ (solid), $K = 1$ (small dash), $K = 2$ (dot), $K = 3$ (dot+dash), $K = 4$ (long dash).

Finally, reaction probabilities for $J = 4$, $M = 0$ and K varying from 0 to 4 are

shown in Fig. 4.11. We obtain a similar behaviour in the K dependence of the reaction probability as seen for the M dependence for $K = 0$. Indeed, CH$_4$ is only slightly deformed from C$_{3v}$ at the transition state. Thus it reacts approximately as a symmetric rotor.

4.5 Conclusion

In this study, we presented quantum dynamics calculations using a full-dimensional PES for CH$_4$/Ni(111) that was obtained with DFT using the RPBE functional. We used the MCTDH method to compute dissociative chemisorption of methane at the atop site with 2D, 3D and 4D models.

Our main results are the following: (i) According to the experiments, the stretching mode is efficient at promoting the dissociation. Whereas the vibrational efficacies obtained with the 2D model are too small compared to the experimental results, they are improved by the inclusion of a bending mode. In addition, the vibrational efficacies decrease with respect to the initial vibrational excitation. (ii) The 3D model improves the vibrational efficacy of the stretching mode. However dissociation probability appears to be an increasing function of the initial vibrational energy whatever the vibrational mode excited. The experimental result, that 1 quantum of stretch (ν_3) is more effective for promoting dissociation than 3 quanta of bend (ν_4) whereas the latter state contains more energy, is not yet reproduced. (iii) At intermediate collision energies (1.1-1.4 eV), the difference in efficacies of the stretching and the bending modes is correctly described in the 4D model, where the polar orientation of the molecule is explicitly described. This result shows that the polar rotation plays a key role in the mode selective behavior of the reaction. However, our description of the vibrational modes is still too rudimentary and the effect of pre-exciting the bending mode on reaction remains qualitatively incorrect at higher energies. (iv) For small energies, the reactivity is almost independent of the total angular momentum J. For $E_{Z_i} > 1.42$ eV (almost our SP energy), the reaction probability is an increasing function of J. The cartwheel motion of the umbrella symmetry axis ($M = 0$) is more efficient at promoting reaction than its helicopter motion ($M = J$).

For better agreement with experiment, the dynamical model should include more and possibly all molecular vibrations. It may also be necessary to include the additional rotational and translational degrees of freedom. The global theory used in this work can be used to derive Hamiltonians of higher dimensionality, to achieve this purpose.

Bibliography

[1] J. R. Rostrup-Nielsen, *Catalysis : Science and Technology*, volume 5 (Springer, Berlin, 1984).

[2] M. B. Lee, Q. Y. Yang, and S. T. Ceyer, J. Chem. Phys. **87**, 2724 (1987).

[3] P. M. Holmblad, J. Wambach, and I. Chorkendorff, J. Chem. Phys. **102**, 8255 (1995).

[4] A. C. Luntz, J. Chem. Phys. **102**, 8264 (1995).

[5] J. H. Larsen and I. Chorkendorff, Surf. Sci. Rep. **35**, 163 (1999).

[6] L. B. F. Juurlink, P. R. McCabe, R. R. Smith, C. L. DiCologero, and A. L. Utz, Phys. Rev. Lett. **83**, 868 (1999).

[7] L. B. F. Juurlink, R. R. Smith, and A. L. Utz, Faraday Discuss. **117**, 147 (2000).

[8] M. P. Schmid, P. Maroni, R. D. Beck, and T. R. Rizzo, J. Chem. Phys. **117**, 8603 (2002).

[9] R. D. Beck, P. Maroni, D. C. Papageorgopoulos, T. T. Dang, M. P. Schmid, and T. R. Rizzo, Science **302**, 98 (2003).

[10] A. C. Luntz, Science **302**, 70 (2003).

[11] R. R. Smith, D. R. Killelea, D. F. DelSesto, and A. L. Utz, Science **304**, 992 (2004).

[12] L. B. F. Juurlink, R. R. Smith, D. R. Killelea, and A. L. Utz, Phys. Rev. Lett. **94**, 208303 (2005).

[13] P. Maroni, D. C. Papageorgopoulos, M. Sacchi, T. T. Dang, R. D. Beck, and T. R. Rizzo, Phys. Rev. Lett. **94**, 246104 (2005).

[14] L. Juurlink, D. Killelea, and A. Utz, Prog. Surf. Sci. **84**, 69 (2009).

[15] A. Luntz and J. Harris, Surf. Sci. **258**, 397 (1991).

[16] A. P. J. Jansen and H. Burghgraef, Surf. Sci. **344**, 149 (1995).

[17] M.-N. Carré and B. Jackson, J. Chem. Phys. **108**, 3722 (1998).

[18] S. Nave and B. Jackson, Phys. Rev. Lett. **98**, 173003 (2007).

[19] S. Nave and B. Jackson, J. Chem. Phys. **127**, 224702 (2007).

[20] Y. Xiang, J. Z. H. Zhang, and D. Y. Wang, J. Chem. Phys. **117**, 7698 (2002).

[21] Y. Xiang and J. Z. H. Zhang, J. Chem. Phys. **118**, 8954 (2003).

[22] C. T. Rettner, H. E. Pfnür, and D. J. Auerbach, Phys. Rev. Lett. **54**, 2716 (1985).

[23] A. C. Luntz and D. S. Bethune, J. Chem. Phys. **90**, 1274 (1989).

[24] T.-C. Lo and G. Ehrlich, Surf. Sci. **179**, L19 (1987).

[25] H. Burghgraef, A. P. J. Jansen, and R. A. van Santen, J. Chem. Phys. **98**, 8810 (1993).

[26] H. Burghgraef, A. P. J. Jansen, and R. A. van Santen, Surf. Sci. **324**, 345 (1995).

[27] J. H. McCreery and J. George Wolken, J. Chem. Phys. **67**, 2551 (1977).

[28] J. H. McCreery and J. George Wolken, J. Chem. Phys. **64**, 2845 (1976).

[29] J. H. McCreery and J. George Wolken, J. Chem. Phys. **63**, 4072 (1975).

[30] H. Yang and J. L. Whitten, Surf. Sci. **255**, 193 (1991).

[31] H. Yang and J. L. Whitten, J. Chem. Phys. **96**, 5529 (1992).

[32] S. Nave and B. Jackson, J. Chem. Phys. **130**, 054701 (2009).

[33] A. K. Tiwari, S. Nave, and B. Jackson, Phys. Rev. Lett. **103**, 253201 (2009).

[34] A. K. Tiwari, S. Nave, and B. Jackson, J. Chem. Phys. **132**, 134702 (2010).

[35] R. Milot and A. P. J. Jansen, J. Chem. Phys. **109**, 1966 (1998).

[36] J. Ischtwan and M. A. Collins, J. Chem. Phys. **100**, 8080 (1994).

[37] M. J. T. Jordan, K. C. Thompson, and M. A. Collins, J. Chem. Phys. **102**, 5647 (1995).

[38] R. P. A. Bettens and M. A. Collins, J. Chem. Phys. **111**, 816 (1999).

[39] C. Crespos, M. A. Collins, E. Pijper, and G. J. Kroes, J. Chem. Phys. **120**, 2392 (2004).

[40] P. Nieto, E. Pijper, D. Barredo, G. Laurent, R. A. Olsen, E.-J. Baerends, G.-J. Kroes, and D. Farias, Science **312**, 86 (2006).

[41] C. Díaz, J. K. Vincent, G. P. Krishnamohan, R. A. Olsen, G. J. Kroes, K. Honkala, and J. K. Nørskov, Phys. Rev. Lett. **96**, 096102 (2006).

[42] P. Hohenberg and W. Kohn, Phys. Rev. B **136**, 864 (1964).

[43] W. Kohn and L. J. Sham, Phys. Rev. A **140**, 1133 (1965).

[44] B. Hammer, L. B. Hansen, and J. K. Nørskov, Phys. Rev. B **59**, 7413 (1999).

[45] S. R. Bahn and K. W. Jacobsen, Comput. Sci. Eng. **4**, 56 (2002), the DA-CAPO code is freely available at, http://www.camp.dtu.dk/software.

[46] D. R. Lide, *CRC Handbook of Chemistry and Physics* (New York, 2002), 83rd edition.

[47] H. J. Monkhorst and J. D. Pack, Phys. Rev. B **13**, 5188 (1976).

[48] D. J. Chadi and M. L. Cohen, Phys. Rev. B **8**, 5747 (1973).

[49] G. Mills and H. Jónsson, Phys. Rev. Lett. **72**, 1124 (1994).

[50] H. Jónsson, G. Mills, and K. Jacobsen (World-Scientific, Singapore, 1998).

[51] P. Kratzer, B. Hammer, and J. K. Nørskov, J. Chem. Phys. **105**, 5595 (1996).

[52] *The ASE code can be downloaded at, https://wiki.fysik.dtu.dk/ase.*

[53] P. Maragakis, S. A. Andreev, Y. Brumer, D. R. Reichman, and E. Kaxiras, J. Chem. Phys. **117**, 4651 (2002).

[54] R. G. Parr and R. J. White, J. Chem. Phys. **49**, 1059 (1968).

[55] K. C. Thompson, M. J. T. Jordan, and M. A. Collins, J. Chem. Phys. **108**, 8302 (1998).

[56] M. A. Collins, Theor. Chem. Acc. **108**, 313 (2002).

[57] G. Wiesenekker, G. J. Kroes, E. J. Baerends, and R. C. Mowrey, J. Chem. Phys. **102**, 3873 (1995).

[58] F. Gatti, C. Munoz, and C. Iung, J. Chem. Phys. **114**, 8275 (2001).

[59] C. Iung and F. Gatti, Int. J. Quant. Chem. **106**, 130 (2006).

[60] F. Gatti and C. Iung, Phys. Rep. **484**, 1 (2009).

[61] S. Woittequand and F. Gatti, article in preparation.

[62] F. Gatti, Y. Justum, M. Menou, A. Nauts, and X. Chapuisat, J. Mol. Spectrosc. **181**, 403 (1997).

[63] *MCTDH Manual.*

[64] M. H. Beck, A. Jäckle, G. A. Worth, and H. D. Meyer, Phys. Rep. **324**, 1 (2000).

[65] H.-D. Meyer, F. Gatti, and G. A. Worth, *Multidimensional Quantum Dynamics: MCTDH theory and applications* (Wiley-VCH, 2009).

[66] H.-D. Meyer, U. Manthe, and L. Cederbaum, Chem. Phys. Lett. **165**, 73 (1990).

[67] A. Raab, G. A. Worth, H.-D. Meyer, and L. S. Cederbaum, J. Chem. Phys. **110**, 936 (1999).

[68] A. Jäckle and H.-D. Meyer, J. Chem. Phys. **104**, 7974 (1996).

[69] A. Jäckle and H.-D. Meyer, J. Chem. Phys. **109**, 3772 (1998).

[70] R. Kosloff, J. Phys. Chem. **92**, 2087 (1988).

[71] D. T. Colbert and W. H. Miller, J. Chem. Phys. **96**, 1982 (1992).

Chapter 5

Reactive and non-reactive scattering of N_2 from Ru(0001): A 6D adiabatic study

This chapter is based on:

C. Díaz, J. K. Vincent, G. P. Krishnamohan, R. A. Olsen, G. J. Kroes, K. Honkala and J. K. Nørskov, J. Chem. Phys. **125** , 114706 (2006).

Abstract

We have studied the dissociative chemisorption and scattering of N_2 on and from Ru(0001), using a six-dimensional quasi-classical trajectory method. The potential energy surface, which depends on all the molecular degrees of freedom, has been built applying a modified Shepard interpolation method to a data set of results from density functional theory, employing the RPBE generalized gradient approximation. The frozen surface and Born-Oppenheimer approximations [Ann. Phys. (Leipzig) **84**, 457] were used, neglecting phonons and electron-hole pair excitations. Dissociative chemisorption probabilities are found to be very small even for translational energies much higher than the minimum reaction barrier, in good agreement with experiment. A comparison to previous low dimensional calculations shows the importance of taking into account the multidimensional effects of N_2 rotation and translation parallel to the surface. The new calculations strongly suggest a much smaller role of non-adiabatic effects than previously assumed on the basis of a comparison between low-dimensional results and experiments [J. Chem. Phys. **115**, 9028 (2001)]. Also in agreement with experiment, our theoretical results show a strong dependence of reaction on the initial vibrational state. Computed angular scattering distributions and parallel translation energy distributions are in good agreement with experiments on scattering, but the theory overestimates vibrational and rotational excitation in scattering.

5.1 Introduction

The Surface Science community has taken a strong interest in the N_2/Ru(0001) system during the last few decades, due to the fact that Ruthenium is considered

a good candidate for replacing Iron as a catalyst in the industrial synthesis of ammonia, and because dissociation of N_2 is the rate-limiting step in this process. As a consequence of this interest a large number of experimental [1-13] and theoretical [5, 11, 14] studies have been published, showing unusual and sometimes controversial results. Although recent theoretical and experimental work [15-17] has proved that dissociation at Ru-steps is much more efficient than at the Ru(0001) terraces, N_2/Ru(0001) is of much fundamental interest. This system can be considered as a new prototype system for activated dissociative chemisorption, because it exhibits properties quite different from the well studied H_2/Cu [18] system. For instance, the minimum reaction barrier (V^*) is located further in the exit channel for N_2/Ru(0001) ($r_b \approx r_e + 1.3\ a_0$) [7] than for H_2 /Cu ($r_b \approx r_e + 0.8\ a_0$) [19] , and its height is much larger for N_2/Ru(0001) (around 2 eV) [4] than for H_2 /Cu (around 0.5 eV) [19].

One of the most striking features of the N_2/Ru(0001) system is that the measured reaction probability (S_0) increases very slowly with the incidence energy (E_i) for energies above the minimum reaction barrier and saturates at a very small value (10^{-2}) for $E_i \gg V^*$. Experimentally, it has also been found that the dissociation probability shows a very strong dependence on the initial vibrational state, vibrational energy being more efficient at promoting reaction than translational energy [4] (see also Fig. 1 of Ref. [9]). Isotope effects have also been investigated [6]. No isotope effect has been observed in the classical regime ($E_i \geq V^*$), but for lower energies the reaction probability for $^{15}N_2$ is smaller than for $^{14}N_2$, which has been interpreted in terms of tunneling through a large barrier for dissociation [6] . Another unexpected feature is the lack of vibrational excitation in molecular-beam experiments for N_2 scattering from Ru(0001) [13] , and the small amount of vibrational excitation observed in laser assisted associative desorption (LAAD) [11] , associative desorption being the reverse process to dissociative chemisorption. Late barrier systems (reaction barrier found for an extended vibrational coordinate) are expected to exhibit significant vibrational excitation of the molecule upon scattering and associative desorption [20-22]. This is not the case for the N_2/Ru(0001) system. Moreover, the analysis of the LAAD experiments presented in [11] suggests that $\frac{2}{3}$ of the energy used by the molecule to overcome the barrier is lost to the surface.

Much recent theoretical effort has been invested in understanding these unusual experimental findings. In Ref. [4] a two-dimensional (2D) non-adiabatic tunneling model was proposed, in which only 2 degrees of freedom (DOFs) of the molecule, r (N-N distance) and Z (molecule-surface distance), were taken into account in the dynamics (see Fig. 5.1(a)). In this model the potential energy surface (PES) includes a physisorption term (V_{phys}), describing the gas phase molecule attached to the surface, a chemisorption term (V_{chem}), describing the sum of the N-atom surface potentials, and a non-adiabatic coupling potential to account for the transition between V_{phys} and V_{chem}. This model reproduces quite accurately the experimental S_0, but introduces a number of parameters that need to be adjusted. It is not yet clear whether these parameters mostly reflect the true system dynamics or rather the restricted number of molecular DOFs treated. Two other
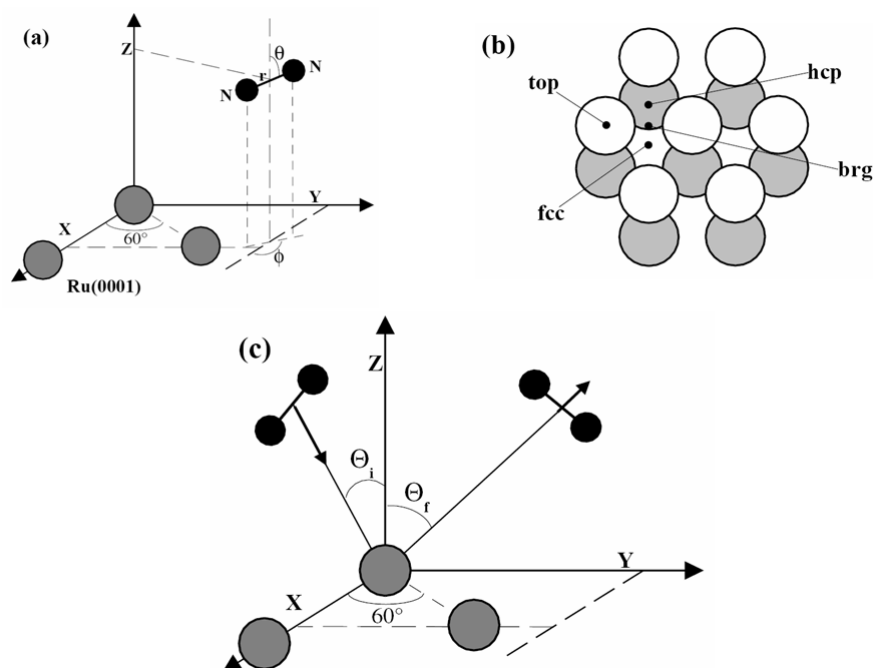
Figure 5.1: (a) The coordinate system used to define the position and orientation of N_2 relative to the Ru surface. (b) High symmetry points of the Ru(0001) surface. White (gray) spheres denote atoms in the first (second) layer. Atoms in the third (fourth) layer are directly below the atoms in the first (second) layer. (c) Coordinate system used to describe the direction of the velocity vector of the incident and scattered N_2.

low dimensional models were proposed in Ref. [11]: (i) A 2+1D(r,Z;q) adiabatic model, in which not only r and Z are included, but also the coupling to surface phonons via a single Einstein oscillator (q) [23] . This low dimensional adiabatic model failed completely at reproducing the experimental value of S_0, overestimating it by 2 orders of magnitude. (ii) A 2+2D(r,Z;q,Γ) non-adiabatic model in which an additional coupling to electron-hole (e-h) pair excitations (Γ) is included via electronic friction and fluctuating forces [24]. Although this model gave reaction probabilities in semi-quantitative agreement with experiment, this agreement was only obtained by using a very strong non-adiabatic coupling, which was 12 times larger than that required for the description of vibrational damping of $O_2(v{=}1)$ adsorbed on Pt(111) [25]. The question in this case is then whether such a strong non-adiabatic coupling is physically reasonable. A recent low dimensional theoretical study [26], aiming to quantify the influence of non-adiabatic effects on the reactivity of N_2 + Ru(0001), suggests a smaller role of non-adiabatic effects, but the low dimensionality of the dynamical model do not allow one to reach a firm conclusion.

The low dimensional calculations were mainly focused on the influence of non-adiabatic effects and on how to include them in the dynamics. The influence of non-adiabatic effects on molecule-surface reactions has become a hot topic in the last few years, thanks to recent experiments showing direct evidence of non-adiabatic effects in molecule-surface scattering such a e-h pair excitations accom-

panying chemisorption of atoms and molecules [27], and ejection of electrons from low work function metal surfaces accompanying scattering of highly vibrationally excited molecules with high electron affinity [28]. These experiments might be viewed as questioning the validity of the Born-Oppenheimer (BO) approximation [29] for molecule-surface reactions. As discussed in Ref. [30], one reason that the BO approximation could seem suspect for the scattering of molecules from metal surfaces is that the metal surface electronic states exhibit a continuum energy distribution. Nevertheless this approximation has been used successfully in modeling molecule-surface reactions for a large number of systems [18, 31, 32] and in modeling heterogeneous catalysis [33, 34]. On the other hand, recent theoretical work has shown that for some special systems, such as a high-spin molecule (O_2) [35] and/or molecules of high electron affinity (O_2 and NO) [36] reacting on a metal surface with a low density of states at the Fermi-level (Al(111)), the reaction can be better described using a non-adiabatic (diabatic with [36] or without coupling [35]) model.

In the case of N_2, we have a low-spin molecule of low electron affinity, so that, in principle, non-adiabatic effects are expected to be less important. Low dimensional results seem to contradict this expectation (see discussion above), giving rise to the following questions: Is N_2/Ru(0001) another special system for which the adiabatic approximation fails to account for experimental results on reaction, or are the molecular DOFs associated with rotation and translation parallel to the surface perhaps more important for this system than for other systems [37]. In order to give appropriate answers to these questions we here present a six-dimensional (including the 6 DOFs of the molecule) adiabatic (neglecting e-h pair excitations) study of N_2 interacting with a Ru(0001) surface. Assuming the system to be reasonably well described by density functional theory (DFT) and the dynamics method employed (see below), the difference between the computational results and experiments should then allow for a verdict on the importance of non-adiabatic effects for this particular system.

The paper is organized as follows: In Sec. 5.2 we describe the methodology used, i.e., the electronic structure method used to compute the molecule-surface interaction energies, the interpolation of the potential, and the quasi-classical trajectory (QCT) method used in the dynamics calculations. In Sec. 5.3 we first present the main features of the six-dimensional (6D) PES obtained for N_2/Ru(0001), and then we discuss the dynamics results obtained for dissociative adsorption and scattering. A short account of some of the results obtained for dissociative adsorption has been published elsewhere [38]. Finally, we summarize the main conclusions in Sec. 5.4.

5.2   Theory

To build the 6D PES for the N_2/Ru(0001) system we have used the Modified Shepard (MS) interpolation method [39, 40] adapted for molecule-surface reactions [41], a new feature being that for the first time we use a direct interface to DFT. We have considered the six DOFs of the molecule, r, Z, the coordinates X and Y that represent the motion parallel to the surface, and the orientation of the molecule described by the polar (θ) and the azimuthal (ϕ) angles (see Fig. 5.1(a)).

We have made two main approximations: (i) We take the surface as frozen, i.e., we consider the surface atoms fixed in their equilibrium positions. Although N_2 is a heavy molecule and some energy exchange with the surface could be expected, this approximation is justified, to some extent, by the experimental results showing dissociation probabilities to be independent of surface temperature (T_s) [3, 4]. (ii) The BO approximation is applied, neglecting possible non-adiabatic effects (such as e-h pair excitations).

5.2.1 Electronic structure calculations

The electronic structure data points have been computed with DFT using the DACAPO code [42]. The generalized gradient approximation (GGA) is used in the description of the exchange-correlation energy of the electrons. In applying the GGA we have used the RPBE functional, which gives smaller over-binding and more accurate chemisorption energies than the PW91 functional [43], and which has been shown to perform well in modeling ammonia production [34]. The ion cores were described using nonlocal ultrasoft pseudopotentials (USPP) [44] (with core cutoff radii of $r_c^N = 0.6 a_0$ and $r_c^{Ru} = 0.9 a_0$) and a plane wave basis set was used for the electronic orbitals.

The adsorbate/substrate system is modeled using a three-layer slab, and a 2×2 surface unit cell. The interlayer distance (c/2) was relaxed, and had a final value of 2.12 Å, slightly compressed with respect to the calculated bulk case (2.18 Å). A vacuum layer of 13.03 Å was placed between the slabs in the Z direction to avoid artifacts caused by the use of periodic boundary conditions in the direction perpendicular to the slab. To sample the Brillouin zone we have used a set of 18 Chadi-Cohen k-points [45]. The cutoff energy for the plane wave basis was set at 350 eV. Using these parameters the molecule-surface interaction energies are converged to within 0.1 eV of the RPBE results for the given USSP. We have found a minimum energy barrier of 2.27 eV in qualitative agreement with a previous calculation [5], in which a value of about 2.4 eV was found for the molecule parallel to the surface and dissociating in the bridge to hollow geometry.

5.2.2 Interpolation method

In the MS interpolation method, the interpolated PES is given by a weighted series of Taylor expansions centered on DFT data points, sampled throughout the configuration space of the system. To get a physically more reasonable behavior when two atoms are close to each other, the inverse interatomic distances, $Q_i = 1/R_i$ (R_i are the interatomic distance that define the system), are used instead of the direct interatomic distances [46]. Thus, any configuration of the system is defined by the vector $\mathbf{Q} = [1/R_1,...,1/R_{n(n-1)/2}]$, where n is the number of atoms needed to model the system. To model our system we use 5 atoms, 2 describing the N_2 approaching the Ru(0001) surface, and 3 atoms, which are kept fixed, to model the frozen surface [41].

For each geometry $\mathbf{Q}$ a set of $3n$-6 algebraically independent linear combinations of the $n(n-1)/2$ interatomic distances, $\zeta(Q)$, can be defined in terms of the inverse distances as [47]:

$$\zeta_m = \sum_{k=1}^{n(n-1)/2} U_{mk} Q_k \quad (m = 1, ..., 3n - 6) \tag{5.1}$$

,

where U_{mk} is the transformation matrix from Cartessian coordinates to reciprocal bond lengths (see Ref. [47] for details). The potential energy at a configuration $\mathbf{Q}$, in the vicinity of a data point $\mathbf{Q}(i)$, can be expanded as a second-order Taylor expansion $T_i(\mathbf{Q})$, in these coordinates,

$$\begin{aligned} T_i(\mathbf{Q}) = \ & V[\mathbf{Q}(i)] + \sum_{k=1}^{3n-6} [\zeta_k - \zeta_k(i)] \frac{\partial V}{\partial \zeta_k}\Big|_{\mathbf{Q}=\mathbf{Q}(i)} \\ & + \frac{1}{2} \sum_{k=1}^{3n-6} \sum_{j=1}^{3n-6} [\zeta_k - \zeta_k(i)] \times [\zeta_j - \zeta_j(i)] \frac{\partial^2 V}{\partial \zeta_k \partial \zeta_j}\Big|_{\mathbf{Q}=\mathbf{Q}(i)} + ..., \end{aligned} \tag{5.2}$$

where $V[\mathbf{Q}(i)]$, the value of the potential at $\mathbf{Q}(i)$, and the gradients at this point, are computed analytically by DACAPO. The second derivates are computed from the gradients using forward differencing.

The total potential energy at any configuration $\mathbf{Q}$ is then taken as:

$$V(\mathbf{Q}) = \sum_{g \in G} \sum_{i=1}^{N_{data}} w_{g \circ i}(\mathbf{Q}) T_{g \circ i}(\mathbf{Q}), \tag{5.3}$$

where the term $T_{g \circ i}(\mathbf{Q})$ represents a second-order Taylor expansion and $w_{g \circ i}(\mathbf{Q})$ a normalized weigh function (see [41, 48] for more details). N_{data} is the number of DFT data in the interpolation, G is the symmetry group and $g \circ i$ denotes the transformation of the ith data point by the group element g. To take into account the full symmetry of the system, a sum is taken over both the DFT data points and their symmetry equivalent points.

5.2.3   Implementation of the MS method in Grow

Unlike other interpolation schemes (see for instance [49, 50]), in the MS method the sampling of DFT data points is non-uniform, the density of data points being higher in the so-called dynamically important regions, which are found performing classical trajectory simulations. The idea behind the Grow method is that to calculate observables from a chemical reaction dynamics simulation, we only need to know the PES in the region of space through which the molecules pass during the dynamics.

In order to choose an appropriate data set the following iterative scheme [39, 40] is used:

1. We start with an initial version of the PES, which only includes a few points located along several reaction pathways. In our case, the initial PES contained 70 initial points chosen along 4 reaction pathways, i.e., 19 for the top, 19 for the bridge and 19 for the hollow configuration, these three reaction pathways corresponding to the highest symmetry sites of the surface (see

Fig. 5.1(b)), and 13 points along a minimum energy pathway. The minimum energy pathway was found by minimizing the N_2/Ru(0001) interaction energy with respect to θ, ϕ, X, Y and Z, while keeping r fixed, for several values of r.

2. Using this initial PES a few classical trajectories (typically 10) are run (see below). In order to assure the accurate representation of the PES for the whole energy range in which we are interested to carry out our study, we have grown the PES using simultaneously several translational energies (only normal incidence is considered in the grow process) and two rovibrational initial states (see Table 5.1). Along each trajectory the molecular geometries explored by the simulation are periodically stored.

v_i	0 ($E_{rv} = 0.142$)						1 ($E_{rv} = 0.427$)				
E_i	2.32	2.82	3.12	4.12	4.87	5.61	2.57	2.97	3.62	4.37	5.12

Table 5.1: Translational energies and rovibrational initial states used in the growth process. In all cases $J_i = 0$. Energies are in eV.

3. From the stored geometries a new point is chosen (and added to the PES) according to one of two criteria (see [39, 48] for more details): (i) The 'h-weight' criterion, which is based on the assumption that the best location for a new point would be the region most frequently visited by the trajectories. Thus, according to this criterion, the new point is added in the region of the PES most frequently visited, as long as there are not many data points already representing this region in the PES data set. (ii) The 'variance' criterion, which is based on the assumption that the accuracy of the PES will be best improved if the new point is added in the region where the determination of the energy is suspected to be the most inaccurate.

4. Once the PES is updated by adding the new chosen point, we restart the grow process from (2).

5. After about 100 points are added, the accuracy of the PES is checked by computing an accurate value of the desired observable (in our case the reaction probability) from a more extensive classical trajectory simulation (10000 trajectories). The grow process is stopped when the observable is considered to be converged, within a given tolerance. The analysis of the convergence of the reaction probability, for several incidence energies and two initial vibrational states, is shown in Fig. 5.2 , where we have represented the reaction probability as a function of the number of data in the PES. To obtain an accurate PES for N_2/Ru(0001) we have computed 2500 DFT data points (70 initial points + 2430 added points).
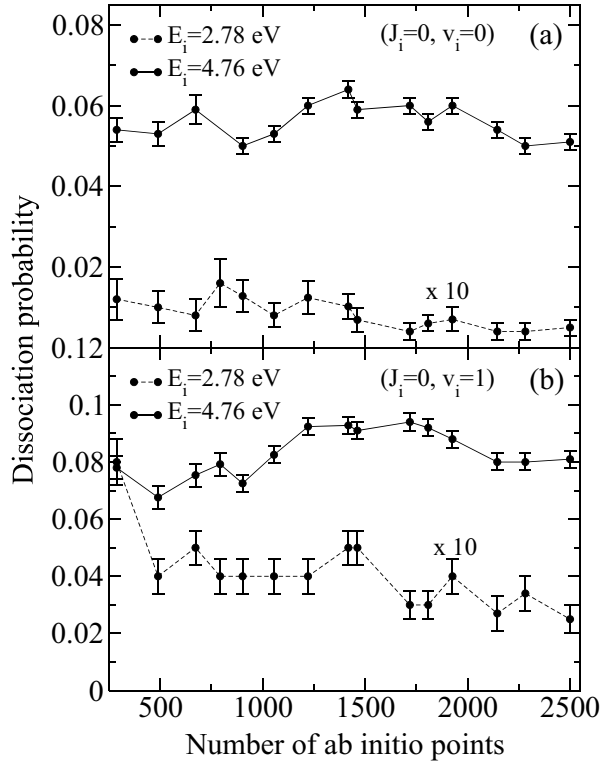
Figure 5.2: The dissociation probability as a function of the number of DFT points added to the PES data set for two incidence energies, E_i=2.78 eV and E_i=4.76 eV. (a) v_i=0 and J_i=0, (b) v_i=1 and J_i=0.

5.2.4   Quasi-classical dynamics

We have performed classical dynamics to find the dynamically important regions during the grow process and to compute reaction and scattering probabilities. In both cases, we have used the so-called QCT method [51] , in which the initial zero point energy (ZPE) of the molecule is included in the dynamics. Although these kind of calculations are susceptible to the so-called ZPE violation problem (see Ref. [52]), for an activated system this problem is expected to play a minor role at energies above the threshold to reaction. The QCT method generally gives accurate results for activated molecule-surface reactions [53-56]. Note that the vibrational softening (adiabatic transfer of energy from internal to translational motion) that takes place when the molecule approaches the surface is taken into account in the QCT method (its absence in the classical trajectory (CT) method leads to underestimated reaction probabilities [57].

To compute the reaction and the scattering probabilities we have solved the classical equations of motion using the velocity-Verlet algorithm [58]. For each initial energy and initial rovibrational state, the probabilities are calculated as an average over the molecular initial conditions (internal coordinates and internal conjugated momenta). A Monte-Carlo sampling method is used to simulate the

molecular initial conditions for each set of initial parameters (E_i, v_i, J_i). In order to obtain low statistical errors (typically between 10% and 3% depending on the translational energy E_i) we have computed 10000 trajectories for each value of E_i and rovibrational state of N_2. We consider that dissociation has taken place whenever r reaches 5.0 a_0 with a positive radial velocity. The molecule is considered to be reflected whenever Z becomes equal to Z_i, Z_i being the initial distance between the molecule and the surface (7.5 a_0), with the molecule's velocity vector pointing towards the vacuum.
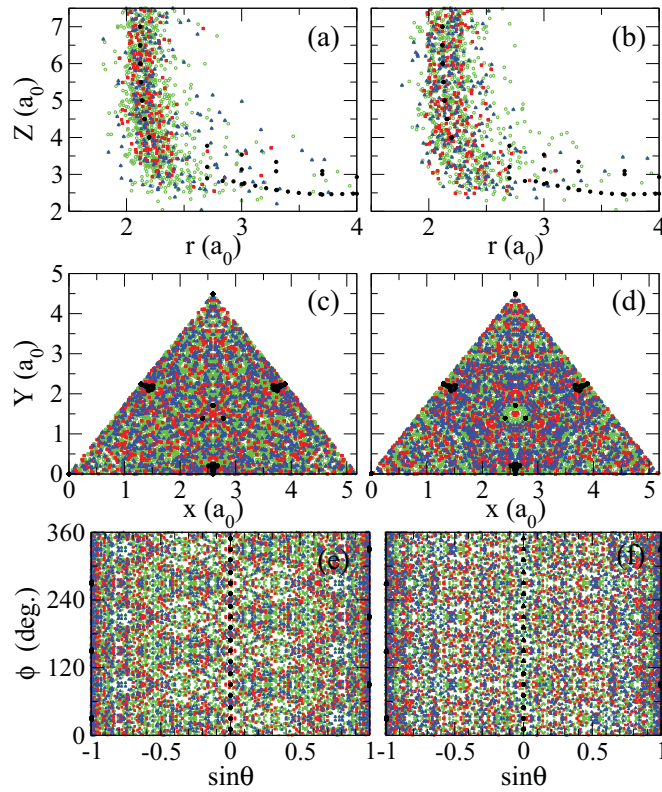
Figure 5.3: The PES data set in (Z,r) representation (a and b), in (X,Y) representation (c and d), and in (θ, ϕ) representation (e and f). The plots (a), (c) and (e) are obtained for v_i=0, and the plots (b), (d) and (f) for v_i=1. Black circles: initial DFT points; red squares: DFT points added for the lower energy growth; blue triangles: DFT points added for the higher energy growth; green circles: DFT points added for intermediate energies growth.

5.3 Results and discussion

5.3.1 The N_2/Ru(0001) PES

The method used to build the PES allows us to locate easily the regions of the PES important for the dynamics, by merely looking at the distribution of points in

configuration space. In Fig. 5.3 we show the computed DFT data points projected
on the (Z,r) (Fig. 5.3(a) and 5.3.(b)), (X,Y) (Fig. 5.3(c) and 5.3(d)) and (θ,ϕ)
(Fig. 5.3(e) and 5.3(f)) hyperplanes. Looking at Fig. 5.3(a) and 5.3(b), we can
see that most of the points are added in the entrance channel (valley of reactants),
with reflects the low reactivity of N_2+Ru(0001). We can also see that for the
highest energy (for both initial states v_i=0 and v_i=1) there are more points added
around the transition state (located at r=3.4a_0 and Z=2.53a_0) than for the lowest
energy, which is consistent with the fact that the reactivity is higher for higher
translational energies. Figure 3c and d show that the added points are uniformly
distributed over the (X,Y) and ($\sin\theta,\phi$) planes. The ($\sin\theta,\phi$) representations show
a slightly higher concentrations of points around $\sin\theta=\pm1$, which, with the way
we have defined θ in the classical dynamics, corresponds to the orientation of the
molecule most favorable for dissociation.
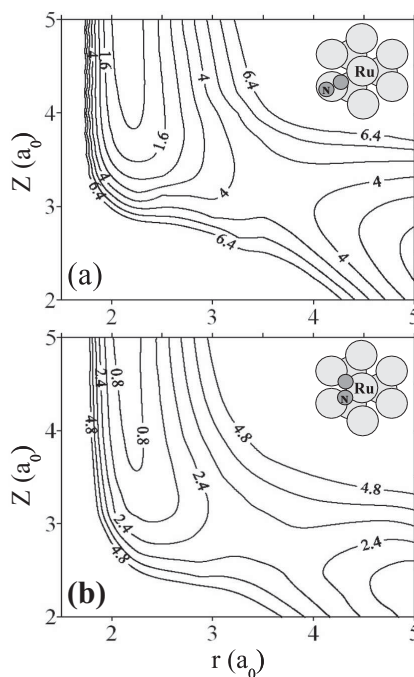
Figure 5.4: 2D cuts through the PES for (a) the molecule approaching the top site
with the N-N bond parallel to the surface (θ=90°) and (b) the molecule approach-
ing a site halfway between the top and fcc sites, also with θ=90°. The potential
is for the molecule oriented as indicated in the inset. The spacing between the
contour levels is 0.8 eV.

In Fig. 5.4 we show two 2D (r,Z) representations of the PES. We show two
configurations for which the molecule approaches the surface with its N-N bond
parallel to the surface (θ=90°). In Fig. 5.4(a) the center-of-mass (CM) of the
molecule is located over a top site (see Fig. 5.1(b)), in Fig. 5.4(b) the CM is
located halfway between a top site and a fcc site, with each N atom pointing
toward a hcp site. We can see that both configurations present very high barriers
towards reaction, which are located far in the exit channel, i.e., at large r. The
second configuration is close to the lowest barrier (V^*=2.27 eV) geometry, which

is located at (X, Y, Z, r, θ, ϕ)=(1.4a_0, 2.20a_0, 2.53a_0, 3.40a_0, 86.23°, -29.33°). This PES does not only present high barriers, but also very large anisotropy and corrugation. In Fig. 5.5 we show the energy profile near the minimum barrier geometry. From this figure we can see that both the anisotropy (Fig. 5.5(a)) and the corrugation (Fig. 5.5(b)) at the barrier are much larger for N_2/Ru(0001) than for the H_2/Cu system [50], i.e., N_2/Ru(0001) presents a much narrower bottleneck towards reaction than H_2/Cu.
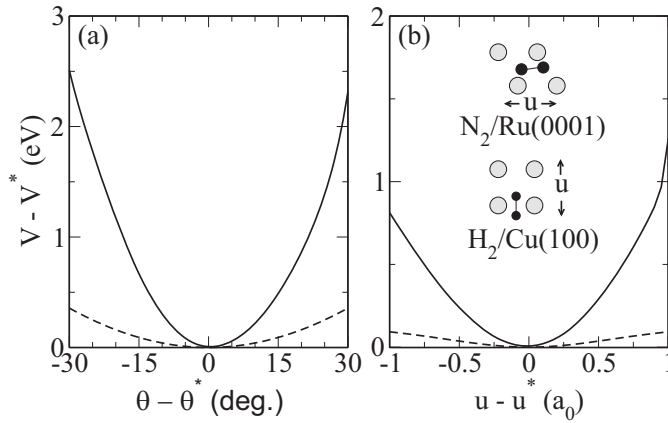
Figure 5.5: The anisotropy and corrugation of the N_2/Ru(0001) (solid line) and H_2/Cu(100) [50] (dashed line) potentials near the minimum barrier is illustrated by plotting the dependence of $V - V^*$, V being the potential and V^* the potential at the minimum barrier geometry, on $\theta(a)$ and u (b), keeping all other coordinates fixed to the barrier geometry $\mathbf{Q}*$. Here, u is the coordinate for motion along a straight line parallel to the surface, such that V varies the least.

5.3.2 Dissociative adsorption

In this section we present reaction probabilities for normal incidence obtained using the QCT method. In order to compare our QCT results directly with the experimental ones, we have to include in our calculations the effect of the nozzle temperature (T_n), i.e., in principle we have to use the same rovibrational initial states distribution in our simulations as was present in the experiments. To find the initial vibrational (v_i) state distribution corresponding to the different T_n, we assume that the vibrational temperature T_{vib} is approximately equal to T_n. The populations of the different initial vibrational states as a function of the simulated T_n are shown in Table 5.2.

To determine the initial rotational state distribution for a given T_n is not straightforward, because it depends not only on T_n but also on the experimental seeding and expansion conditions, i.e., it depends on the specific conditions

under which each experiment was performed. However, as shown in Fig. 5.6 where we have plotted the reaction probabilities as a function of E_i for several J_i, the reaction probability does not depend significantly on the initial rotational state (J_i) for the J states with significant population at the rotational temperatures relevant to the molecular beams used in the experiments [59]. In fact, the reaction probabilities are the same to within the statistical accuracy of the calculations.
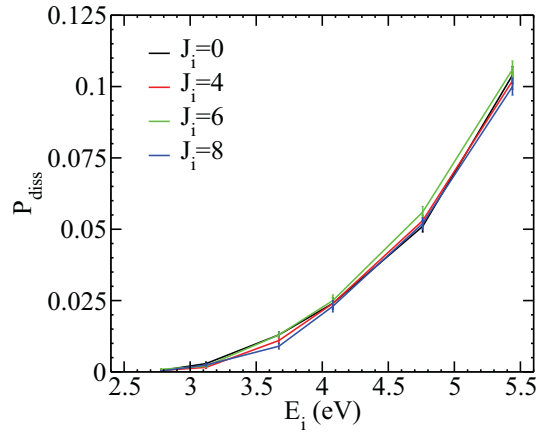
Figure 5.6: The reaction probabilities as a function of the translational energies for several initial rotational states J_i and v_i=0.

$T_n(K)$	$P_{v=0}(\%)$	$P_{v=1}(\%)$	$P_{v=2}(\%)$
700	100	0	0
1850	83	14.5	2.5

Table 5.2: Initial vibrational state distributions used in our QCT simulations.

In Fig. 5.7 we compare our 6D QCT reaction probabilities with some of the available experimental measurements [4, 9]. The agreement between theory and experiment is remarkable. From the comparison between our 6D model and the 2+1D model (results of which are also included in Fig. 5.7) we see that the inclusion of the remaining 4 molecular DOFs (associated with rotation and translation parallel to the surface) decreases the reaction probability by two orders of magnitude. This illustrates the fundamental role played by these 4 DOFs. In fact, the inclusion of the rotation and parallel motion lowers the reaction probability much more for N_2/Ru(0001) than for the prototype system H_2/Cu(100) [18]. This is due to the fact that, as has been shown in section IIIA , both the corrugation and the anisotropy near the minimum barrier are much higher for N_2/Ru(0001) than
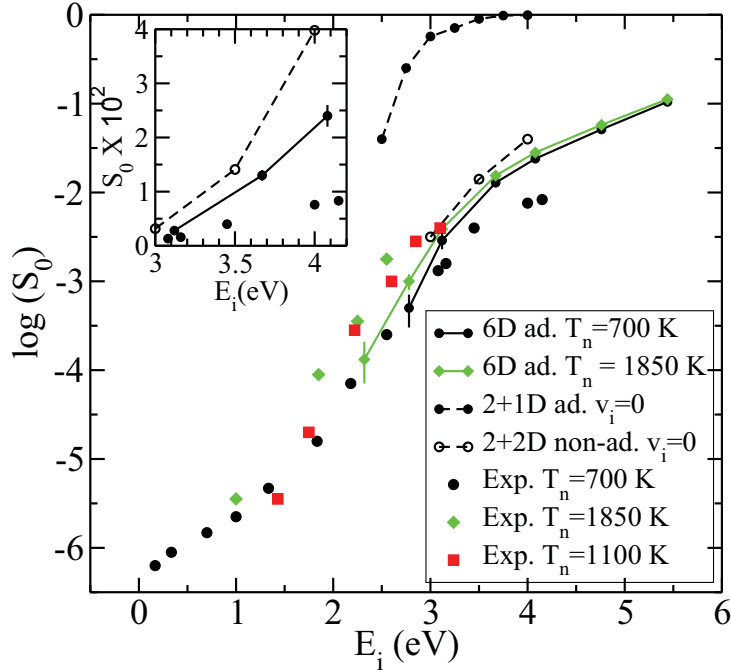
Figure 5.7: The log of the probability of N_2 dissociation on Ru(0001) is plotted vs. normal translational energy E_i. The continuous line with full symbols represent 6D adiabatic calculations, the dashed line with full symbols represent 2+1D adiabatic calculations from [11], and the dashed line with open symbols 2+2D the non-adiabatic calculations from [11]. Experimental measurements: full circles from [4]; full green diamonds from [4]; full red squares from [9]. The inset shows S_0 times 10^2 vs. normal translational energy. Results are shown for different nozzle temperatures (T_n).

for H_2/Cu(100). Thus the barrier is a much narrower bottleneck for N_2/Ru(0001) system, explaining the lower reactivity.

By looking more carefully at the comparison between 6D adiabatic theory and experiment for the higher E_i at which measurements are available (see inset Fig. 5.7), we see that 6D QCT dynamics overestimates reaction probabilities by a factor of about 3 at the highest E_i for which experimental results are available (the non-adiabatic 2+2D model [11] overestimates S_0 by a factor of about 5). In the below analysis, we assume the experimental reaction probabilities [4, 9] to be accurate, even though there could be considerable uncertainty in their absolute value, for instance, due to the procedure comparing the TPD (Temperature Programmed Desorption) of the small amount of N_2adsorbed to that of a monolayer N_2 [59, 60]. Other sources of error are in the determination of the collision energy and of the flux [60]. These factors should, however, lead to an error of no more than a factor 2 in the reaction probability (≈ 0.01) measured at the highest E_i (≈ 4 eV).

In the theory, several factors can then be responsible for the remaining disagreement between experiment and 6D adiabatic theory: (i) approximations made in the implementation of the adiabatic frozen surface model; (ii) exclusion of phonons; (iii) exclusion of e-h pair excitations. Concerning (i), although DFT is, in principle, an exact theory and has allowed the calculation of quite accurate dissociation probabilities for H_2-metal systems [18, 32], in practice its use requires some approximations. For instance, the exact form of the exchange-correlation functional is unknown, and the use of pseudopotentials to describe the ion cores is also a source of possible inaccuracies. These approximations lead to some uncertainties in the barrier heights of the system [61], and therefore also in the reaction probabilities. We have chosen to use the RPBE GGA functional [43], instead of the, at present, most used PW91 functional [62]. The RPBE functional has been selected because: (a) The PW91 functional fails [34] to predict the barrier found experimentally (0.4 eV) for N_2 + stepped Ru, which is however accurately described by the RPBE functional [15]. (b) The RPBE functional more accurately describes atomic and molecular chemisorption on metal surfaces than the PBE functional, which gives values close to the PW91 functional [43] . (c) A recent systematic study [63] of the accuracy of several functionals for barrier heights in small gas phase systems shows a better agreement between RPBE results and results of more accurate hybrid functionals than between these hybrid functionals and the PW91 functional. The QCT method, as discussed above, has been shown to provide accurate results for activated dissociation of H_2 on metal surfaces [53, 55], H_2 presenting a much greater challenge to the classical approximation than N_2. Concerning (ii), although experimentally a minimal influence of T_s on reaction was found (for T_s between 500-850 K) within the classical regime ($E_i \geq V^*$) [3, 4], this does not exclude the possibility that N_2 (which is rather heavy compared to H_2 , for which the frozen surface approximation works quite well [31, 64]) transfers energy to the metal surface phonons on impact. In fact, low dimensional calculations (including only r and Z) showed an increase in the classical reaction threshold of 0.5 eV upon inclusion of phonons. Although this result can not be directly extrapolated to our 6D QC calculations, it is likely that the inclusion of phonons will lower the reaction probability. Concerning (iii), in the case of e-h pair excitations the LAAD experiments [11] and experiments on vibrationally inelastic scattering [13], as well as own our inelastic scattering study showing an overestimation of the energy transfer to molecular vibration (see section IIIC), suggest that the remaining discrepancy between 6D adiabatic theory and experiment is, at least in part, due to non-adiabatic effects. Taking into account that the inclusion of phonons should also reduce the reaction probability, we can establish the factor 3 discrepancy observed between 6D adiabatic theory and experiment at the highest E_i (inset Fig. 5.7) as a reasonable upper bound to the effect that e-h pair excitations might have on the reactivity, at high incidence energies (about 4 eV).
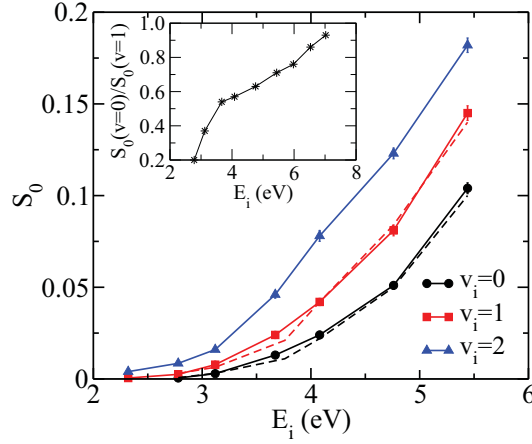
Figure 5.8: Computed dissociation probability vs. incidence energy for several initial vibrational states v_i, and $J_i=0$. Continuous line $^{14}N_2$. Dashed line $^{15}N_2$. The inset shows the dissociation probability for $v_i=0$ divided by the dissociation probability for $v_i=1$ as a function of the incidence energy .

The experimental and theoretical probabilities increase considerably with T_n (Fig. 5.7). To study the effectiveness of initial vibrational excitation at increasing reaction, we have computed the vibrational efficacy, which is a measure of the relative importance of molecular vibration and translation for promoting reaction, and is given by:

$$\eta(S_0) = \frac{[\epsilon_{v=0}(S_0) - \epsilon_{v=1}(S_0)]}{E_{vib}(v=1) - E_{vib}(v=0)},\tag{5.4}$$

where E_{vib} is the molecule's vibrational energy in the gas phase, and $\epsilon(S_0)$ is the energy required to obtain a reaction probability S_0 when the molecules are initially in a vibrational state v. To evaluate η we have computed initial vibrational state resolved dissociation probabilities (Fig. 5.8). For an energy range [3.3 eV - 5.5 eV] and S_0 between [2.5×10^{-2}-0.1], the average value we compute for $\eta(S_0)$ is about 1.6 (as the value of $\eta(S_0)$ depend slightly on the value of S_0, we have computed $\eta(S_0)$ for 4 different values of S_0 obtaining values between 1.4 and 1.8). Thus, in our 6D adiabatic model vibrational excitation promotes reaction more efficiently than normal translational energy E_i. This result is in reasonable agreement with a previous estimated value of 1.3 [5], where reaction probabilities were obtained from detailed balance. It is also in qualitative agreement with an analysis of the previous experiments [4]. To calculate the value of η from the molecular beam results, we suppose $S_0(T_n = 700 \text{ K}) = S_0(v=0)$ and $S_0(T_n = 1850 \text{ K}) = (1\text{-c})S_0(v=0) + cS_0(v=1)$, c being the fraction of molecules in $v=1$ at 1850 K assuming that only $v=0$ and 1 are populated. Doing this analysis we obtain $\eta \approx 3.8$. As we have neglected $v=2$ (also present for $T_n = 1850$), we are overestimating the experimental value of η. We have evaluated this possible overestimation by doing a similar analysis of our $S_0(T_n)$, both including and excluding the $v=2$ contribution.

Our analysis suggests that excluding the $v=2$ contribution to $S_0(T_n)$ leads to an overestimation of $\eta(S_0)$ by about 0.5. The result of this analysis of the efficacy is in contrast with a previous statement [9] that the effect should be less than for H_2/Cu ($\eta \approx 0.5$). However, this statement was not backed up by an analysis in terms of the vibrational efficacy. Although quantitatively there are discrepancies between our adiabatic results and previous experiments [4], both show that excitation of the N_2vibration promotes reaction much more efficiently than increasing the N_2 translational energy normal to the surface. A similar finding was mentioned in Ref. [15].
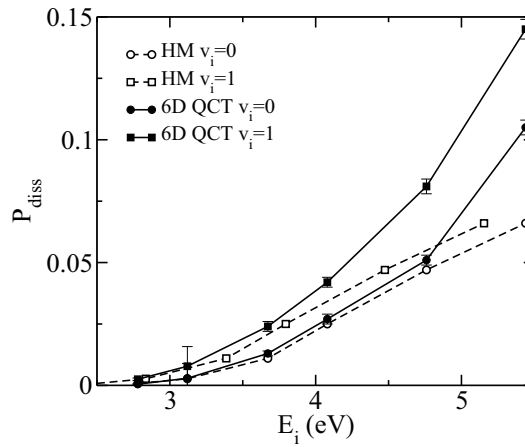
Figure 5.9: The fraction of accessible 2D paths toward dissociation as a function of the translational energy. Solid lines and filled symbols: 6D QCT dissociative probabilities. Dashed lines and open symbols: hole model results.

This high vibrational efficacy contrasts with the relative low η found in other N_2/metal systems [65, 66]. However a similar high vibrational enhancement has been observed previously, for instance, for $CH_4/Ni(111)$ [67]. It is worth noticing that in the case of $N_2/Ru(0001)$ the sticking curves for different v_i apparently saturate at about the same amplitude for $v=0$ and $v = 1$ (see inset Fig. 5.8), therefore we can consider that all the v_i dependence is contained in η (see Ref. [68] for more details). Now the question is how the vibrational energy can be more efficient than E_i at promoting reaction. In principle, a vibrationally excited molecule has a maximum extra energy to overcome the barrier, $E_v = n\hbar\omega_0$ (n being the vibrational state), which means that, in principle, the vibrational excitation cannot reduce the E_i required to overcome the barrier by more than E_v. One possible explanation to this phenomenon was proposed in [67]: a vibrationally excited molecule surmounting a late barrier can in some cases access phase space regions where the transition state is lower than those accessed by molecules in the vibrational ground state (see Fig. 3 of Ref. [67]), which means that the reaction barrier seen by molecules in $v_i=1$ is smaller (by ΔE) than for molecules in $v_i=0$.

Thus, the translation energy needed by a molecule in $v_i=1$ to overcome the barrier is reduced by $E_v+\Delta E$, which can explain how η can be bigger than 1.
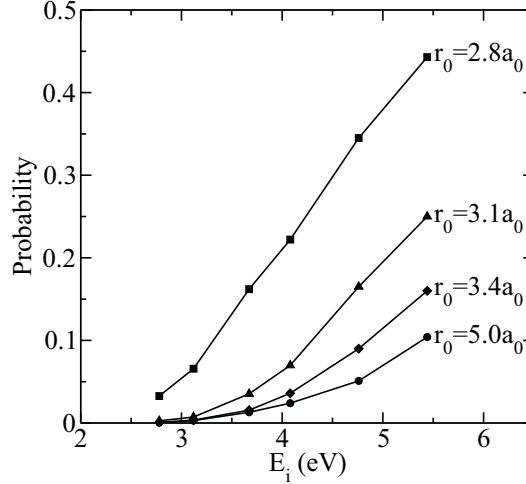
Figure 5.10: The probability of the molecule to reach an interatomic distance r_0, with $r_0=3.4a_0$ being the minimum reaction barrier and $r_0 = 5a_0$ is the dissociation condition.

In Fig. 5.8 we show the initial vibrational state resolved reaction probabilities for the heavier isotope $^{15}N_2$. Taking into account the statistical errors intrinsic to the calculation, no isotope effect is observed. This result is in perfect agreement with the experimental findings [6], according to which isotope effects are only observed for incidence energies below the minimum reaction barrier (the quantum regime).

We now address the following fundamental question: Why is the reactivity so small in the $N_2/Ru(0001)$ system? As we have shown in section IIIA, the system shows a very high anisotropy and corrugation around the minimum reaction barrier (see Fig. 5.5), which means that the potential seen by a molecule approaching the surface depends strongly on its position and orientation over the surface. Of course, in a 6D scenario all values of (X,Y,θ,ϕ) that are compatible with the given energy are allowed, which means, from a statistical point of view, that the number of molecules approaching the surface with a geometry favorable to dissociation is very small (smaller than in the case of H_2/Cu). On the other hand, if steering in the rotational and the translational motion parallel to the surface would be efficient enough to drive the molecule to the minimum energy reaction path, thereby avoiding the highest barriers when it approaches the surface, a strong corrugation and anisotropy would not be an impediment to reaction.

To study the efficiency of the dynamics to drive the molecule to the minimum energy reaction path, we have compared our 6D QCT results with that obtained using the hole model (HM) [69]. In the absence of complex dynamical behavior,

this static model allows a good guess of the dissociation probability for a fixed E_i, merely by looking at the fraction of molecular configurations leading to dissociation. From Fig. 5.9, there is good agreement between the HM and QCT results for molecules in the vibrational ground state, for $E_i < 5$ eV, whereas for molecules with v_i=1 the agreement is only good for $E_i < 4$ eV. These results can be taken as an indication of the inefficiency of the rotational and parallel translational motion to drive the molecule to the minimum energy reaction path. When E_i increases, the rotations become more efficient at steering the molecule towards the reaction path, because the high force zones of the PES start to play a predominant role [70]. This explains the difference between the HM probability and the 6D QCT results at high energies. In summary, the reaction probability is small at energies significantly above the minimum barrier height not only because of the presence of a narrow minimum reaction barrier, but also because of the nature of the dynamics, which does not allow the molecule to get orientated or positioned in such a away as to be able to pass the barrier. In fact, most of the molecules do not even approach the barrier, they are scattered back to the vacuum far from the minimum reaction barrier, as we can see in Fig. 5.10, where we have plotted the probability of a molecule to reach an interatomic distance r_0 (see Sec. 5.3.1).

5.3.3 Scattering

As we have shown in Sec. 5.3.2 reaction is the minority process for N_2 interacting with Ru(0001). Now we are going to focus on the majority process, scattering. Some extra information about the system can be extracted by looking at the molecules scattered back to the vacuum after the interaction with the surface. Experimentally it is not possible to study scattering under normal incidence conditions, therefore, most of the results we present in this section are for non-normal incidence. We defined the incidence angle Θ_i as the angle between the incident velocity vector and the surface normal (see Fig. 5.1(c)).

In Fig. 5.11(a) we present the angular distribution of the scattered molecules, for an incidence angle Θ_i=40°. We can see that the maximum of the distribution increases and its width (FWHM) decreases with incidence energy until $E_i = 0.41$ eV, and then the maximum decreases and the FWHM increases with E_i. A similar behavior has been found experimentally [12]. In Fig. 5.11(b) we have plotted the FWHM as a function of the incidence energy for Θ_i=40° and 50°. We see that for 50° the increase of the FWHM with E_i is less pronounced and starts at a higher E_i. It has been argued [12] that this behavior is related to the existence of two scattering regimes: thermal scattering should dominate at low incident energies, whereas structural scattering should dominate at high energies. The argument is that, in structural scattering, at higher normal energies ($E_\perp$) the molecule sees a more corrugated surface (higher penetration [71]), leading to a bigger momentum exchange and a broader distribution, consistent with the experimental and theoretical results. For the same incidence angle, $E_\perp$ increases with E_i, leading to an increase of FWHM with E_i, and for the same incidence energy, $E_\perp$ decreases with increasing Θ_i, leading to a smaller FWHM at Θ_i=50°. For low incidence energies, the argument of thermal scattering can not be applied to our theoretical results (which nevertheless show a decrease of the FWHM with E_i like the experimental

results), because we consider the surface atoms fixed in their equilibrium position (see Sec. 5.2). The behavior of the FWHM at low E_i can however also be understood without invoking the effect of the phonons. For low E_i the molecules are reflected far from the surface, and for the energy range 0.05-0.41 eV the corrugation seen by the molecules is more or less the same, which implies that the momentum exchange is similar for the smaller energies (see inset Fig. 5.12). This implies that the relative momentum exchange, defined as $|\Delta K|/K_i$, should decrease with increasing E_i. The relative momentum exchange is directly related to the width of the angular distribution: the bigger the relative momentum exchange, the broader the angular distribution is expected to be and vice versa. From Fig. 5.12 we observe that the relative momentum change indeed decreases with E_i until $E_i \approx 0.41$ eV and from this point on increases with E_i . Comparing Fig. 5.12 and 5.11(b) we see that the minimum of the FWHM of the angular distribution agrees with the minimum of the relative momentum exchange curve.
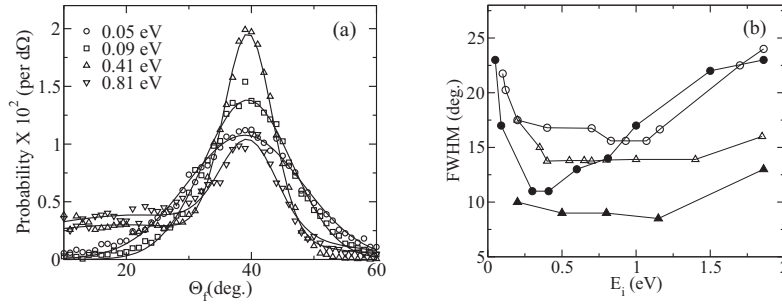
Figure 5.11: The reflection probabilities per unit solid angle as a function of Θ_f , for Θ_i=40° and several E_i. The continuous lines through the data points are to guide the eye only. (b) The width of the angular distribution as a function of E_i. Open symbols experimental data [12]; filled symbols our theoretical results. Circles: Θ_i=40°; triangles: Θ_i=50°.

Other interesting features that we can extract from the scattered molecules, which contain information about the interaction between the molecule and the surface, are energy transfer to the molecule's internal motion and to the parallel translational motion. The average energy transfered to translation parallel to the surface ($\langle\Delta E_x\rangle$) as a function of E_i is shown in Fig. 5.13(a), along with the available experimental results [13] . Both theory and experiment show a small excitation of the translational energy parallel to the surface, which increases which increasing E_i (and $E_\perp$, for high E_i). As explained above, when $E_\perp$ increases the molecules get closer to the surface and experiences more corrugation, which favors the excitation of the parallel motion via momentum exchange. In the theory, for the higher energies we observe a clear difference between the results for the initial conditions Θ_i=19° and Θ_i=40°: $\langle\Delta E_x\rangle$ is twice as high as for the first condition. Two factors can explain this differences: (i) Penetration (and therefore

corrugation) is expected to be increased when Θ_i decreases [71]. (ii) For $\Theta_i=19°$ there is a much bigger difference between the normal and the parallel energy, which favors the transfer of energy from normal to parallel motion. From the experimental data it is not possible to establish any kind of dependence of ΔE_x on Θ_i, due to the magnitude of the errors and the small number of points for $\Theta_i=40°$.

Rotational excitation is overestimated in our theoretical calculations in comparison with the experimental findings [13], as can be observed in Fig. 5.13(b), where we have plotted the average of the energy transfered to rotation ($\langle\Delta E_{rot}\rangle$) as a function of the incidence energy, for $J_i=0$. The disagreement between theory and experiment increases with E_i, and the theoretical value $\langle\Delta E_{rot}\rangle$ becomes twice the experimental one at $E_i\approx 2.8$ eV. The disagreement between theory and experiment is even worse for vibrational excitation (see Fig. 5.13(c)). In this case, the theoretical average of the energy transfered to vibration $\langle\Delta E_{vib}\rangle$ is around 7 times bigger than the experimental one at $E_i =2.8$ eV (the only available experimental data [13]). Experimentally no measurable vibrational excitation was observed, the value given in Fig. 5.13(c) is merely an upper bound determined to $v=1$ excitation. It is not clear whether an attempt was made to measure vibrational excitation to $v >1$. The lack of vibrational excitation in this experiment was attributed in part to the spectral overlap associated with transitions of $v=0$, $J \geq 49$ and the low J transitions of $v=1$. Taking into account that experiments did not consider transitions to $v >1$ we have recalculated the $\langle\Delta E_{vib}\rangle$ as it would be measured in experiments only considering scattering to $v=0$ and 1, i.e., we suppose that $P_{ref}(v_f=0) + P_{ref}(v_f=1)=1$, where $P_{ref}(v_f)$ is the probability that a reflected molecule is scattered to the final state v_f. Fig. 5.13(c) shows that when making this supposition our theoretical $\langle\Delta E_{vib}\rangle$ is lowered to a value that is only twice the experimental value (a difference similar to that found for rotational excitation).

Classical dynamics is not the best method to study energy transfer to molecule's internal motions, because the selection rules limiting this transfer are not taken into account. Quantum mechanically only transitions between internal energy states with $\Delta v=n$, n being 0,1,2..., and $\Delta J=2n$ (because of the nuclear spin symmetry) are allowed for N_2, whereas classically the internal energy transfer presents a continuous distribution. Nevertheless, it has been shown previously that classical dynamics can account for some typical quantum features like rotational excitation [72] or even diffraction [73]. The main problem classical dynamics face in these kind of studies is how to use 'binning', i.e, how to transform a continuous distribution into a discrete representation. In the case of rotational excitation we have checked our results using two different binning methods: (i) 'Homogeneous binning', in which we assign J to reflected molecules by evaluating the closest integer that satisfies $J_{cl} = [-1 + (1 + 4L^2/\hbar^2)^{1/2}]/2$ and $\Delta J = 2n$, where L is the classical angular momentum, and we consider all trajectories to have the same weight in the final discrete distribution. (ii) 'Non-homogeneous binning' [74], where each trajectory is weighted by a Gaussian-like coefficient such that the closer the J_{cl} values to integer values satisfying $\Delta J = 2n$, the larger the coefficient. Both method (i) and (ii) allow one to choose $\Delta J = $ n or 2n (n=0,1,2...). No significant differences in the results have been found using these two methods with the rule $\Delta J = 2n$, which seems reasonable due to the small energy spacings between the rotational

levels of N_2. This suggests that the disagreement between theory and experiment for the rotational energy transfer cannot be attributed to deficiencies of the QCT method.
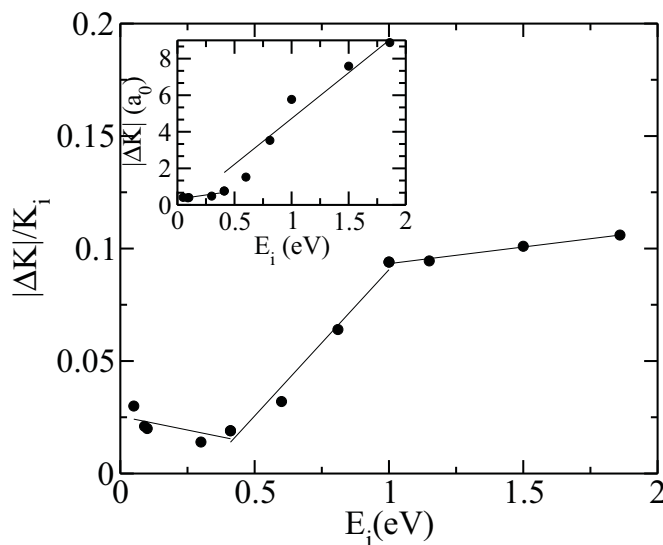

Figure 5.12: The relative momentum exchange as a function of the incidence energy for Θ_i=40 °. The continuous lines through the data points are to guide the eye only.

The agreement between the scattering experiments and our 6D adiabatic calculations can also be affected by the use of the frozen surface approximation. Although the phonons seem to play a minor role for dissociative chemisorption, they could be important for rotational excitation, because the energy spacings between the rotational levels are small. As we do not include the phonons in our calculation we can only speculate about their effect using the previous experimental and theoretical results. Low dimensional calculations suggest that the inclusion of phonons in the dynamics increases the reaction threshold. This means that the molecule looses energy to the surface, thus less energy is available for rotational excitation and therefore the inclusion of phonons could lead to less rotational and vibrational excitation. Of course, once the phonons are taken into account the rotational excitation is expected to increase with T_s, the larger T_s the smaller the transfer of energy from the molecule to the surface is expected, and then more energy is available for rotational excitation. The increase of rotational excitation with T_s has been observed experimentally [13].
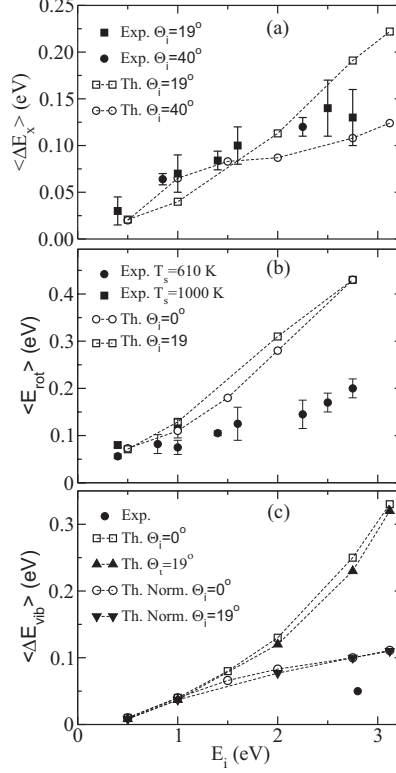
Figure 5.13: (a) The conversion of incidence energy E_i into translational energy parallel to the surface, ΔE_x, as a function of the incidence energy. The filled symbols are from experiment [13]. (b) The average of the energy transferred to rotation $\langle \Delta E_{rot} \rangle$ as a function of the translational energy. (c) The average of the energy transfered to vibration $\langle \Delta E_{vib} \rangle$ as a function of the translational energy. 'Norm' means that we suppose $P_{ref}(v_f = 0) + P_{ref}(v_f = 1) = 1$.

It has been suggested [13] that the absence of observable vibrational excitation in the experiment could be due to non-adiabatic coupling to e-h pair excitations. This conclusion is partly based on the previous observation of significant vibrational excitation and de-excitation for another 'exit' channel system, $H_2(D_2)/Cu(111)$ [20], for which e-h pair excitations is expected to be unimportant, and also on the comparison between adiabatic and non-adiabatic low dimensional calculations (see above). But, as we have shown in section III, $N_2/Ru(0001)$ presents large differences with the other prototype 'exit' channel system, $H_2+Cu(111)$, and low dimensional calculations can not be used to describe the dynamics of this system properly. On the other hand, our adiabatic 6D calculations do show more vibrational excitation than the experiments, and we cannot rule out that this is due to the absence of e-h pair excitations in our model. To obtain more insight in the role of phonons and e-h pair excitations, 6+2D calculations should be done in a fashion similar to that used in the 2+2D model of Diekhoner *et al.* [11], using an appropriate coupling strength parameter describing the non-adiabatic coupling [26].

5.4 Summary and conclusions

In this paper we have presented a six-dimensional (6D) quasi-classical dynamics study, within the adiabatic approximation, of N_2 reacting with and scattering from a Ru(0001) surface. The 6D potential energy surface (PES) has been constructed applying a modified Shepard method to a non-uniform set of electronic structure data, which are chosen using quasi-classical dynamics. The electronic structure data were obtained with density functional theory, using the RPBE generalized gradient approximation in a supercell approach.

The dissociative adsorption probabilities computed using 6D quasi-classical dynamics show good agreement with previous experimental results, with a very low reaction probability for incidence energies significantly above the minimum reaction barrier. A comparison with previous calculations using a 2+1D adiabatic model including phonons shows that the inclusion, in both a static description using the hole model (HM) and in the dynamics, of the 4 DOFs of the molecule associated with the rotation and translation parallel to the surface lowers the reaction probability by two orders of magnitude. Furthermore, the good agreement between the experimental and the HM probability shows that the low reactivity of the system can already be understood by looking only at the static properties of the PES. Our results show clearly that the previous experimental findings can be explained largely within an adiabatic framework, without invoking large non-adiabatic effects, if the 6 DOFs of the molecule are included in an accurate description of the PES. The low reactivity of the system reflects the high anisotropy and corrugation of the potential, making the barrier a very narrow bottleneck to reaction.

Theoretical angular scattering distributions show the same behavior as observed experimentally. In agreement with experiment, two scattering regimes can be distinguished: one operating at low energy and one at high energies. At high energies the decrease of the maximum of the distribution and the increase of its width with energy are due to the increase of the corrugation seen by the molecules (structure scattering). For low energies, the calculations suggest that the decrease of the width of the distribution with energy is not (entirely) due to the interaction with the surface phonons, because it is also observed in our static surface calculations. Instead, it reflects a decrease of the relative momentum exchange as the incidence energy is increased in a regime where structural scattering does not yet occur.

Finally, whereas our theoretical results show a small excitation of the translation parallel to the surface increasing with E_i, in good agreement with the experiment, rotational and vibrational excitation are overestimated by our theoretical calculations. Additional work is needed in which motion in all six N_2 DOFs is considered alongside dissipation to phonons and electron-hole (e-h) pair excitations to explain these discrepancies.

Although our study by itself can not be used to determine in an accurate way the influence of the electron-hole (e-h) pair excitations on the interaction between N_2 and Ru(0001), it allows us at least, to determine (assuming the experiments to be accurate, and considering the factors that affect the accuracy in the theory) an upper bound to the influence that non-adiabatic effects have on the reactivity

of this system. This influence is much smaller than previously suggested by low dimensional calculations: Our calculations suggest that at the highest incidence energies considered, e-h pair excitations diminish the reactivity by no more than a factor 3, rather than by two orders of magnitudes as suggested by the previous low-dimensional calculations. On the other hand, it is essential to take into account the multidimensional effects (rotation and translation parallel to the surface) in the dynamics for to an appropriate description of the system. This reduces the reactivity by 2 orders of magnitude. The minor role played by non-adiabatic effects in dissociative chemisorption of N_2 on Ru(0001) can be understood from recent theoretical work, which strongly suggests that a breakdown of the Born-Oppenheimer approximation should be expected for: (i) Molecules with high electron spin interacting with a metal surface with a low density of states at the Fermi level, due to spin quenching before the systems interact [35]. (ii) Molecules with intermediate electronegativities, for which the time scale for the electron transfer process and the nuclear motion are comparable [36]. N_2 has zero electronic spin, so that non-adiabatic spin quenching is not possible, and it also has a low electronegativity so that no non-adiabatic effects accompanying electron transfer from the surface to the molecule are expected.

Acknowledgments

Bibliography

[1] T. Matsushima, Surf. Sci. **197**, L287 (1988).

[2] H. Shi, K. Jacobi, and G. Ertl, J. Chem. Phys. **99**, 9248 (1993).

[3] H. Dietrich, P. Geng, K. Javobi, and G. Ertl, J. Chem. Phys. **104**, 375 (1996).

[4] L. Romm, G. Katz, R. Kosloff, and M. Asscher, J. Phys. Chem. B **101**, 2213 (1997).

[5] M. J. Murphy, J. F. Skelly, A. Hodgson, and B. Hammer, J. Chem. Phys. **110**, 6954 (1999).

[6] L. Romm, O. Citri, R. Kosloff, and M. Asscher, J. Chem. Phys. **112**, 8221 (2000).

[7] L. Diekhoner, H. Mortensen, A. Baurichter, A. C. Luntz, and B. Hammer, Phys. Rev. Lett. **84**, 4906 (2000).

[8] L. Diekhöner, H. Mortensen, A. Baurichter, and A. C. Luntz, J. Chem. Phys. **115**, 3356 (2001).

[9] L. Diekhöner, H. Mortensen, A. Baurichter, E. Jensen, V. V. Petrunin, and A. C. Luntz, J. Chem. Phys. **115**, 9028 (2001).

[10] R. C. Egeberg, J. H. Larsen, and I. Chorkendorff, Phys. Chem. Chem. Phys. **3**, 2007 (2001).

[11] L. Diekhoner, L. Hornekaer, H. Mortensen, E. Jensen, A. Baurichter, V. V. Petrunin, and A. C. Luntz, J. Chem. Phys. **117**, 5018 (2002).

[12] D. C. Papageorgopoulos, B. Berenbak, M. Verwoest, B. Riedmuller, S. Stolte, and A. W. Kleyn, Chem. Phys. Lett. **305**, 401 (1999).

[13] H. Mortensen, E. Jensen, L. Diekhoner, A. Baurichter, A. C. Luntz, and V. V. Petrunin, J. Chem. Phys. **118**, 11200 (2003).

[14] J. J. Mortensen, Y. Morikawa, B. Hammer, and J. K. Nørskov, J. Catal. **169**, 85 (1997).

[15] S. Dahl, A. Logadottir, R. C. Egeberg, J. H. Larsen, I. Chorkendorff, E. Tornqvist, and J. K. Nørskov, Phys. Rev. Lett **83**, 1814 (1999).

[16] S. Dahl, E. Tornqvist, and I. Chorkendorff, J. Catal. **192**, 381 (2000).

[17] R. v. Harrevelt, K. Honkala, J. K. Nørskov, and U. Manthe, J. Chem. Phys. **122**, 234702 (2005).

[18] G. J. Kroes, A. Gross, E. J. Baerends, M. Scheffler, and D. A. McCormack, Acc. Chem. Res. **35**, 193 (2002).

[19] M. F. Somers, D. A. McCormack, G. J. K. R. A. Olsen, E. J. Baerends, and R. C. Mowrey, J. Chem. Phys. **117**, 6673 (2002).

[20] C. T. Rettner, D. J. Auerbach, and H. A. Michelsen, Phys. Rev. Lett. **68**, 2547 (1992).

[21] C. T. Rettner, H. A. Michelsen, and D. J. Auerbach, J. Chem. Phys. **102**, 4625 (1995).

[22] G. J. Kroes, G. Wiesenekker, E. J. Baerends, and R. G. Mowrey, Phys. Rev. B **53**, 10397 (1996).

[23] M. Hand and J. Harris, J. Chem. Phys. **92**, 7610 (1990).

[24] M. Head-Gordon and J. C. Tully, J. Chem. Phys. **103**, 10137 (1995).

[25] B. N. J. Persson, Chem. Phys. Lett. **139**, 457 (1987).

[26] A. C. Luntz and M. Persson, J. Chem. Phys. **123**, 074704 (2005).

[27] B. Gergen, H. Nienhaus, W. H. Weinberg, and E. W. McFarland, Science **294**, 2521 (2001).

[28] J. D. White, J. Chen, D. Matsiev, D. J. Auerbach, and A. M. Wodtke, Nature **433**, 503 (2005).

[29] M. Born and E. Oppenheimer, Ann. Phys. **84**, 457 (1927).

[30] A. M. Wodtke, J. Tully, and D. J. Auerbach, Int. Rev. Phys. Chem. **23**, 513 (2004).

[31] G. R. Darling and S. Holloway, Rep. Prog. Phys. **58**, 1595 (1995).

[32] P. Nieto, E. Pijper, D. Barredo, G. Laurent, R. A. Olsen, E.-J. Baerends, G.-J. Kroes, and D. Farias, Science **312**, 86 (2006).

[33] K. Reuter, D. Frenkel, and M. Scheffler, Phys. Rev. Lett. **93**, 116105 (2004).

[34] K. Honkala, A. Hellman, I. N. Remediakis, A. Lagadottir, Carlsson, S. Dahl, C. H. Christensen, and J. K. Nørskov, Science. **307**, 555 (2005).

[35] J. Behler, B. Delley, S. Lorenz, K. Reuter, and M. Scheffler, Phys. Rev. Lett. **94**, 036104 (2005).

[36] A. Hellman, B. Razaznejad, and B. I. Lundqvist, Phys, Rev, B **71**, 205424 (2005).

[37] G. J. Kroes, E. J. Baerends, and R. G. Mowrey, Phys. Rev. Lett. **78**, 3583 (1997).

[38] C. Diaz, J. K. Vincent, G. P. Krishnamohan, R. A. Olsen, G. J. Kroes, K. Honkala, and J. K. Nørskov, Phys. Rev. Lett. **96**, 096102 (2006).

[39] J. Ischtwan and M. A. Collins, J. Chem. Phys. **100**, 8080 (1994).

[40] R. P. A. Bettens and M. A. Collins, J. Chem. Phys. **111**, 816 (1999).

[41] C. Crespos, M. A. Collins, E. Pijper, and G. J. Kroes, J. Chem. Phys. **120**, 2392 (2004).

[42] DACAPO, http://dcwww.camp.dtu.dk/campos/Dacapo/.

[43] B. Hammer, L. B. Hansen, and J. K. Nørskov, Phys. Rev. B **59**, 7413 (1999).

[44] D. Vanderbilt, Phys. Rev. B **41**, 7892 (1990).

[45] D. J. Chadi and M. L. Cohen, Phys. Rev. B **8**, 8747 (1973).

[46] R. G. Parr and R. J. White, J. Chem. Phys. **49**, 1059 (1968).

[47] K. C. Thompson, M. J. T. Jordan, and M. A. Collins, J. Chem. Phys. **108**, 8302 (1998).

[48] M. A. Collins, Theor. Chem. Acc. **108**, 313 (2002).

[49] H. F. Busnengo, A. Salin, and W. Dong, J. Chem. Phys. **112**, 7641 (2000).

[50] R. A. Olsen, H. F. Busnengo, A. Salin, M. F. Somers, G. J. Kroes, and E. J. Baerends, J. Chem. Phys. **116**, 3841 (2002).

[51] M. Karplus, R. N. Porter, and R. D. Sharma, J. Chem. Phys. **43**, 3259 (1965).

[52] Y. Guo, D. L. Thompson, and T. D. Sewell, J. Chem. Phys. **104**, 576 (1996).

[53] D. A. McCormack and G. J. Kroes, Phys. Chem. Chem. Phys. **1**, 1359 (1999).

[54] D. A. McCormack, G. J. Kroes, R. A. Olsen, I. A. Groeneveld, J. N. P. van Stralen, E. J. Baerends, and R. C. Mowrey, Faraday Discuss. **117**, 109 (2000).

[55] E. Pijper, M. F. Somers, G. J. Kroes, R. A. Olsen, E. J. Baerends, H. F. Busnengo, A. Salin, and D. Lemoine, Chem. Phys. Lett. **347**, 277 (2001).

[56] P. Riviere, H. F. Busnengo, and F. Martin, J. Chem. Phys. **123**, 074705 (2005).

[57] H. F. Busnengo, C. Crespos, W. Dong, J. C. Rayez, and A. Salin, J. Chem. Phys. **116**, 9005 (2002).

[58] W. C. Swope, H. C. Andersen, P. H. Berens, and K. R. Wilson, J. Chem. Phys. **76**, 637 (1982).

[59] A. C. Luntz, private communication.

[60] M. Asscher, private communication.

[61] J. K. Vincent, R. A. Olsen, and G. J. Kroes, J. Chem. Phys. **122**, 122 (2005).

[62] J. P. Perdew, J. A. Chevary, S. H. Vosko, K. A. Jackson, M. R. Pederson, D. J. Singh, and C. Fiolhais, Phys. Rev. B **46**, 6671 (1992).

[63] S. Andersson and M. Gruning, J. Phys. Chem. A **108**, 7621 (2004).

[64] G. J. Kroes, Prog. Surf. Sci. **60**, 1 (1999).

[65] C. T. Rettner and H. Stein, J. Chem. Phys. **87**, 770 (1987).

[66] G. Haase, M. Asscher, and R. J. Kosloff, J. Chem. Phys. **90**, 3346 (1989).

[67] R. R. Smith, D. R. Killelea, D. F. DelSesto, and A. L. Utz **304**, 992 (2004).

[68] A. C. Luntz, J. Chem. Phys. **113**, 6901 (2000).

[69] M. Karikorpi, S. Holloway, N. Henriksen, and J. K. Nørskov, Surf. Sci. **179**, L41 (1987).

[70] P. Riviere, A. Salin, and F. Martin, J. Chem. Phys. **124**, 084706 (2006).

[71] C. Diaz, H. F. Busnengo, F. Martin, and A. Salin, J. Chem. Phys. **118**, 2886 (2003).

[72] H. F. Busnengo, W. Dong, P. Sautet, and A. Salin, Phys. Rev. Lett. **87**, 127601 (2001).

[73] D. Farias, C. Diaz, P. Riviere, H. F. Busnengo, P. Nieto, M. F. Somers, G. J. Kroes, A. Salin, and F. Martin, Phys. Rev. Lett. **93**, 246104 (2004).

[74] L. Bonnet and J. C. Rayez, Chem. Phys. Lett. **277**, 183 (1997).

Samenvatting

Dissociatieve chemisorptie van methaan op Ni(111)

De rol van katalyse in de scheikunde en de industrie is een veel-bestudeerd onderwerp, en nog altijd een belangrijk onderzoeksgebied. Het veld van katalyse bestaat uit verschillende deelgebieden, waarbij heterogene katalyse een belangrijke plaats inneemt, vanwege zijn wijdverbreide toepassing in de chemische industrie. De basis van heterogene katalyse is de verandering van de eigenschappen van moleculen in de aanwezigheid van een (metaal) oppervlak. Zoals in vele andere gebieden in de scheikunde, is een gedetailleerde theoretische modellering noodzakelijk om katalytische activiteit op verschillende oppervlakken te begrijpen. Hedentendage is het mogelijk om met behulp van theoretische modellering vele gas-oppervlakte reacties en oppervlakte processen nauwkeurig te beschrijven. In dit proefschrift worden verschillende aspecten van twee belangrijke chemisorptiereacties theoretisch bestudeerd, namelijk de dissociatieve adsorptie van methaan op Ni(111), en stikstof dissociatie op Ru(0001). In **Hoofdstuk 1** worden enkele algemene aspecten van gas-metaaloppervlak reacties besproken.

In al het werk besproken in dit proefschrift wordt gebruik gemaakt van quantummechanische berekeningen, gebaseerd op dichtheidsfunctionaaltheorie (DFT). Met behulp van deze theorie wordt de interactiepotentiaal tussen het gasfase molecuul en het oppervlak beschreven. In dit onderzoek maak ik gebruik van vlakke golf DFT in de "generalized gradient approximation'' (GGA) om interactie energieën te berekenen. Voor de dynamica berekeningen wordt de quasi-klassieke trajectmethode gebruikt. Voor de quantummechanische dynamica berekeningen gebruik ik de multi-configuratie tijds-afhankelijke Hartree methode (MCTDH). Het potentiële energie-oppervlak (PES) is gefit met behulp van een Shepard interpolatiemethode. In alle berekeningen zijn twee belangrijke benaderingen gebruikt: de Born-Oppenheimer benadering, en het negeren van energie-overdracht naar de fononen in het oppervlak. In Hoofdstuk 1 worden deze benaderingen besproken. **Hoofdstuk 2** geeft een overzicht van de theoretische methoden die gebruikt zijn in dit onderzoek.

In **Hoofdstuk 3 en 4** bespreek ik de dissociatieve chemisorptie van methaan op een Ni(111) oppervlak. De reactie van methaan op een nikkeloppervlak naar een geabsorbeerde methylgroep en waterstofatoom is de snelheidsbepalende stap bij stoomreforming, het belangrijkste proces bij industriële waterstofproductie. Deze reactie wordt ook beschouwd als een prototype voor de geactiveerde dissociatie van

een polyatomig molecuul op een vast oppervlak. Veel van de toestandsopgeloste experimenten aan dit systeem bestuderen de rol van de vibrationele energie in de bevordering van de reactie, deze worden besproken in Hoofdstuk 1. Al deze experimenten wijzen uit dat de uitgangspunten van de statistische theorieën die zijn gebaseerd op de "Microcanonical unimolecular rate theory" fout zijn en dat een dynamische beschrijving van het systeem nodig is.

Hoofdstuk 3 behandelt de "vibrational mode following" berekeningen aan de reactie. De geometrie waarop de berekening is gebaseerd is verkregen middels reactiepad (RP) berekeningen. In de RP berekeningen werd een endotherme, late barrière energieprofiel gevonden. De vibrationele frequenties langs de RP geometrieën wezen op een significante betrokkenheid van de verschillende vibrationele coördinaten in het bereiken van de overgangstoestand. Ik gebruikte Massey snelheden en de vibrationele karakters van de normaalvibraties om de koppeling tussen de vibrationele niveaus te analyseren en de aard van de verschillende kruisingsregio's te bestuderen. Ik vond twee verschillende kruisingsregio's in het RP, één in het ingangskanaal en een tweede in de buurt van de overgangstoestand. Om de ruis in de DFT krachten en Hessian matrixes te verwijderen zijn 'Levenberg-Marquardt non-linear least square fitting' methoden gebruikt. Een vooralsnog vermeden kruising in de buurt van het ingangskanaal is in detail geanalyseerd. Hieruit bleek dat pre-excitatie van ν_1 met één quantum drie keer zo effectief zou moeten zijn voor het bevorderen van de reactie dan pre-excitatie van ν_3. Een andere belangrijke observatie bij deze kruising was de quarantining van de vibrationele energie in de CH_3-groep in het geval van excitatie van de asymmetrische ν_3 strek-vibratie. De analyse van de late kruising impliceert dat de buigvibraties niet sterk zijn gekoppeld met de reactiecoördinaat, in tegenstelling tot de strekvibraties die wel een efficiënte koppeling laten zien. Deze observatie is ook in lijn met de experimentele waarnemingen en in overeenstemming met theoretisch werk van Halonen et al.

In **Hoofdstuk 4** bespreek ik de 2D, 3D en 4D quantumdynamica bestudering van het $CH_4/Ni(111)$ systeem. De quantumdynamicaberekeningen worden met behulp van de MCTDH methode toegepast op een volledig-dimensionaal PES (met betrekking tot de CH_4 vrijheidsgraden). Om dit te bewerkstelligen wordt een gestandaardiseerde formule voor de 15D kinetische energie-operator afgeleid. Ik ident ificeer vier vrijheidsgraden die sterk gecorreleerd met het 15D minimum energie traject evolueren en sub-selecties hiervan worden in het dynamische model opgenomen, met behulp van zogenaamde "constraints". In onze gereduceerde-dimensie berekeningen vind ik dat de "cartwheel" roterende beweging van de CH_3-as de reactie versnelt, wat overeenkomt met de bevindingen van Xiang et al. Voor reactie met een lage botsings-energie vind ik dat de reactiviteit nagenoeg onafhankelijk is van het draai-impulsmoment. Voor reactie bij een licht hogere botsings-energie (1.1-1.4 eV) voorspelt ons 4D model correct de experimentele bevinding dat de $1\nu_3$ toestand meer reactief is dan de $3\nu_4$ toestand. Verdere analyse van de resultaten laat zien dat het model betere resultaten zal produceren als meer rotatie- en translatie-vrijheidsgraden toegevoegd worden.

Recentelijk heeft de studie van de dissociatie van N_2 op Ru(0001) veel aandacht ontvangen van zowel experimentele en theoretische scheikundigen. Het is aangetoond dat ruthenium een betere katalysator is dan de Haber-Bosch katalysator, alhoewel duurder, voor de synthese van NH_3 onder bepaalde omstandigheden. Deze

reactie wordt door theoretische scheikundigen beschouwd als een modelreactie om de geldigheid van een electronisch adiabatische aanpak en de rol van electrongat (e-h) paar excitaties te testen. De experimenten laten een lage dissociatie-waarschijnlijkheid (≤1%) zien bij een botsings-energie die tot twee maal zo hoog is als de reactie drempel. Laser-geassisteerde associatieve desorptie experimenten suggereren dat ruim 2/3 van de energie, die door het molecuul wordt gebruikt om de barrière te overwinnen, verloren is aan het oppervlak.

Ondanks de experimentele aanwijzingen voor niet-adiabatisch gedrag laat ons werk in **Hoofdstuk 5** een veel kleinere rol zien van niet-adiabatische effecten. In dit werk wordt een zes-dimensionale (inclusief de zes vrijheidsgraden van een molecule) adiabatische studie aan N_2 reagerend op Ru(0001) verricht. De PES-topologie verklaart de lage reactiviteit van N_2/Ru(0001) uit een hoge anisotropie en corrugatie van de potentiaal op de barrière. Dit benadrukt ook het belang van de initiële vibrationele excitatie ter bevordering van deze dissociatiereactie. De berekende reactiewaarschijnlijkheden komen goed overeen met moleculaire bundel experimenten. Deze mate van overeenstemming tussen adiabatische theorie en experiment suggereert een veel kleinere rol voor niet-adiabatische effecten dan eerder werd aangenomen op basis van de vergelijking van experimenten met laag-dimensionale niet-adiabatische modellen. Men kan zien dat het vakgebied van de gas-oppervlakte dynamiek zich heeft ontwikkeld en sterk gegroeid is in de afgelopen decennia. De "ab initio" rekenmethoden hebben nu een niveau bereikt dat belangrijke inzichten in het DFT-tijdperk mogelijk maakt. Hoewel een volledige dimensionale PES een grote hoeveelheid informatie geeft, blijft de ontwikkeling van een multidimensionele PES nog steeds een knelpunt in het onderzoek naar polyatomige molecule-oppervlak systemen. Naast de conventionele klassieke en quantumdynamica methoden zou een meer 'minimalistische' aanpak geprobeerd kunnen worden binnen het DFT kader (zoals adiabatische reactie pad Hamiltoni-aan methoden), om zo de onderliggende mechanismen van de chemie in dit soort gas-oppervlak systemen te verkennen.

List of publications

This thesis is based on the following publications:

- *Towards an understanding of the vibrational mode specificity for dissociative chemisorption of CH_4 on Ni(111): a 15 dimensional study*, G. P. Krishnamohan, R. A. Olsen, Á. Valdés, and G. J. Kroes, Phys. Chem. Chem. Phys., **12**, 7654 (2010). Chapter 3.

- *Quantum dynamics of dissociative chemisorption of CH_4 on Ni(111): Influence of the bending vibration*, G. P. Krishnamohan, R. A. Olsen, G. J. Kroes, F. Gatti, and S. Woittequand, J. Chem. Phys., in press. Chapter 4.

- *Reactive and nonreactive scattering of N_2 from Ru(0001): A six-dimensional adiabatic study*, C. Díaz, J. K. Vincent, G. P. Krishnamohan, R. A. Olsen, G. J. Kroes, K. Honkala, and J. K. Nørskov, J. Chem. Phys, **125**, 114706 (2006). Chapter 5.

- *Multidimensional effects on dissociation of N_2 on Ru(0001)*, C. Díaz, J. K. Vincent, G. P. Krishnamohan, R. A. Olsen, G. J. Kroes, K. Honkala, and J. K. Nørskov, Phys. Rev. Lett., **96**, 96102 (2006). Chapter 5.

Other publications:

- *Phase stabilities of Pd-H alloys: First-principles investigations with a statistical thermodynamics approach*, A. Marashdeh, D. E. Nanu, G. P. Krishnamohan and A. J. Böttger (article in preparation, 2010).

- *A computational study of cation-π interaction in polycyclic systems: exploring the dependence on the curvature and electronic factors*, U. Devapriyakumar, M. Punnagai, G. P. Krishnamohan, and G. N. Sastry, Tetrahedron, **60**, 3037 (2004).

Curriculum Vitae

I was born on 28 February of 1980 in Trivandrum, India. I passed the secondary school studies in 1995 and then chose the math group for the pre-university course with an optional subject: electronics. In 1997, I joined the University College in Trivandrum for the B.Sc. course in Chemistry. There, Dr. Sadasivan and Dr. C. Moly Merceline guided me in several theoretical/experimental sections in chemistry. My M.Sc. program was in physical chemistry which I did in the campus of Mahatma Gandhi University in Kerala, India. Dr. A. S. Padmanabhan and Dr. G. Narahari Sastry guided me in mathematical and computational chemistry respectively. After M.Sc. course I joined an engineering training center in Trivandrum to teach programming for some months.

On May 1'st of 2004, I started my Ph.D. research work in the theoretical chemistry group led by Prof. Dr. Geert-Jan Kroes in the University of Leiden. Prof. Dr. Roar A. Olsen is the other promoter. The main goal of the project is to study the role of vibrational efficacy of the different vibrational eigenstates of the methane molecule in its dissociative chemisorption on the nickel (111) surface.

In 2008 and 2009 I have assisted in the elementary quantum chemistry course for the B.Sc. students in life science and technology in the Technical University of Delft, where Dr. Martina Huber was the lecturer.

During my Ph.D. program, I have attended several winter schools and conferences. I attended the Dutch winter school in theoretical chemistry and spectroscopy in 2004, 2005 and 2006 in Belgium. In 2006, I participated in the winter school in 'computational nanoscience' held in Germany. I have been to the "Spectroscopie en Theorie" national conference in Lunteren for four times for poster presentations. In 2005, 2007 and in 2009, I have attended the GRC conferences entitled 'Dynamics at surfaces' in the USA for poster presentations.

Acknowledgement